ISSN 1607-8829

Journal of
THERMOELECTRICITY

International Journal

- General problems
- Theory
- Materials research
- Technology
- Design
- Metrology and standardization
- Reliability
- Thermoelectric products
- News
- Discussion

2013

2

Institute of Thermoelectricity, Academy of Sciences and Ministry of Education and Science of Ukraine

Journal of THERMOELECTRICITY

International Research
Founded in December, 1993
published 6 times a year

No. 2 *2013*

Founders - National Academy of Sciences, Ukraine
Institute of Thermoelectricity of National Academy of Sciences and Ministry of Education and Science of Ukraine

Certificate of state registration № КВ 15496-4068 ПР

Editorial office manager D. Taschuk

Editors:
L. Vikhor, L. Kosyachenko, A. Farion, V. Kramar, V. Katerynchuk

Published by decision of Scientific Board of Institute of Thermoelectricity
of National Academy of Sciences and Ministry of Education and Science of Ukraine

Address of editorial office:
Ukraine, 58002, Chernivtsi, General Post Office, P.O. Box 86.
Phone: +(380-3722) 7 58 60.
Fax: +(380-3722) 4 19 17.
E-mail: jt@inst.cv.ua
http:// www.jt.cv.ua

Signed for publication 25.04.13. Format 70×108/16. Offset paper №1. Offset printing.
Printer's sheet 11.1. Publisher's signature 9.2. Circulation 400 copies. Order 6.

Printed by “Bukrek” publishers,
10, Radischev Street, 58000, Chernivtsi, Ukraine.

CONTENTS

Theory

L.P. Bulat, I.A. Nefedova Nonlocal transport phenomena in semiconductors 5

P.V. Gorsky, V.P. Mikhalchenko On the electric conductivity of contacting particles of thermoelectric material 12

P.I. Baranskii, G.P. Haidar Anisotropic scattering theory and relevant problems of the kinetics of electron processes in many-valley semiconductors 19

L.P. Bulat, D. Kossakovski, D.A. Pshenai-Severin The influence of phonon thermal conductivity on thermoelectric figure of merit of bulk nanostructured materials with tunneling contacts 30

Material Research

D.M. Freik, C.A. Kryskov, I.V. Horichok, T.S. Lyuba, O.S. Krynytsky, O.M. Rachkovsky Synthesis, properties and mechanisms of doping with *Sb* of thermoelectric lead telluride *PbTe*:*Sb* 42

V.A. Romaka, Yu.V. Stadnyk, P. Rogl, V.V. Romaka, V.Ya. Krayovsky, O.I. Lakh, A.M. Horyn Parameter optimization of thermoelectric material based on *n-ZrNiSn* intermetallic semiconductor 51

E.I. Rogacheva, O.S. Vodorez Peculiarities of the concentration dependences of structural and thermoelectric properties in solid solutions *PbTe-PbSe* 61

Design

L.M. Vikhor, V.Ya. Mykhailovsky, V.R. Bilinsky-Slotylo Segmented and multi-stage structures based on $PbTe/Zn_4Sb_3$ for thermoelectric generator modules 74

L.I. Anatychuk, R.G. Giba, R.R. Kobylyanskii Some peculiarities of using medical heat meters in the investigation of local human heat release 82

Yu.M. Lobunets Solar pond with thermoelectric energy converter 89

Thermoelectric products

V.S. Gischuk Modernized device for human heat flux measurement 92

News

D.M. Freik (Dedicated to the 70-th anniversary) 99

L.P. Bulat

L.P. Bulat, I.A. Nefedova

Saint-Petersburg National Research University ITMO
9, Lomonosov Str., Saint-Petersburg,
191002, Russian Federation

I.A. Nefedova

NONLOCAL TRANSPORT PHENOMENA IN SEMICONDUCTORS

The content of "nonlocality" concept in theory of transport phenomena is discussed. Nonlinear and nonlocal phenomena in thermoelectricity are compared. Finite element method is used to calculate the characteristic length of change in temperature and nonlocality length for a semiconductor "cone-plate" contact. It is shown that the presence of nonlinear phenomena brings about the emergence of nonlocal phenomena and vice versa.

Key words: nonlocal transport phenomena, nonlinear transport phenomena, thermoelectric phenomena, semiconductors, solids, finite element method.

Conventional theory of transport phenomena in solids, liquids and gases employs a well-known Boltzmann equation derived as far back as 1872. In almost all cases, local solutions of this equation are considered. In the strict sense, classical Boltzmann equation has its domain of applicability, and the problem of correctness of local solutions in each case demands verification and justification [1-3]. In monograph [1] and a cycle of works (see, for instance, [2, 3]) the fundamental concepts of a generalized Boltzmann gas-kinetic theory as part of nonlocal physics are developed. It is established that theory of transport phenomena can be considered within a unified theory based on nonlocal description [2]. Moreover, a generalized nonlocal quantum kinetics and gas-hydrodynamics is applicable to mathematical simulation of the vast class of objects – from galaxies to atoms [2, 3]. A large number of applied problems can be considered with the aid of a generalized Boltzmann nonlocal theory of transport, starting from study of various turbulent flows, application of generalized quantum mechanics and quantum hydrodynamics for the analysis of nanostructures, to theory of dark energy and matter evolution after the Big Bang [1-3].

What is the essence of nonlocality of transport phenomena in semiconductors and solids in general?

Let some function $f(x)$ and derivative $\partial\varphi(x)/\partial x$ are related by the relation [4]

$$f(x) = \int_{-\infty}^{+\infty} K(x-x')\frac{\partial\phi(x')}{\partial x'}\mathrm{d}x'. \tag{1}$$

Relation (1) between $f(x)$ and $\partial\varphi(x)/\partial x$ is inherently linear, rather than local, since the value $f(x)$ at point x depends on the value of derivative $\partial\varphi(x)/\partial x$ at other points [4]. A nonlocal bond nucleus $K(x-x')$ must possess the property $K(x-x') \to 0$ at $x-x' \to \propto$.

It is easy to verify [4] that if the nucleus is of the form $K(x-x') = K_0\delta(x-x')$ where $\delta(x-x')$ is a δ-function, then formula (1) goes over into $f(x) = -K_0 \mathrm{d}\varphi/\mathrm{d}x$, i.e. the relation acquires a local character. In other words, if some function *f(x)* depends only on the first derivative (derivatives) of other function with respect to coordinates, then function *f(x)* is local.

As is known, under thermodynamic equilibrium conditions temperature T and electrochemical potential $\mu = \mu_0 - e\varphi$ at each sample point are constant (μ_0 and φ are chemical and electrical potentials, respectively, e is electron charge). If, however, these conditions are not satisfied, the following spatial derivatives of temperature and electrochemical potential must be different from zero [4]:

$$\begin{aligned}
&\frac{\partial T}{\partial x}, \frac{\partial T}{\partial y}, \frac{\partial T}{\partial z}, \frac{\partial^2 T}{\partial x^2}, \frac{\partial^2 T}{\partial y^2}, \frac{\partial^2 T}{\partial z^2}, \frac{\partial^2 T}{\partial x \partial y}, \frac{\partial^2 T}{\partial x \partial y}, \frac{\partial^2 T}{\partial y \partial z}, \frac{\partial^3 T}{\partial x^3}, \frac{\partial^3 T}{\partial y^3}, \frac{\partial^3 T}{\partial z^3},\\
&\frac{\partial^3 T}{\partial x^2 \partial y}, \frac{\partial^3 T}{\partial x^2 \partial z}, \frac{\partial^3 T}{\partial x \partial y^2}, \frac{\partial^3 T}{\partial x \partial z^2}, \frac{\partial^3 T}{\partial x \partial y \partial z}, \frac{\partial^3 T}{\partial y^2 \partial z}, \frac{\partial^3 T}{\partial y \partial z^2}, \ldots\\
&\frac{\partial \mu}{\partial x}, \frac{\partial \mu}{\partial y}, \frac{\partial \mu}{\partial z}, \frac{\partial^2 \mu}{\partial x^2}, \frac{\partial^2 \mu}{\partial y^2}, \frac{\partial^2 \mu}{\partial z^2}, \frac{\partial^2 \mu}{\partial x \partial y}, \frac{\partial^2 \mu}{\partial x \partial y}, \frac{\partial^2 \mu}{\partial y \partial z}, \frac{\partial^3 \mu}{\partial x^3}, \frac{\partial^3 \mu}{\partial y^3}, \frac{\partial^3 \mu}{\partial z^3},\\
&\frac{\partial^3 \mu}{\partial x^2 \partial y}, \frac{\partial^3 \mu}{\partial x^2 \partial z}, \frac{\partial^3 \mu}{\partial x \partial y^2}, \frac{\partial^3 \mu}{\partial x \partial z^2}, \frac{\partial^3 \mu}{\partial x \partial y \partial z}, \frac{\partial^3 \mu}{\partial y^2 \partial z}, \frac{\partial^3 \mu}{\partial y \partial z^2}, \ldots
\end{aligned} \tag{2}$$

Of course, higher-order derivatives with respect to coordinates can be nonzero, too.

The vectors of current density and heat flux

$$\vec{j} = \{j_x, j_y, j_z\}, \quad \vec{q} = \{q_x, q_y, q_z\}$$

must be functions of derivatives of temperature and chemical potential with respect to coordinates [4]:

$$j_k = f_k^j(\ldots), \qquad q_k = f_k^q(\ldots), \tag{3}$$

where three dots in brackets mean a collection of spatial derivatives (2).

In the lectures by A.G. Samoilovich [4] it was assumed that with small deviations from thermodynamic equilibrium the expressions for current and heat flux densities (3) will comprise only linear summands, and will not involve quadratic, cubic and higher degrees of spatial derivatives of temperature and electrochemical potential. Thus, in (3) only linear summands will be left with quadratic, cubic, etc. higher derivatives with respect to coordinates.

However, direct solution of the Boltzmann equation and calculation of current density and heat flux density for semiconductors dependent on not very small temperature gradients [5-8] has shown that nonlinear and nonlocal terms in equations for fluxes are of the same order. Therefore, at least in the model assumed in [5-8], the presence of nonlinear summands automatically brings about the emergence of nonlocal terms, and, vice versa, the presence of nonlocal summands automatically causes the emergence of nonlinear terms. In one-dimensional geometry, solution of the Boltzmann equation was obtained with electron scattering on acoustic phonons or ionized impurities by two methods: perturbation theory and variation [5-8]. Both methods yield the expressions for current density and heat flux density. If we restrict ourselves to conventional linear and local summands and the first nonlinear and nonlocal terms, then the equation for current density for a single-dimensional problem can be represented as follows:

$$\begin{aligned}
j = &-\sigma \frac{\mathrm{d}\mu}{\mathrm{d}x} - \sigma\alpha \frac{\mathrm{d}T}{\mathrm{d}x} + \\
&+ a_1 \left(\frac{\mathrm{d}T}{\mathrm{d}x}\right)^3 + a_2 \left(\frac{\mathrm{d}T}{\mathrm{d}x}\right)^2 \frac{\mathrm{d}\mu}{\mathrm{d}x} + a_3 \frac{\mathrm{d}T}{\mathrm{d}x}\left(\frac{\mathrm{d}\mu}{\mathrm{d}x}\right)^2 + a_4 \left(\frac{\mathrm{d}\mu}{\mathrm{d}x}\right)^3 + \\
&+ a_5 \frac{\mathrm{d}^2 T}{\mathrm{d}x^2}\frac{\mathrm{d}T}{\mathrm{d}x} + a_6 \frac{\mathrm{d}^2 T}{\mathrm{d}x^2}\frac{\mathrm{d}\mu}{\mathrm{d}x} + a_7 \frac{\mathrm{d}T}{\mathrm{d}x}\frac{\mathrm{d}^2 \mu}{\mathrm{d}x^2} + a_8 \frac{\mathrm{d}^2 \mu}{\mathrm{d}x^2}\frac{\mathrm{d}\mu}{\mathrm{d}x} + a_9 \frac{\mathrm{d}^3 T}{\mathrm{d}x^3} + a_{10} \frac{\mathrm{d}^3 \mu}{\mathrm{d}x^3},
\end{aligned} \tag{4}$$

where σ and α are known electric conductivity and Seebeck coefficients (in the anisotropic case – second-rank tensors), a_k are kinetic coefficients characterizing nonlinear and nonlocal phenomena. The analytical expressions for coefficients a_k for different cases are given in [6, 7].

The first line in Eq. (4) corresponds to a conventional generalized Ohm's law which in a vector form is given by

$$\vec{j}^{(o)} = \hat{\sigma}\vec{E} - \hat{\sigma}\hat{\alpha}\nabla T, \tag{5}$$

where $\vec{E} = \frac{1}{e}\nabla\mu$ is a generalized intensity of the electric field.

Note that Eq. (4) involves not quadratic, but only cubic combinations of derivatives of temperature and electrochemical potential, and also third, rather than second, derivatives of temperature and electrochemical potential with respect to coordinate. It is due to symmetry requirements, i.e. in a one-dimensional or isotropic case, replacement of temperature gradient direction or electric field intensity should not lead to a change in current density or heat flux value. At the same time, in the case of a sample having no inversion centre an equation of (4) type must also involve quadratic terms. This fact yields a variety of new nonlinear and nonlocal phenomena in the samples having no inversion centre. Even in cubic crystals a variety of new effects can appear [9-11].

Apart from linear and local, Eq. (4) also involves nonlinear and nonlocal terms, i.e. actually we have in (4) an expansion in small parameters. Physically, it means that each of the two lengths, namely characteristic length of temperature change L_T and nonlocality length in temperature L_{Tnloc}

$$L_T = T\left(\frac{\mathrm{d}T}{\mathrm{d}x}\right)^{-1}, \; L_{Tnloc} = T\left(\frac{\mathrm{d}^2T}{\mathrm{d}x^2}\right)^{-1}, \tag{6}$$

are large as compared to current carrier cooling length L_0 [6-8]

$$L_T \geq L_0, \; L_{Tnloc} \geq L_0. \tag{7}$$

Eq.(4) has been written for a one-dimensional geometry. In a real three-dimensional problem the respective equation must also include summands comprising all, among them cross derivatives with respect to different coordinates (2).

Thus, if characteristic lengths (6) are not very large as compared to charge carrier cooling length, then, as it follows from solving the Boltzmann equation in a one-dimensional model [5-8], Eq. (4) must comprise nonlocal terms. To check the conditions whereby in a real three-dimensional model the nonlinear (nonlocal) phenomena must become apparent, we made a calculation using finite element method of the temperature field for a semiconductor "cone-plate" contact [12] which is often realized in various applied problems.

In the present paper, computer simulation method is used to study possible emergence of nonlocal thermoelectric phenomena in a real three-dimensional geometry. As a geometrical model, "truncated cone-plate" structure is employed (Fig. 1). Such a structure is interesting for the following reasons: 1) it simulates properly real contacts in the bulk nanostructured and composite materials [13]; 2) it describes properly particle contacts for spark plasma sintering method (SPS-method) showing good promise for creation of efficient thermoelectric nanomaterials [14]; 3) such a structure is used in thermoelements "with cold contacts" offering high thermoelectric figure of merit [15].

Let the Joule heat be used for heating "truncated cone-plate" contact, with electric voltage applied between the cone base and the lower part of the plate for electric current generation (Fig. 1).

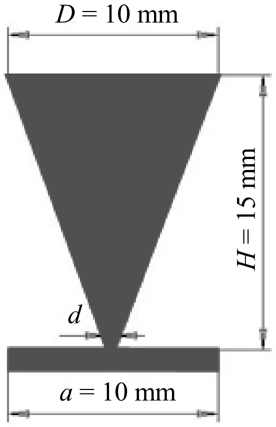

Fig. 1. Model geometry.

The basic equations of the problem include energy balance equation

$$\operatorname{div}\left(-\kappa\nabla T\right)=Q \tag{8}$$

and current-continuity equation

$$\operatorname{div}\left(\sigma\vec{E}\right)=0\,, \tag{9}$$

where Q is heat source power (Joule heat).

The boundary conditions were selected as follows: the lateral surfaces of cone and plate are thermally and electrically isolated, the temperatures of cone base and plate outer face are thermostated at equal temperature T_0, with constant electric voltage U_0 maintained between them, and cross-linking in temperature and thermal flux made in contact area. The boundary conditions of this kind correspond, for instance, to situation whereby the Benedicks effect arises [6-8].

Comsol Multiphysics software package was used to calculate and visualize the distribution of temperature field and temperature gradient. For certainty, *n-Ge* sample with parameters $k = 60.2$ W/(m·K), $\sigma = 10$ S/m was considered. Temperature $T_0 = 300$ K, voltage U_0 assumed the values: 50, 75, 100, 125 and 130 V. Geometric dimensions $D = 10$ mm, $H = 15$ mm, $a = 10$ mm were assigned (Fig. 1).

The calculated data are represented in Figs. 2 – 3.

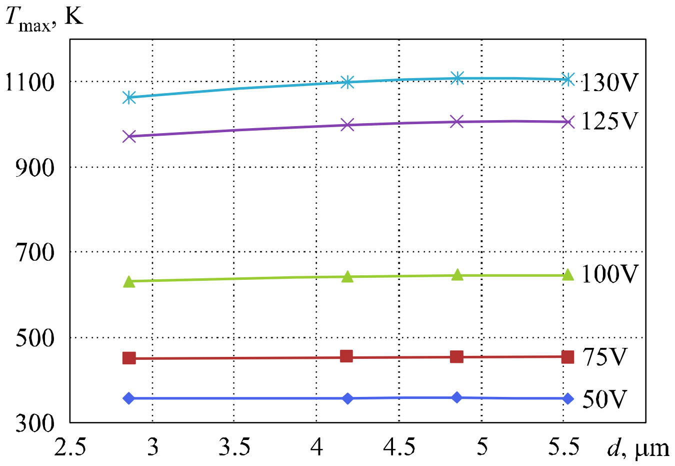

Fig. 2. Dependences of maximum temperature at contact point on contact plane diameter.

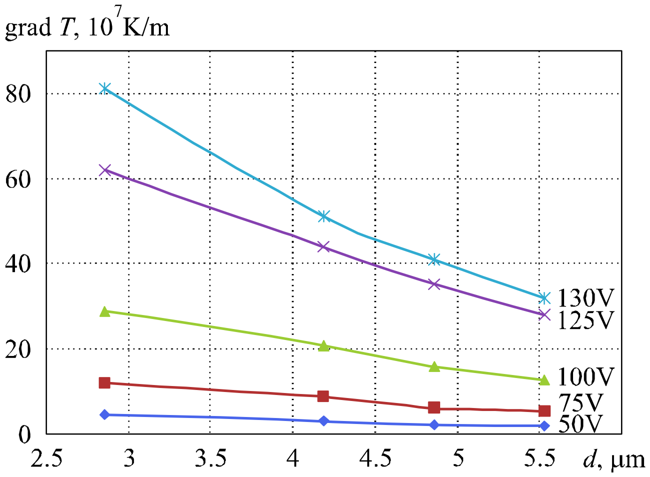

Fig. 3. Dependences of temperature gradient at contact point on contact plane diameter.

Calculations have shown that as long as geometric dimensions D, H and a are large as compared to neck diameter d (Fig. 1), these dimensions have no effect on the temperature field in contact area.

From Fig. 2 it is seen that maximum temperature in contact area is almost independent of neck diameter at a fixed voltage. It increases with voltage, and in this model at a voltage of 130 V maximum contact temperature becomes comparable to germanium melting point ($T_{melt} = 937$ °C). Naturally, temperature gradient reduces with increase in contact plane diameter and grows with increase in applied voltage (Fig. 3).

Knowing temperature gradient, one can determine characteristic length of its change L_T and temperature nonlocality length L_{Tnloc}. These results are represented in Figs. 4 – 5.

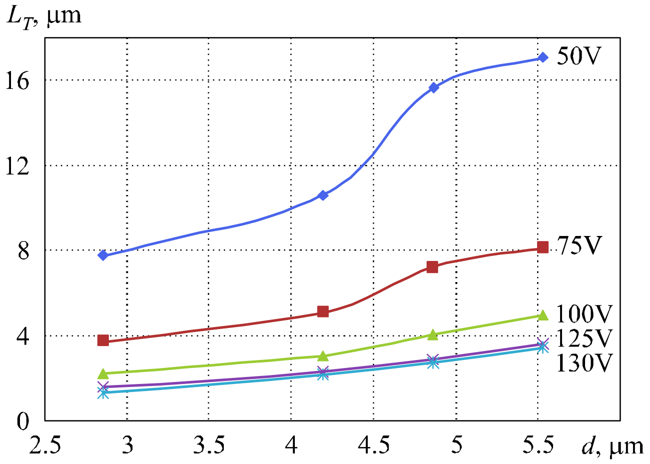

Fig. 4. Dependences of characteristic length of temperature change on contact plane diameter.

From Fig. 4 it is seen that the lowest L_T value in the model under consideration is achieved with a minimum contact diameter $d = 2.8$ μm and varies from 1.3 μm to 7.8 μm, whereas cooling length for *n-Ge* $L_o = 1.7$ μm [8]. It means that cooling length and characteristic length of temperature change are quite comparable. That is, under conditions at hand the processes of heat and electric charge transport become nonlinear. Now, inequality $L_o \ll L_T$ is not satisfied, and we have no right to use conventional linear transport equations, such as generalized Ohm's and Fourier's laws [12].

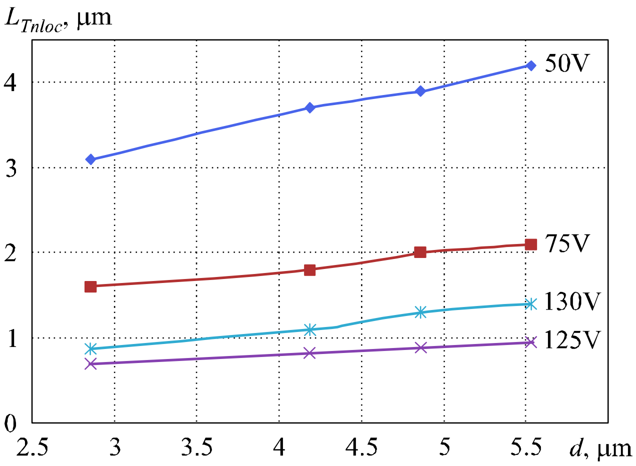

Fig. 5. Dependences of temperature nonlocality length on contact plane diameter.

An important role of nonlocality is illustrated in Fig. 5. We see that minimum values of nonlocality length L_{Tnloc} are also achieved with a minimum contact diameter $d = 2.8$ μm and make (0.7 – 0.9) μm, i.e. 2 – 7 times less than nonlinearity length L_T under the same conditions. Thus, computer simulation proves theoretical conclusions within a one-dimensional model [5-8] that the presence of nonlinear transport phenomena automatically brings about the emergence of nonlocal phenomena and vice versa, the presence of nonlocal summands automatically causes the emergence of nonlinear terms. Moreover, nonlocal phenomena can be even more important, like in the case under consideration, when the following inequality is satisfied

$$L_{Tnloc} < L_T. \tag{10}$$

Inequality (10) means that situations are possible when one can ignore the nonlinear phenomena ($L_0 << L_T$), but must already take into account the nonlocal effects ($L_{Tnloc} \sim L_T$). In general, in each specific case it is necessary to check the relative role of nonlinear and nonlocal phenomena using, for instance computer simulation.

There is a further point to be made. In the present model we calculated only the temperature field and were not interested in the electric field arising in the sample. In thermoelectric problems, the presence of temperature field brings about the appearance of corresponding electric (thermoelectric) field. And, in general, apart from nonlinearity and nonlocality lengths related to temperature (5), one should consider similar nonlinearity and nonlocality lengths due to electrochemical potential. However, if we restrict ourselves to thermoelectric problems, then in conformity with Seebecks's formula, characteristic nonlinearity and nonlocality lengths related to temperature and electrochemical potential, respectively, must be of the same order of magnitude [7]. Therefore, for the estimates it is sufficient to be restricted to the above approach. Certainly, for correct calculation of kinetic coefficients with regard to nonlinear and nonlocal phenomena, one should solve a self-consistent system of equations comprising energy balance equation and current-continuity equation with regard to the Seebeck and Peltier effects.

Mesoscopic and nanostructures are known to be promising thermoelectric materials. In such materials, the size of inhomogeneities (for instance, nanograins) can become comparable not only to characteristic length of temperature change, but also to nonlocality length. The effect of nonlocal phenomena on heat and electrotransport in semiconductor nanostructures has not been studied so far.

References

1. B.V. Alexeev, *Generalized Boltzmann Physical Kinetics* (Elsevier: 2004), 368 p.
2. B.V. Alexeev, Generalized Quantum Hydrodynamics and Principles of Non-Local Physics, *J. Nanoelectronics and Optoelectronics* **3** (2), 143 – 158 (2008).
3. B.V. Alexeev, Solution of the Dark Matter Problem in the Frame of the Non-Local Physics, *arXiv:1007.2800*, 2012
4. A.G. Samoilovich, *Thermoelectric and Thermomagnetic Methods of Energy Conversion* (compendium of lectures) (Chernivtsi: 2006), 227 p.
5. L.P. Bulat, Effect of Temperature Gradient on Electron Distribution Function in Semiconductors, *Semiconductors* **7** (11), 2181 – 2186 (1977).
6. L.P. Bulat, Thermoelectricity under Large Temperature Gradients, *J. Thermoelectricity* **4**, 3 – 34 (1997).
7. L.I. Anatychuk, L.P. Bulat, Semiconductors under Extreme Temperature Conditions (Saint-Petersburg: Nauka, 2001), 224 p.
8. L.I. Anatychuk, L.P. Bulat, Thermoelectric Phenomena under Large Temperature Gradients. In *"Thermoelectrics Handbook: Macro to Nano-Structured Materials"*. Ed. by D.M. Rowe. CRC Press, 2006, Chapter 3.
9. L.P. Bulat, E.I. Demchishin, Sasaki Phenomenon Thermoelectric Analogue and its Application to Thin Film Sensors, *Int. J. Electronics* **73** (5), 881-882 (1992).
10. L.P. Bulat, E.I. Demchishin, New Nonlinear Thermomagnetic Effects in Films and Sensors Based on These Effects, *Int. J. Electronics* **76** (5), 805-808 (1994).
11. L.I. Anatychuk, L.P. Bulat, New Nonlinear Thermoelectric, Heat-Conducting and Thermomagnetic Effects and their Classification, *J. Thermoelectricity* **1**, 41 – 55 (1998).
12. L.P. Bulat, I.A. Nefedova, On the Linear Thermoelectric Effects, *Bulletin of the International Academy of Refrigeration* **6**, 54-56 (2012).
13. L.P. Bulat, D.A. Pshenai-Severin, Tunneling Effect on Thermoelectric Figure of Merit of Bulk Nanostructured Materials, *Physics of the Solid State* **52** (3), 452 – 458 (2010).
14. L.P. Bulat, I.A. Drabkin, V.V. Karatayev, V.B. Osvenskii, Yu.N. Parkhomenko, M.G. Lavrentev, A.I. Sorokin, D.A. Pshenai-Severin, V.D. Blank, G.I. Pivovarov, V.T. Bublik, N.Yu. Tabachkova, Structure and Transport Properties of Bulk Nano-Thermoelectrics Based on $Bi_xSb_{2-x}Te_3$ Fabricated by SPS Method, *J. Electronic Materials*, 2013 (in press).
15. U. Ghoshal, S. Ghoshal, C. McDowell and L. Shi, Enhanced Thermoelectric Cooling at Cold Junction Interfaces, *Appl. Phys. Letters* **80** (16), 3006 – 3008 (2002).

Submitted 05.03.2013.

P.V. Gorsky, V.P. Mikhalchenko


P.V. Gorsky

Institute of Thermoelectricity
NAS and MES of Ukraine, 1, Nauky Str.,
Chernivtsi, 58029, Ukraine


V.P. Mikhalchenko

ON THE ELECTRIC CONDUCTIVITY OF CONTACTING PARTICLES OF THERMOELECTRIC MATERIAL

In the isotropic approximation the electric conductivity was calculated for a physical model – two half-spheres contacting in a circle with regard to electron scattering on the contact boundary as applied to Bi_2Te_3. It is shown that the value of effective electric conductivity of this material in the temperature range of 300 K and higher can be retained if contact radius exceeds 10.4 of mean free path of electron (hole). Calculated data are briefly discussed from the general physics and applied standpoints of thermoelectric material science.

Key words: thermoelectric material, extrusion, figure of merit, conductivity, shape-forming element, contact, boundaries, electrons, phonons, scattering.

Introduction

One of the most efficient conventional thermoelectric materials used today for the manufacture of working members of thermoelectric instruments and devices is bismuth telluride Bi_2Te_3. Its single crystals are traditionally prepared by one of the three methods, namely zone recrystallization, Czochralski pulling and oriented crystallization. The specific feature of Bi_2Te_3 single crystal is the presence of cleavage planes, along which it easily splits, by virtue of which with a reasonable degree of accuracy it can be considered to be layered. Besides, Bi_2Te_3 single crystal possesses a pronounced thermal conductivity and electric conductivity anisotropy. Thermal conductivity χ_{11} of this crystal along cleavage planes is 2 – 3 times larger than its thermal conductivity χ_{33} in the direction normal to these planes. Quite similarly, electric conductivity σ_{11} of Bi_2Te_3 along cleavage planes for *p*-type material is a factor of 2.7, and for *n*-type material – a factor of 4 – 6 larger than electric conductivity σ_{33} in the direction normal to cleavage planes. For this reason, to maximize thermoelectric figure of merit, thermoelectric modules of single crystals are made so that electric current and temperature gradient are parallel to cleavage planes.

Alongside with single-crystal materials, polycrystalline materials are used for the manufacture of thermoelectric modules. They can be divided into two classes: materials with oriented cleavage planes of individual crystallites and materials with a disordered (random) orientation of cleavage planes of individual crystallites. For the latter materials, according to the Odelevsky formula, electric conductivity is $\sigma = \sqrt{\sigma_{11}\sigma_{33}}$ and thermal conductivity is $\chi = \sqrt{\chi_{11}\chi_{33}}$.

Materials prepared by extrusion method in their structure are similar to polycrystalline materials with disordered orientation of cleavage planes of individual crystallites. Therefore, by virtue of the Odelevsky formula, in going from a single crystal to extruded material, the thermoelectric figure of merit must mostly drop. However, in actual practice such a drop is not observed. Hence, a mechanism must exist due to which material thermal conductivity drops, and electric conductivity is retained.

One of possible mechanisms of electric conductivity retention is quantum tunneling mechanism which manifests itself at small, i.e. comparable to electron (hole) de Broglie wavelength dimensions of thermoelectric material particles and contacts between them. The authors of [1] were among the first to pay attention to this fact. In [2] this mechanism was studied in more detail as applied to $Bi_xSb_{2-x}Te_3$. Exactly due to a large role of tunnelling effect in the formation of electric conductivity the researchers' attention is drawn to materials of the type TTF-TCNQ and similar to them with large carrier mobilities and the lowest lattice thermal conductivity [3-5].

At the same time, in the manufacture of thermoelectric products of conventional materials by hot pressing or extrusion, of current concern is a problem of optimal in terms of thermoelectric figure of merit dimensions of thermoelectric material grains and contacts between them. In particular, a question arises whether these dimensions can be selected so as to retain the electric conductivity of thermoelectric material particle aggregates with a simultaneous reduction of their thermal conductivity.

The form-shaping element of extruded material structure can be a system of two half-spheres of macroscopic radius R contacting in a circle of radius r [6]. The purpose of this work is to calculate the electric conductivity of such a system with regard to electrons or holes scattering on the contact boundaries.

Phenomenological consideration of the problem

Let us determine the effective electric conductivity of a system of two half-spheres of radius R of thermoelectric material contacting in a circle of radius r as a ratio of current through the system to potential difference between the large circles of half-spheres. A physical model of this problem is shown in Fig. 1.

In the formulation of the problem it is assumed that the surfaces of half-spheres are electrically isolated, their bases (large circle planes) are maintained at given potentials φ_1 and φ_2, and tunnelling of carriers to a gap between the spherical surfaces is ignored.

For the analytical calculation of potential distribution in such a system we will make direct use of Ohm's law. Let us direct the Z axis of coordinate system along the common axis of half-spheres. Then in the area of half-sphere with a larger potential from Ohm's law follows the equation:

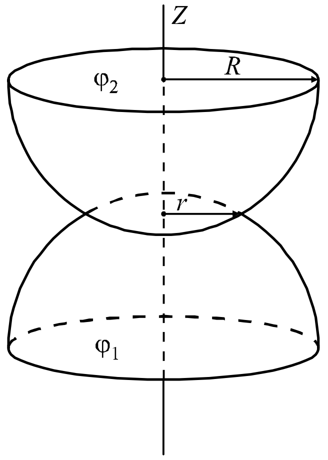

Fig. 1. Physical model of the problem.

$$-\sigma_0\pi\left(R^2-z^2\right)\frac{d\varphi}{dz}=I\ , \tag{1}$$

where σ_0 is known electric conductivity of half-sphere material, φ is potential, I is current through the system to be determined from the boundary conditions. The solution of Eq. (1) is of the form:

$$\varphi=\varphi_1-\frac{I}{2\sigma_0\pi R}\ln\frac{R+z}{R-z}\ . \tag{2}$$

Hence we find the contact potential:

$$\varphi_s = \varphi_1 - \frac{I}{2\sigma_0 \pi R} \ln \frac{R + \sqrt{R^2 - r^2}}{R - \sqrt{R^2 - r^2}} . \tag{3}$$

If, however, current coordinate varies within a half-sphere with a smaller potential $\sqrt{R^2 - r^2} \le z \le 2\sqrt{R^2 - r^2}$, from Ohm's law follows the equation:

$$-\sigma_0 \pi \left(R^2 - \left(2\sqrt{R^2 - r^2 - z} \right)^2 \right) \frac{\mathrm{d}\varphi}{\mathrm{d}z} = I . \tag{4}$$

Solution of Eq.(4) is given by:

$$\varphi = \varphi_1 - \frac{I}{\sigma_0 \pi R} \ln \frac{R + \sqrt{R^2 - r^2}}{R - \sqrt{R^2 - r^2}} - \frac{I}{2\sigma_0 \pi R} \ln \frac{R - 2\sqrt{R^2 - r^2} + z}{R + 2\sqrt{R^2 - r^2} - z} . \tag{5}$$

Satisfying condition $\varphi |_{z = 2\sqrt{R^2 - r^2}} = \varphi_2$, we get the following expression for current through the system:

$$I = \frac{\pi R \sigma_0 \left(\varphi_1 - \varphi_2 \right)}{\ln \left(\dfrac{R + \sqrt{R^2 - r^2}}{R - \sqrt{R^2 - r^2}} \right)} . \tag{6}$$

Therefore, the effective electric conductivity of a system of two half-spheres in S (Ω^{-1}) is equal to:

$$\sigma_{ef} = \frac{\pi R \sigma_0}{\ln \left(\dfrac{R + \sqrt{R^2 - r^2}}{R - \sqrt{R^2 - r^2}} \right)} . \tag{7}$$

At $r/R \ll 1$ this formula goes over into:

$$\sigma_{ef} = \frac{\pi R \sigma_0}{\ln \left(4R^2 / r^2 \right)} . \tag{8}$$

So, the final expression for potential distribution in a half-sphere with a larger potential is as follows:

$$\varphi = \varphi_1 - 0.5 \left(\varphi_1 - \varphi_2 \right) \frac{\ln \dfrac{R + z}{R - z}}{\ln \dfrac{R + \sqrt{R^2 - r^2}}{R - \sqrt{R^2 - r^2}}} . \tag{9}$$

Whereas in a half-sphere with a smaller potential this expression is given by:

$$\varphi = \varphi_2 + 0.5 \left(\varphi_1 - \varphi_2 \right) \frac{\ln \dfrac{R + 2\sqrt{R^2 - r^2} - z}{R - 2\sqrt{R^2 - r^2} + z}}{\ln \dfrac{R + \sqrt{R^2 - r^2}}{R - \sqrt{R^2 - r^2}}} . \tag{10}$$

Examples of potential fields in a system of two half-spheres are shown in Figs. 2 and 3. The Z axis is directed as in Fig. 1, i.e. from the base with a smaller potential to that with a larger potential. For simulation the values $\varphi_1 = 10$ V, $\varphi_2 = 0$ V, $R = 3$ and 4 mm, $r = 500$ and 25 μm were taken.

For comparison, crosses on the same plots are used to show the results of a numerical solution of Laplace's equation for a system of two half-spheres with the aid of "Comsol Multiphysics" program. The distinctions are mostly due to the error of difference approximation of differential operators with a numerical solution of second-order differential equations in partial derivatives by method of networks.

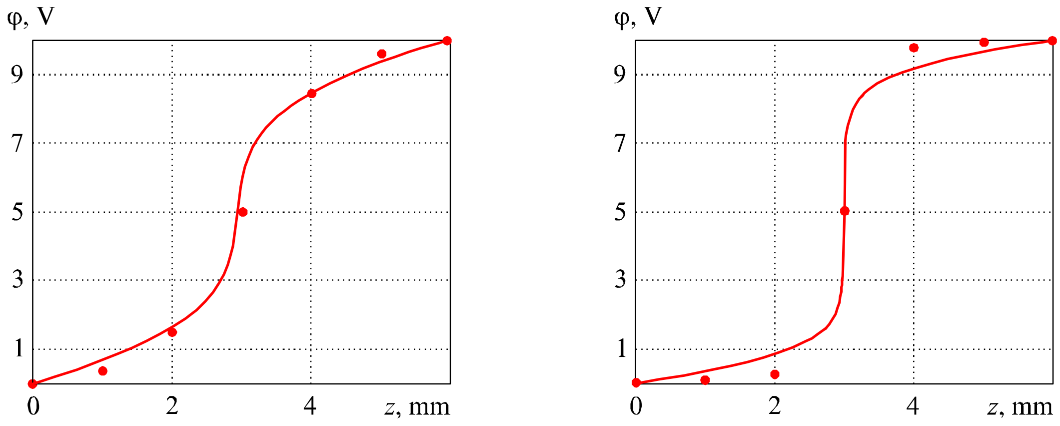

a) *b)*

Fig. 2. Results of a correlation between the numerical and analytical solutions at R = 3 mm and r = 500μm (a), 25 μm (b).

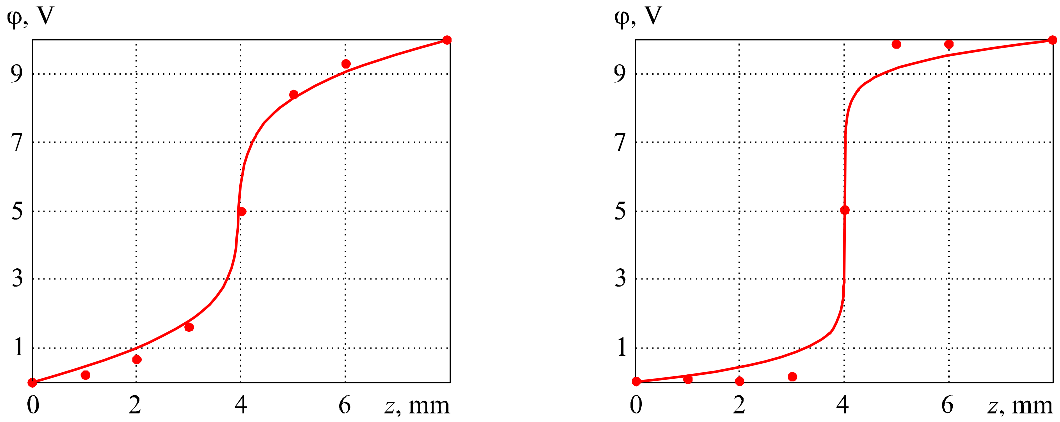

a) *b)*

Fig. 3. Results of a correlation between the numerical and analytical solutions at R = 4 mm and r = 500 μm (a) and 25 μm (b).

Dependence of current through the system (and its effective electric conductivity) on the ratio $b^* = r/R$ with a fixed radius of half-spheres is shown in Fig. 4.

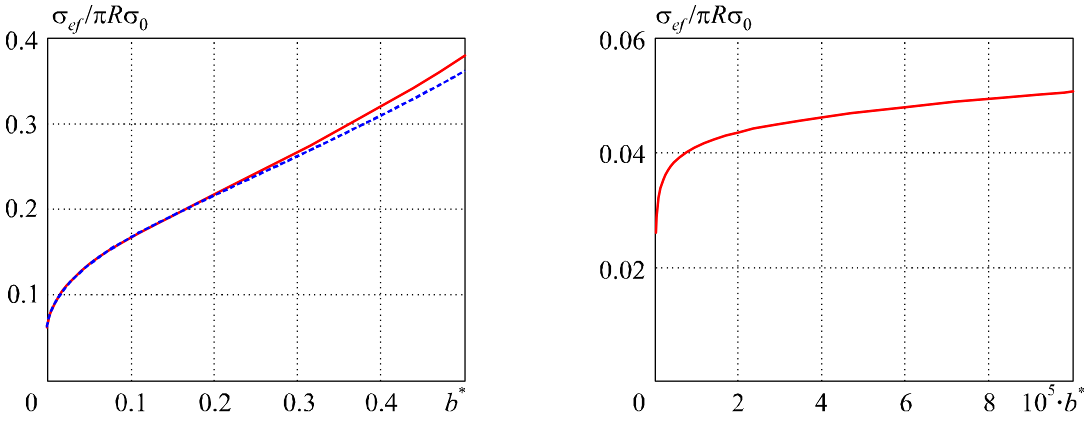

a) *b)*

Fig. 4. Dependence of effective electric conductivity of the system (and current through it) on the relative contact radius for moderate (a) and particularly small (b) radii. The dashed curve in Fig. 4 a is constructed by a simplified formula (8).

Thus, it follows from the results of phenomenological consideration of the problem that by virtue of similarity between thermal conductivity and electric conductivity effects, no gain in thermoelectric figure of merit can be obtained due to purely “geometric” factor, hence, it is necessary to consider the microscopic mechanism of system electric conductivity retention with a reduction of its thermal conductivity. In this case we will consider purely drift mechanism, thus far leaving aside quantum tunneling.

Consideration of the problem of electrons (holes) scattering on sample boundaries in the approximation of power dependence of relaxation time on energy

Consider this problem within a model of two half-spheres contacting in a circular spot of radius r . In the bulk material the mean free path l_{cc} of electron or hole depends on energy by the power law $l_{cc}(\varepsilon) = A\varepsilon^q$, where A is a certain coefficient of proportionality, q is power exponent. The values of these quantities are defined by specific scattering mechanism, where q, according to general concepts of quantum mechanics varies from 0 at low to 4 at high energies. Therefore, for the electric conductivity of the bulk sample in the isotropic approximation in the case of a nondegenerate gas of current carriers the following expression is valid:

$$\sigma_0 = D\left(kT\right)^{q+1}\int_0^\infty \exp\left(-x\right)x^{q+1}\mathrm{d}x = D\left(kT\right)^{q+1}\Gamma\left(q+2\right). \tag{11}$$

In this formula, $D = ABC\exp(\zeta/kT)$, B is coefficient of proportionality between the density of states of current carriers and the square root of their energy, C is coefficient of proportionality between the rate of current carriers and the square root of their energy, ζ is chemical potential, T is temperature, $\Gamma(x)$ is gamma-function.

For carrier scattering on the contact spot boundaries the following expression for the resulting mean free path of current carriers is valid:

$$l_{cct}\left(\varepsilon\right) = \frac{l_{cc}\left(\varepsilon\right)L}{L + l_{cc}\left(\varepsilon\right)}. \tag{12}$$

In this formula, $l_{cc}(\varepsilon)$ is mean free path of current carrier (electron or hole) in material determined by all scattering mechanisms, except for the contact spot boundaries, L is effective mean free path of current carrier determined by the sample boundaries. Now we introduce the mean free path of current carrier, for instance, electron, by the formula:

$$l_e = \frac{\int_0^\infty l_{cc}\left(\varepsilon\right)f_0\left(\varepsilon\right)g\left(\varepsilon\right)\mathrm{d}\varepsilon}{\int_0^\infty f_0\left(\varepsilon\right)g\left(\varepsilon\right)\mathrm{d}\varepsilon}. \tag{13}$$

In this formula, $f_0(\varepsilon)$ is the Maxwell-Boltzmann distribution function, $g(\varepsilon)$ is the electron density of states. From (12) follows the following relation for A:

$$A = l_e\frac{\Gamma\left(1.5\right)}{\left(kT\right)^q\Gamma\left(q+1.5\right)}. \tag{14}$$

In the case of a circular contact which is small as compared to half-sphere diameters, it can be considered that a drag of current carriers, for instance, electrons, takes place only in the area of this contact. Moreover, all contact points are equivalent due to its symmetry. Therefore, a general formula for electric conductivity [7] with regard to (12) and (14) yields the following expression for the ratio between the electric conductivity of a system of half-spheres to the electric conductivity of the bulk sample:

$$\frac{\sigma_{bs}}{\sigma_0}=\frac{1}{\pi\Gamma(q+2)}\int_0^{\infty}\int_0^{1}\int_0^{2\pi}\frac{k^*\sqrt{y^2+1-2y\cos\varphi}\,yx^{q+1}\exp(-x)}{x^q+k^*\sqrt{y^2+1-2y\cos\varphi}}\mathrm{d}\varphi\mathrm{d}y\mathrm{d}x\,. \tag{15}$$

In this formula, σ_{bs} is the electric conductivity of the system, $k^* = [\Gamma(q+1.5)/\Gamma(1.5)](r/l_e)$. As it must be, at $k^* = 0$ formula (13) gives zero, and at $k^* \to \infty$ – the electric conductivity of the bulk sample. The results of this calculation are depicted in Fig. 5.

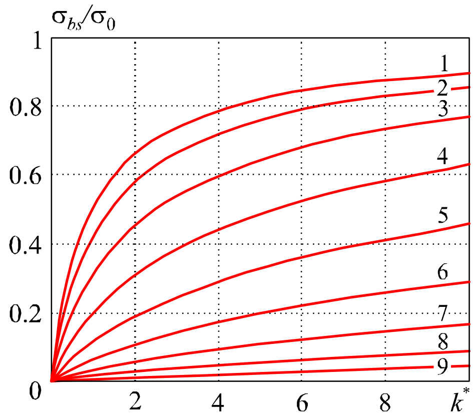

Fig. 5. Dependence of the electric conductivity of a system of two half-spheres contacting in a circular spot on its radius. Curves 1 – 9 are constructed for the values of q from 0 to 4 with a step of 0.5.

Dependence of r/l_e ratio on q following from considerations of retention of at least 90 % of the electric conductivity of the bulk sample is depicted in Fig. 6.

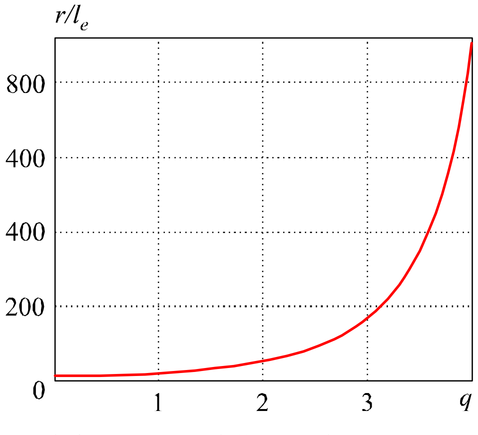

Fig. 6. Dependence of r/l_e ratio on q following from considerations of retention of at least 90 % of the electric conductivity of the bulk sample.

From this figure it is evident that with increase in q after the value equal to 2, r/l_e ratio is rather drastically increased. However, in semiconductors the most frequent q values are equal to 0, which corresponds to approximation of constant mean free path, or 0.5, which corresponds to approximation of constant relaxation time. In the temperature range of 300 K and above which is relevant for thermoelectricity it can be considered that $q = 0$. In this case the mean free path of current carriers, i.e. electrons (holes) l_{cc} at temperature T is expressed through their mobility b and density-of-state effective mass m^* as follows:

$$l_{cc} = \sqrt{\frac{\pi}{2}}\frac{b}{e}\sqrt{m^{*}kT}. \tag{16}$$

Therefore, the estimate of mean free paths at this temperature, based on the mobilities and density-of-state effective masses of electrons and holes [7], yields $l_e = 38.7$ nm, $l_h = 20.4$ nm. Minimum contact radius at $q = 0$, necessary for the retention of 90 % of electric conductivity, is 10.4 of the mean free path of electron or hole. And this corresponds (with a larger path) to 0.4 μm.

Conclusions and recommendations

1. In the isotropic drift approximation with regard to charge carrier scattering on the acoustic phonons and contact boundaries it is shown that in going from single crystal to extruded material the electric conductivity of shape-forming material structural element at least 90 % is retained, if the radius of contact between half-spheres is at least 10.4 of the mean free path of electron (hole).
2. As applied to Bi_2Te_3 at a temperature of 300 K it means that contact radius must be not less than 0.4 μm, and such contacts can occur between particles of diameter 40 to 80 μm.
3. Retention or slight change of thermoelectric figure of merit in going from single crystal to extruded material is attributable to the fact that at phonon scattering on the boundaries of contact between half-spheres of shape-forming element its thermal conductivity drops, while the electric conductivity even with account of charge carrier scattering on the contact boundaries remains the same.

The Authors express their gratitude to academician L.I. Anatychuk for the problem statement and important critical remarks.

References

1. N.S. Lidorenko, V.A. Andriyako, L.D. Dudkin, E.L. Nagayev, O.M. Narva, The Effect of Tunneling on the Efficiency of Thermoelectric Devices, *Doklady Akademii Nauk SSSR* **186**, 1295 (1969).
2. L.P. Bulat, D.A. Pshenai-Severin, Tunneling Effect on the Thermoelectric Figure of Merit of the Bulk Nanostructured Materials, *Semiconductors* **52,** 2010, 452.
3. A. Casian, V. Dusciac, and I. Coropceanu, Huge Carrier Mobilities Expected in Quasi-One-Dimensional Organic Crystals, *Phys. Rev. B* **66,** 165404, 1 – 5 (2002).
4. A.I. Casian, I.I. Balmush, and V.G. Dusciac, The Lorentz Number Reduction as a New Trend of *ZT* Increase in Quasi-One-Dimensional Organic Crystals, *J. Thermoelectricity* **3**, 19 – 28 (2011).
5. V. Dusciac, Thermoelectric Capabilities of Quasi-One-Dimensional Organic Semiconductors, *J. Thermoelectricity* **1**, 5 – 18 (2004).
6. A. Misnar, *Thermal Conductivity of Solids, Liquids, Gases and Their Compositions (*Moscow: Mir, 1968), 464 p.
7. B.M. Goltsman, V.A. Kudinov, and I.A. Smirnov, *Semiconductor Thermoelectric Materials Based on* Bi_2Te_3 (Moscow: Nauka, 1972), 320 p.

Submitted 16.01.2013.

P.I. Baranskii[1], **G.P. Haidar**[2]

[1]V.E. Lashkaryov Institute of Semiconductor Physics,
NAS Ukraine, 45, Nauky Ave., Kyiv, 03028, Ukraine;
[2]Institute for Nuclear Research, NAS Ukraine,
47, Nauky Ave., Kyiv, 03680, Ukraine


P.I. Baranskii


G.P. Haidar

ANISOTROPIC SCATTERING THEORY AND RELEVANT PROBLEMS OF THE KINETICS OF ELECTRON PROCESSES IN MANY-VALLEY SEMICONDUCTORS

This paper deals with the physics of anisotropic scattering theory. Researchers' attention is drawn to the advantageous features of this theory which made it suitable for practical application in the region of intermediate magnetic fields ($\mu H/c \approx 1$) where the use of other theories proved to be inefficient.

Key words: theory of anisotropic scattering, many-valley semiconductors, kinetic phenomena, electric and magnetic fields.

Introduction

Without exaggeration one may state that a real prerequisite to progress in some divisions of the kinetics of electron processes in semiconductors in our country (and abroad) over the last three to four decades has been development of anisotropic scattering theory (AST) efficiently pursued by its author, professor A.G. Samoilovich and his school of thought in Chernivtsi since 1960 and actually to the last day of his creatively rich and far from being easy life.*

Some AST divisions appeared in special editions [1-4] dealing with dedicated problems. Therefore, in this review it would not be inappropriate to set forth, possibly briefly and consecutively, the main postulates of AST, paying special attention to specific features of this theory assuring the opportunity of its application in such regions of magnetic field intensity (satisfying, in particular, criterion $\mu H/c \approx 1$) in which a description of electron gas kinetics for other theories is virtually impossible.

The most detailed and complete (so to speak, first-hand) AST outline can be found in the compendium of lectures by A.G. Samoilovich [5] prepared for publication by Anatoliy Grygorovich's pupils – L.N. Vikhor, O.A. Okhrem and A.O. Snarskii.

Note that the theoretical special course of AST (published as a compendium of lectures) is certainly self-sufficient and complete. However, being restricted by the scope of university program, it surely did not embody the results of experimental research pursued at the Lashkaryov Institute of Semiconductor Physics, NAS Ukraine with the active participation of theoreticians from Chernivtsi State University. It is exactly this gap in the interpretation of AST interaction with the experiment that the authors of this review would like to fill to some extent, referring, of course, only to scientific papers and monographs published with A.G. Samoilovich and the research officers of the department he was in charge of.

---

* At the age of 5 A.G. Samoilovich lost the opportunity not only to move without exterior help, but even to eat.

1. Physics of anisotropic scattering theory and its contribution to research on electron gas kinetics in many-valley semiconductors (*n*-type *Ge* and *Si*)

Research on the electric and galvanomagnetic properties of solids yields important information on the energy spectrum structure of carriers, the character of their scattering and other values describing transport effects. Knowledge of precise quantitative theory of these effects allows determination of a variety of parameters and enables a wide practical use of the electric and galvanomagnetic properties of solids in science and technology.

When considering electron motion in crystal lattice, it is necessary to take into account correctly the effective mass anisotropy and the anisotropy of electron scattering both on crystal lattice vibrations and on the ionized impurities.

The first successful step in this direction was taken in the work by Herring and Vogt [6]. In this work, the non-equilibrium addition to distribution function $n'_{\vec{k}}$ was taken in the form of a linear function of quasi-pulse $\vec{k}$

$$n'_{\vec{k}} = \vec{A}(\varepsilon)\vec{k}, \tag{1}$$

which is equivalent to taking into account only the first harmonic in the expansion of $n'_{\vec{k}}$ with respect to spherical functions, that is, use was made of a linear approximation. Being restricted to a linear approximation, it is impossible to evaluate the errors that arise. In the case of strongly anisotropic scattering (scattering on ionized impurities) such an approach is unacceptable altogether.

As will be shown below, within AST the solution of the kinetic equation has a reliable mathematical background. This method is equivalent to variation one. We will restrict ourselves to consideration of elastic scattering of electrons that have isoenergetic surfaces in the form of ellipsoids of revolution. The solution of the kinetic equation is sought as a series of expansion with respect to spherical functions and reduced to an infinite system of linear algebraic equations with respect to coefficients of this expansion.

To calculate the fluxes, it is necessary to determine the first harmonic coefficients in the system. When scattering probability in the axes of mass ellipsoid does not depend on the azimuth of vector $\vec{q}$ equal to a change in quasi-pulse at scattering, and the magnetic field is equal to zero, the first harmonic coefficients can be represented as a series where the first term gives a linear Herring-Vogt approximation. In the case of elongated isoenergetic ellipsoids of revolution ($m_{\parallel} > m_{\perp}$) at scattering on ionized impurities these series rapidly converge for any (considerable) $m_{\parallel} / m_{\perp}$ ratios, so it is enough to preserve two terms of the series. In the case of *Si* and *Ge* (as shown by estimates) at scattering on acoustic phonons it is enough to be restricted to the first term of expansion, because the second term is two orders of magnitude smaller than the first one. According to estimates, the last statement remains valid with a mixed scattering as well.

2. Solution of the kinetic equation with anisotropic electron scattering

2.1. Reduction of the kinetic equation to a system of algebraic equations (according to data reported in works [1 – 10])

Under anisotropic scattering conditions, the probability of $W_{\vec{k}\vec{k}'}$ transition from $\vec{k}$ state to $\vec{k}'$ state depends on $\vec{k}$ and $\vec{k}'$ directions. Such scattering can be caused either by the anisotropy of electron energy spectrum or by the anisotropic character of scatterer. We will consider only elastic scattering. Let us assume that the energy spectrum of electrons in the external electric field in the absence of a magnetic field ($H = 0$) is given by:

$$\varepsilon = \sum_{i=1}^{3} \frac{\hbar^2 k_i^2}{2\, m_i}. \tag{2}$$

Then with the weak electric field and temperature gradient (grad T), in conformity with [2, 3, 7 – 10], the kinetic equation can be written as

$$\hat{D}\, n^{(0)}_{\vec{k}} + \hat{R}\, n'_{\vec{k}} = 0\,, \tag{3}$$

where

$$\hat{R}\, n'_{\vec{k}} = \sum_{\vec{k}'} W_{\vec{k}\vec{k}'} \left(n'_{\vec{k}'} - n'_{\vec{k}} \right), \tag{4}$$

where $n^{(0)}_{\vec{k}}$ is equilibrium distribution function, $n'_{\vec{k}}$ is nonequilibrium addition to distribution function, $\hat{R}$ is collision operator, $\hat{D}\, n^{(0)}_{\vec{k}}$ is a free term of the kinetic equation

$$\hat{D}\, n^{(0)}_{\vec{k}} = \frac{1}{\hbar} \frac{\partial n^{(0)}_{\vec{k}}}{\partial \varepsilon} \sum_i \left(\frac{\partial \mu}{\partial x_i} + \frac{\varepsilon - \mu}{T} \frac{\partial T}{\partial x_i} - e E_i \right) \frac{\partial \varepsilon}{\partial k_i}\,, \tag{5}$$

μ is chemical potential, E is external electric field.

The kinetic equations are solved for each isoenergetic ellipsoid taken individually (Umklapp processes between minima are disregarded).

Let us introduce "deformed" coordinates in quasi-pulse space

$$\xi_i = \frac{\hbar}{\sqrt{2\, m_i\, \varepsilon}}\, k_i\,. \tag{6}$$

Then expression (2) will be of the form

$$\sum_i \xi_i^2 = 1\,. \tag{7}$$

Let us introduce a spherical coordinate system with a polar axis oriented along $0Z$ axis of constant energy ellipsoid

$$\xi_1 = \sin\vartheta_0 \cos\phi_0\,,\ \xi_2 = \sin\vartheta_0 \sin\phi_0\,,\ \xi_3 = \cos\vartheta_0\,. \tag{8}$$

In this case, denoting through

$$K_i = -\frac{\partial \mu}{\partial x_i} - \frac{\varepsilon - \mu}{T} \frac{\partial T}{\partial x_i} + e E_i\,, \tag{9}$$

one can write a free term of the kinetic equation as

$$\hat{D}\, n^{(0)}_{\vec{k}} = \sum_m D_m\, Y_{1m} \left(\vartheta_0\, \phi_0 \right), \tag{10}$$

where $Y_{lm} \left(\vartheta_0\, \phi_0 \right)$ is a spherical function normalized to unity.

$$\left. \begin{aligned} D_1 &= \sqrt{\frac{4\pi\varepsilon}{3}}\, \frac{\partial n^{(0)}_{\vec{k}}}{\partial \varepsilon} \left(\frac{K_1}{\sqrt{m_1}} - \frac{i}{\sqrt{m_2}} K_2 \right) \\ D_0 &= \sqrt{\frac{8\pi E}{3\, m_3}}\, \frac{\partial n^{(0)}_{\vec{k}}}{\partial \varepsilon} K_3, \qquad D_{-1} = -D_1^* \end{aligned} \right\} . \tag{11}$$

With regard to equation (10), it is natural to seek the solution of the kinetic equation as expansion with respect to spherical functions

$$n'_{\vec{k}} = \sum_{k\,m} X_{k\,m}(\varepsilon)\, Y_{k\,m}(\vartheta_0\, \phi_0)\,. \tag{12}$$

As long as under elastic scattering conditions a collision operator affects only the angular part of function $n'_{\vec{k}}$, we get

$$\hat{R}\, n'_{\vec{k}} = -\sum_{j\,k\,m\,p} X_{k\,m}(\varepsilon)\; B_{j\,k}(p\,m)\; Y_{j\,p}(\vartheta_0\, \phi_0)\,, \tag{13}$$

where

$$-\sum_{j\,p} B_{j\,p}(p\,m)\, Y_{j\,p}(\vartheta_0\, \phi_0) = \hat{R}\, Y_{k\,m}(\vartheta_0\, \phi_0)\,. \tag{14}$$

Substituting (10) and (13) into (3), we obtain a system of equations in unknowns $X_{k\,m}(\varepsilon)$

$$\sum_{k\,m} B_{j\,k}(p\,m)\, X_{k\,m} = D_p\; \delta_{j1}\,. \tag{15}$$

Thus, the problem of finding $n'_{\vec{k}}$ from equation (3) came down to determination of $X_{k\,m}$ from the infinite system of linear algebraic equations (15). Current components are proportional to first-order spherical functions. Hence, for current calculation it is enough to find X_{1m} from the reduced system. Part of distribution function $n'_{\vec{k}}$ whereby current is determined is of the form

$$n'_{\vec{k}} = \sum_{m} X_{1m}(\varepsilon)\, Y_{1m}(\vartheta_0\, \phi_0). \tag{16}$$

Based on the principle of microscopic reversibility it can be shown that expansion (12) includes only unpaired harmonics.

Note that a system of equations (15) can be also obtained using the principle of entropy growth rate maximum.

As a result of collision operator action on the angular part of function $n'_{\vec{k}}$ and performing the necessary calculations [8, 9], the expression for coefficients $B_{j\,k}(p\,m)$ was obtained as below:

$$\begin{gathered} B_{j\,k}(p\,m) = \frac{4\sqrt{2\,m_1\, m_2\, m_3\, \varepsilon}}{(2\pi\hbar)^3}\, i^{m-p} \sum_{s_{paired}} \sqrt{\frac{(2\,j+1)\;(2\,k+1)\;(j-s)!\;(k-s)!}{(j+s)!\,(k+s)!}}\; \times \\ \times \int d\,\Omega \int_0^{\pi/2} d\theta \sin\theta \cos\theta\;\, W(\theta\,\vartheta\,\phi)\, P_j^s(\cos\theta)\, P_k^s(\cos\theta)\, P_{s\,p}^{j}(\cos\vartheta)\, P_{s\,m}^{*\,k}(\cos\vartheta)\, e^{i(m-p)\phi}. \end{gathered} \tag{17}$$

Summation in (17) over S_{pair} is done from $-k+1$ to $k-1$, when $k<j$; and from $-j+1$ to $j-1$, when $j<k$; P_j^s is an associated Legendre function; $P_{s\,p}^{j}$ is an orbital part of generalized spherical function (Wigner function) determined in [11]. $d\,\Omega = \sin\vartheta\, d\vartheta\, d\phi$. ϑ_0 and φ_0 determine a direction $\vec{\xi}$ of electron quasi-pulse in "deformed" coordinate system (6) up to scattering, ϑ and φ determine a direction of vector $\vec{q} = \vec{\xi} - \vec{\xi}'$ equal to a change in quasi-pulse on scattering, $\chi = \pi - 2\theta$ is scattering angle, that is, the angle between $\vec{\xi}$ and $\vec{\xi}'$ (Fig. 1).

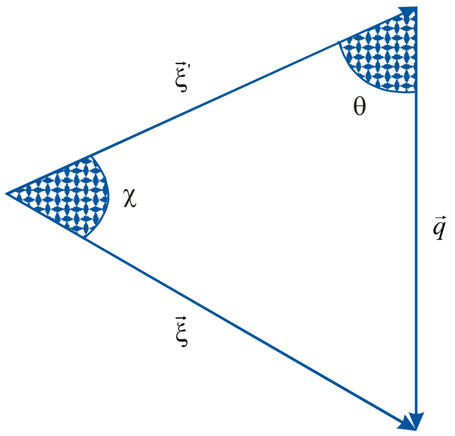

Fig. 1. Schematic of scattering angle χ.

When probability of scattering in the axis of mass ellipsoid does not depend on vector azimuth $\vec{q}$ (on angle φ), then matrix $\left\| B_{jk}\left(pm\right) \right\|$ is diagonalized in p and m:

$$B_{jk}\left(pm\right) = B_{jk}\left(p\right)\delta_{mp}. \tag{18}$$

In so doing, system (15) is disintegrated into independent systems with different p:

$$\sum_k B_{jk}\left(p\right) X_{kp} = D_p \delta_{j1}. \tag{19}$$

Accordingly, $W(\theta\ \vartheta\ \varphi)$ in (17) will not depend on φ and we will get:

$$\begin{gathered} B_{jk}\left(pm\right) = B_{jk}\left(m\right)\delta_{mp} = \frac{\sqrt{2m_1 m_2 m_3 \varepsilon}}{\pi^2 \hbar^3} \sum_{s_{paired}} \sqrt{\frac{\left(2j+1\right)\left(2k+1\right)\left(j-s\right)!\left(k-s\right)!}{\left(j+s\right)!\left(k+s\right)!}} \times \\ \times \int_0^{\pi} d\vartheta \sin\vartheta \int_0^{\pi/2} d\theta \sin\theta\cos\theta\ W\left(\theta,\vartheta\right) P_j^s\left(\cos\theta\right) P_k^s\left(\cos\theta\right) P_{sm}^j\left(\cos\vartheta\right) P_{sm}^{*k}\left(\cos\vartheta\right) \times \delta_{mp}. \end{gathered} \tag{20}$$

As is evident from (17),

$$B_{jk}\left(pm\right) = B_{kj}^{*}\left(mp\right). \tag{21}$$

Using an explicit expression for functions $P_{sm}^j\left(\cos\vartheta\right)$ [11], it is readily apparent from (20) that coefficients $B_{jk}\left(m\right)$ (as real ones) meet the condition

$$B_{jk}\left(m\right) = B_{kj}\left(m\right), \tag{22}$$

and, with regard to (20), one can also write

$$B_{jk}\left(m\right) = B_{jk}\left(-m\right). \tag{23}$$

2.2. Iteration method for determination of X_{1m}

A method for calculation of X_{1m} that will be set forth below can be efficiently used to find X_{1m} from system (19).

Let *B(XX)* be a quadratic form of variables X_{lm}

$$B\left(XX\right) = \sum_{jk} B_{jk} X_j X_k \tag{24}$$

(index *m* is omitted as yet).

Let us introduce the notation

$$A_i(X) = \sum_k B_{ik} X_k, \tag{25}$$

$$Z_1 = A_1(X), \quad Z_k = \begin{vmatrix} B_{11} & B_{13} & \cdots & B_{1,2k-3} & A_1(X) \\ B_{31} & B_{33} & \cdots & B_{3,2k-3} & A_3(X) \\ \cdots & \cdots & \cdots & \cdots & \cdots \\ B_{2k-1,1} & B_{2k-1,3} & \cdots & B_{2k-1,2k-3} & A_{2k-1}(X) \end{vmatrix}. \tag{26}$$

In conformity with the Jacobi formula

$$B(XX) = \sum_l \frac{Z_l^2}{\Delta_l \, \Delta_{l-1}}, \tag{27}$$

where Δ_l is determinant of the principal "l"-th minor matrix $\| B_{jk} \|$. However, in our case variables X_{1m} meet system (18), therefore

$$A_1(X) = D, \; A_{i>1} = 0, \; B(XX) = D X_1. \tag{28}$$

Thus, for c we obtain from (27) the following series

$$X_{1m} = D_m \sum_l \frac{\bar{Z}_{l-1}^2}{\Delta_l(m) \; \Delta_{l-1}(m)}, \tag{29}$$

where

$$\bar{Z}_{l-1}^{(m)} = \begin{vmatrix} B_{31}(m) & B_{33}(m) & \cdots & B_{3,2l-3}(m) \\ \cdots & \cdots & \cdots & \cdots \\ \cdots & \cdots & \cdots & \cdots \\ B_{2l-1,1}(m) & B_{2l-1,3}(m) & \cdots & B_{2l-1,2l-3}(m) \end{vmatrix}; \; \bar{Z}_0 = 1. \tag{30}$$

The sum of the first n terms of series for X_{1m} is a solution of system (19), if we set $X_{lm} = 0$ at $l > n$. In this sense, said method for calculation of X_{1m} can be referred to as iteration. Note that series (29) when considering scattering on phonons and impurity ions is rapidly converging. For instance, at scattering on ionized impurities in the case of strongest anisotropy (when scattering is mainly forward and $m_1 / m_3 << 1$) the ratio of the first four terms in this series is as follows: 1: 0.72: 0.015: 0. Here, the nondiagonal matrix elements $\| B_{jk}(m) \|$ are not small.

2.3. Scattering on ionized impurities

Let us consider a dielectric constant ς isotropic and assume impurity potential as

$$V = \frac{e_0^2}{\varsigma r} e^{-r/a}, \tag{31}$$

where e_0 is electron charge, a is screening radius which in the degenerate case is calculated by the formula

$$a^{-2} = \frac{4\pi e_0^2 n'}{\varsigma k T}, \tag{32}$$

where $n' = n + (n + N_A)\left(1 - \frac{n + N_A}{N_D}\right)$. Here n is electron concentration in conduction band, N_D and N_A are donor and acceptor concentrations. The n' value, according to Brooks [12], takes into account the effect of compensating impurity on screening.

Under these conditions, in the Born approximation, for matrix transition element we get

$$V_{\vec{k}\,\vec{k}'} = \frac{e_0^2}{\varsigma}\int e^{i\left(\vec{k}-\vec{k}',\,\vec{r}\right)}\,\frac{e^{-r/a}}{r}\,d\vec{r} = \frac{4\pi e_0^2}{\varsigma}\,\frac{1}{\left(\vec{k}-\vec{k}'\right)^2 + a^{-2}}. \tag{33}$$

If $\left(\vec{k}-\vec{k}'\right)^2$ is expressed through angles θ, ϑ and φ (see explanations to (17)), in the case of ellipsoid of revolution we obtain the following expression for transition probability

$$W(\theta\vartheta\phi) = \frac{2\pi}{\hbar}N\left|V_{\vec{k}\,\vec{k}'}\right|^2 = \frac{\pi^3 e_0^4 N\hbar^3}{2\varepsilon^2 m_3^2\chi^2\left[\left(\cos^2\vartheta + \frac{m_1}{m_3}\sin^2\vartheta\right)\cos^2\theta + \gamma^2\right]^2}, \tag{34}$$

where

$$\gamma^2 = \frac{\hbar^2}{8a^2 m_3\varepsilon}, \tag{35}$$

N is the number of ionized impurities per 1 cm^3, $m_1 = m_2 < m_3$.

Parameter γ^2 in the region of $5 \le T \le 300$ K and $10^{14} \le N_D \le 10^{17}$ cm^{-3} is in the range of $10^{-7} \le \gamma^2 \le 10^{-2}$. With that sort of low γ^2 an angular summand in denominator (34) is essential, since the probability of scattering for certain angle χ (scattering angle $\chi = \pi - 2\theta$) with real values m_1/m_3 is strongly dependent on angle ϑ, that is, on the direction of electron motion.

As long as in our case $W(\theta\,\vartheta\,\varphi)$ does not depend on φ, coefficients $B_{jk}(pm) = B_{jk}(m)\,\delta_{pm}$ (see (18)) – X_{1m} can be determined by means of series (29). In the boundary case of low but finite γ^2 and m_1/m_3 we get

$$X_{10} = \frac{D_0}{\tilde{B}_{11}(0)}\left(1 + 0.72 + 0.015 + 0.00018 + \ldots\right). \tag{36}$$

The values of $\tilde{B}_{jk}(m)$ for $m = 0.1$ are given in Tables 1 and 2.

<u>*Table 1*</u>

The values of coefficients $\frac{\tilde{B}_{jk}(0)}{\tilde{B}_{11}(0)}$ *at certain j and k*

j	*k*			
	1	3	5	7
1	1	3.44	6.74	10.7
3	3.44	28.2	59.2	96.0
5	6.74	59.2	169	287
7	10.7	96.0	287	576

Table 2

The values of coefficients $\frac{\tilde{B}_{jk}(1)}{\tilde{B}_{11}(1)}$ *at certain j and k*

j	*k*		
	1	3	5
1	1	1.40	1.74
3	1.40	4.70	6.24
5	1.74	6.24	11.4

For larger γ^2 and m_1/m_3 values, when the anisotropy is lower, series (29), naturally, converges even better. If we use an evaluation formula where we substitute $m_1/m_3 = 0.052$ for *Ge* and $m_1/m_3 = 0.196$ for *Si*, the second term in (29) will be equal to 0.38 and 0.15 respectively, and the third term $\cong 10^{-3}$ in both cases.

Similarly, for X_{11} in the boundary case of low but finite γ^2 and m_1/m_3, we obtain

$$X_{11} = \frac{D_1}{\tilde{B}_{11}(1)}\left(1 + 0.72 + 0.015 + \ldots\right). \tag{37}$$

For *Ge* and *Si* the second term in (37) will be equal to 0.50 and 0.18, respectively. So, both for X_{10} and X_{11} we can restrict ourselves to two terms of the series.

Restricting ourselves in (29) to the second term, we will have

$$X_{1m} = D_m\,\chi_m, \tag{38}$$

where

$$\chi_m = \frac{1}{B_{11}(m)}\left[1 + \frac{B_{13}^2(m)}{B_{11}(m)\,B_{33}(m) - B_{13}^2(m)}\right], \tag{39}$$

in which case $\chi_1 = \chi_{-1}$. Taking into account (21) and (38), we will get the following expressions for components of relaxation time tensor

$$\left.\begin{aligned} \tau_{\parallel} = \tau_{33} = \chi_0 = \frac{1}{B_{11}(0)}\left(1 + g_0\right) \\ \tau_{\perp} = \tau_{11} = \chi_1 = \frac{1}{B_{11}(1)}\left(1 + g_1\right) \end{aligned}\right\}, \tag{40}$$

where

$$g_m = \frac{B_{13}^2(m)}{B_{11}(m)\;B_{33}(m) - B_{13}^2(m)}. \tag{41}$$

In the isotropic case ($m_1/m_3 = 1$) all $B_{jk}(m) = 0$ at $j \neq k$ and formulae (40) give us relaxation time obtained by Brooks and Herring [12] and Dingle [13]:

$$\tau^{-1} = \frac{\pi\, e_0^4\, N}{\varsigma^2\,\sqrt{2m^*\varepsilon^3}}\left(\ln\frac{1+\gamma^2}{\gamma^2} - \frac{1}{1+\gamma^2}\right). \tag{42}$$

Note that all coefficients $B_{jk}(m)$ can be precisely calculated and are rather complicated and cumbersome expressions. However, as it turned out, in the calculation of $B_{jk}(m)$ for *Ge* and *Si* one can make an expansion with respect to parameter $\alpha^2 = \gamma^2 m_3/m_1$ and omit all α^2 and higher-order terms, since, in practically most important region, $\gamma^2 \leq 10^{-2}$. The obtained coefficients $B_{jk}(m)$ can be used for calculation of correction g_m by formula (39) in the cases when scattering on impurity ions prevails over other scattering mechanisms (heavily compensated samples, low temperatures, etc.).

2.4. Scattering on acoustic phonons

Based on deformation potential theory [6] and the results of Ref. [14], the probability of scattering for *Ge* and *Si* is of the form

$$W(\vartheta)=\frac{2\pi kTC_1^2}{C_{11}^{'}\hbar}\left\{\begin{array}{l}1+\dfrac{2C_2m_3\cos^2\vartheta}{C_1\left(m_1\sin^2\vartheta+m_3\cos^2\vartheta\right)}+\dfrac{C_2^2m_3^2\cos^4\vartheta}{C_1^2\left(m_1\sin^2\vartheta+m_3\cos^2\vartheta\right)^2}+\\+\dfrac{C_2^2\,C_{11}^{'}\,m_1\,m_3\,\sin^2\vartheta\,\cos^2\vartheta}{C_1^2\,C_{44}^{'}\left(m_1\sin^2\vartheta+m_3\cos^2\vartheta\right)^2}\end{array}\right\},\tag{43}$$

where C_1 and C_2 are deformation potential constants, $C_{11}^{'}$ and $C_{44}^{'}$ are averaged elastic constants determined in [14].

As can be seen from (43), W does not depend on angle θ, hence, on scattering angle either. Coefficients $B_{jk}(m)$ are calculated by the formula

$$B_{jk}(m)=\frac{4m_1\sqrt{2m_3\varepsilon}}{(2\pi\hbar)^3}\sum_{s_{paired}}L_{jk}^s\,R_{jk}^s(m),\tag{44}$$

where

$$\left.\begin{array}{l}L_{jk}^s=2\sqrt{\dfrac{(j-s)!(k-s)!}{(j+s)!(k+s)!}}\displaystyle\int_0^{\pi/2}d\theta\sin\theta\cos\theta\,P_j^{*s}(\cos\theta)\,P_k^s(\cos\theta)\\R_{jk}^s(m)=\displaystyle\int d\Omega\;\overline{P}_{sm}^{j}(\cos\vartheta)\,\overline{P}_{sm}^{*k}(\cos\vartheta)\end{array}\right\},\tag{45}$$

$\overline{P}_{sm}^{j}(\cos\vartheta)$ are functions normalized to unity.

A matrix of coefficients $B_{jk}(m)$ in this case is very close to the diagonal one, so in series (29) for X_{1m} the second term can be already omitted, since it is two orders of magnitude smaller than the first one for *Ge* and *Si*.

The respective $B_{11}(m)$ values, according to (44) and (45), will be given by

$$B_{11}(m)=\frac{1}{\tau_0}S_m,\tag{46}$$

where "isotropic" relaxation time τ_0:

$$\tau_0=\frac{\pi C_{11}^{'}\hbar^4}{kTC_1^2\sqrt{2m_1^2m_3\varepsilon}},\tag{47}$$

$$\begin{aligned}S_0&=1+\frac{2C_2m_3}{C_1m_1\beta^2}\left(1-\frac{3}{\beta^2}+\frac{3}{\beta^3}b\right)+\frac{m_3C_2^2}{m_1C_1^2\beta^4}\times\\&\times\left\{\frac{m_3}{m_1}\left(1-\frac{6}{\beta^2}-\frac{3m_1}{2\beta^2m_3}+\frac{15}{2\beta^3}b\right)+\frac{C_{11}^{'}}{C_{44}^{'}}\left[2+\frac{15}{2\beta^2}-\frac{3b}{2\beta^3}\left(5+3\beta^2\right)\right]\right\},\end{aligned}\tag{48}$$

$$\begin{aligned}S_1&=1+\frac{C_2m_3}{C_1m_1\beta^2}\left(2-\frac{3}{\beta^2}+\frac{3bm_3}{m_1\beta^3}\right)+\frac{m_3C_2^2}{m_1C_1^2\beta^4}\times\\&\times\left\{\frac{m_3}{m_1}\left(1+\frac{15}{4\beta^2}-\frac{3b}{4\beta^3}\left(5+3\beta^2\right)\right)-\frac{C_{11}^{'}}{4C_{44}^{'}}\left[13+\frac{15}{\beta^2}-\frac{3}{\beta^3}\left(5+6\beta^2+\beta^4\right)b\right]\right\}.\end{aligned}\tag{49}$$

Here, $\beta^2 = \dfrac{m_3 - m_1}{m_1}$, $b = arctg\ \beta$.

Relaxation time tensor is given by

$$\tau_{11} = \tau_{22} = \tau_{\perp} = \frac{1}{B_{11}(1)} = \frac{\tau_0}{S_1}; \ \ \tau_{33} = \tau_{\|} = \frac{1}{B_{11}(0)} = \frac{\tau_0}{S_0}. \tag{50}$$

2.5. Mixed scattering

In the case of mixed scattering, coefficients $B_{jk}(m)$ (owing to summation of transition probabilities) will be as follows

$$B_{jk}(m) = B^{f}_{jk}(m) + B^{ion}_{jk}(m), \tag{51}$$

where $B^{f}_{jk}(m)$ and $B^{ion}_{jk}(m)$ are coefficients corresponding to scattering on phonons or impurity ions only. The second term of series (29) for X_{1m} (designated as g_m) will be determined by the relationship

$$g_m = \frac{\left(B^{f}_{13}(m) + B^{ion}_{13}(m)\right)^2}{\left(B^{f}_{11}(m) + B^{ion}_{11}(m)\right)\left(B^{f}_{33}(m) + B^{ion}_{33}(m)\right) - \left(B^{f}_{13}(m) + B^{ion}_{13}(m)\right)^2}. \tag{52}$$

As long as a matrix of coefficients $\left\| B^{\phi}_{jk}(m) \right\|$ (as mentioned above) is almost diagonal, from (52) it is seen that correction g_m in this case is much smaller than in the case of purely ion scattering. Analysis shows that g_m with a mixed scattering is of the order of several percent for *Ge* and *Si* in the entire practically important range of temperatures and impurity concentrations. Therefore, for the case of mixed scattering (and this kind of scattering in actual practice is very frequent) it is enough in series (29) for X_{1m} to be restricted to the first term (linear approximation).

3. The use of AST for study of thermoelectric and thermomagnetic effects in anisotropic semiconductors

As long as the theory of thermoelectric and thermomagnetic effects within the assumptions used here was published in full scope as a separate edition [3], we will restrict ourselves to several general comments related to practical use of this theory (by comparison of its conclusions to the experiment).

In the framework of assumptions accepted in the band theory and AST, in said edition a general theory of galvano- and thermomagnetic effects was built for arbitrary-value (but non-quantizing) magnetic fields. In so doing, the kinetics of electron processes in many-valley semiconductors was considered both in the presence and absence of electron phonon drag effects.

It turned out that qualitative and quantitative analyses of the entire combination of considered effects can be carried to completion with restriction to two parameters that are well measured experimentally: mobility anisotropy parameter $K = \mu_{\perp}/\mu_{\|}$ and drag thermoEMF anisotropy parameter $M = \alpha_{\|}^{\Phi}/\alpha_{\perp}^{\Phi}$, which characterize an isoenergetic ellipsoid taken individually.

The use of uniaxial elastic deformation (with application to crystal and a change in deforming mechanical stress X in rather wide limits) assures the analysis of effects under study with a different number of efficient isoenergetic ellipsoids: from one (*n-Ge*, deformed in <111> direction) to six (*n-Si* – in the non-deformed crystal).

However, there are many semiconductors whose isoenergetic surfaces are shaped not as ellipsoids of revolution, but as three-axial ellipsoids (and even more complicated). In monograph [3], the necessary generalizations of the theory appropriate for the description of kinetic effects in these (far from being simple) cases were made and can employed for comparison of experimental data to the theory.

Conclusions

1. The basic postulates of anisotropic scattering theory (AST) are formulated and the most important formulae of this theory are given in a form convenient for practical use by comparison to the experimental data.
2. Possibilities of AST practical use in the investigation of thermoelectric and thermomagnetic effects in many-valley semiconductors of the type *n-Si* and *n-Ge* are explored.
3. The specific feature of AST is pointed out, namely its suitability for the description of the kinetics of electron processes not only in the region of near-boundary small or boundary large (non-quantizing) magnetic fields H, but also in the region of intermediate magnetic fields (that is, at $\mu H/c \approx 1$), where the use of other theories is inefficient.

References

1. P.M. Tomchuk, Anisotropic Scattering of Current Carriers in Semiconductors, *Ukr. J. Physics* **13** (8), 1366 – 1377 (1968).
2. P.I. Baranskii, I.S. Buda, I.D. Dakhovsky, and V.V. Kolomoyets, *Electric and Galvanomagnetic Effects in Anisotropic Semiconductors* (Kyiv: Naukova Dumka, 1977), 270 p.
3. P.I. Baranskii, I.S. Buda, and I.V. Dakhovsky, *Theory of Thermoelectric and Thermomagnetic Effects in Anisotropic Semiconductors* (Kyiv: Naukova Dumka, 1987), 272 p.
4. P.I. Baranskii, I.S. Buda, and V.V. Savyak, *Thermoelectric and Thermomagnetic Effects in Many-Valley Semiconductors* (Kyiv: Naukova Dumka, 1992), 268 p.
5. L.M. Vikhor, O.A. Okhrem, A.O. Snarskii, *Thermoelectric and Thermomagnetic Methods of Energy Conversion, Compendium of Lectures by Professor A.G.Samoilovich* (Chernivtsi: Ruta, 2006), 228 p.
6. C. Herring, E. Vogt, *Problems of Semiconductor Physics* (Moscow: Inoizdat, 1957), 567 p.
7. A.G. Samoilovich, I.Ya. Korenblit, and I.V. Dakhovsky, *Doklady AN SSSR* **139** (2), 355 – 358 (1961).
8. A.G. Samoilovich, I.Ya. Korenblit, I.V. Dakhovsky, and V.D. Iskra, Solution of Kinetic Equation with Anisotropic Scattering of Electrons, *Physics of the Solid State* **3** (10), 2939 – 2952 (1961).
9. A.G. Samoilovich, I.Ya. Korenblit, I.V. Dakhovsky, V.D. Iskra, Anisotropic Scattering of Electrons on Ionized Impurities and Acoustic Phonons, *Physics of the Solid State* **3** (11), 3285 – 3298 (1961).
10. I.V. Dakhovsky, Anisotropic Scattering of Electrons in Germanium and Silicon, *Physics of the Solid State* **5** (8), 2332 – 2338 (1963).
11. I.M. Gelfand, R.A. Minlos, and Z.Ya. Shapiro, *Representations of the Rotation Group and Lorentz Group* (Moscow: Fizmatgiz, 1958), 367 p.
12. G. Brooks, Problems of Modern Physics: Collected Translations (Moscow: Inoizdat, 1957), Is. 8, 216 p.
13. R.B. Dingle, Scattering of Electrons and Holes by Charged Donors and Acceptors in Semiconductors, *Phil. Mag., Ser. 7*, **46** (379), 831 – 840 (1955).
14. A.G. Samoilovich, V.D. Iskra, Effect of Crystal Anisotropy on Thermal Fluctuations of Atoms in *Ge* and *Si, Physics of the Solid State* **2** (11), 2827 – 2833 (1960).

Submitted 22.10.2012.

L.P. Bulat,[1] D. Kossakovski[2], D.A. Pshenai-Severin[3]

[1]National Research University ITMO, 9, Lomonosova Str., St. Petersburg 191002, Russia;
[2]ZT Plus, 1321 Mountain View Circle, Azusa, CA 91702, USA;
[3]Physicotechnical Institute RAS, 26, Politekhnicheskaya Str., St. Petersburg, 194021, Russia

THE INFLUENCE OF PHONON THERMAL CONDUCTIVITY ON THERMOELECTRIC FIGURE OF MERIT OF BULK NANOSTRUCTURED MATERIALS WITH TUNNELING CONTACTS

A composite material is considered which consists of conducting nanoparticles separated by tunneling dielectric barriers. The influence of the phonon thermal conductivity of dielectric matrix κ_d *on the thermoelectric figure of merit of this composite material is theoretically investigated. The range of* κ_d *values and barrier parameters that can lead to the thermoelectric figure of merit greater than unity is estimated. The influence of space charge and nonlinearity of current-voltage relations of tunneling barrier are also discussed.*

Key words: thermoelectrics, bulk nanostructures, electron tunneling, thermoelectric figure of merit.

Introduction

Thermoelectric materials are used in heat to electricity converters and refrigerators. Their main advantages are the lack of moving parts and environmentally unsafe refrigerants, maintenance-free operation and usage in waste heat utilization [1, 2]. The efficiency of energy conversion is determined by the thermoelectric figure of merit Z

$$ZT = \frac{S^2 \sigma}{\kappa}, \tag{1}$$

where T is the absolute temperature, S is the Seebeck coefficient, σ and κ are electrical and thermal conductivities of the material. One of the possibilities to enhance ZT above unity proposed recently is to use bulk nanostructured materials [3-10]. These materials are synthesized by means of ball milling of initial *BiTe-SbTe* solid solution material and subsequent hot-pressing [3-8]. The final samples were polycrystalline with grains of the size of about $20 - 30\,\text{nm}^3$ [3]. The other authors obtained solid solutions based on *PbTe-SbTe* with nano-inclusions of *Ag* or *Pb* [9, 10]. One can imagine that during the preparation process the nanograins can be coated with a dielectric material. So the composite will consist of conducting grains separated by a dielectric matrix. This type of nanostructured material is considered in the present paper.

The conduction in such structures is determined by electron tunneling through the dielectric barriers. This mechanism is similar to that in thermionic energy converters that were considered for the cases of layered geometry [11-13] and for the case of vacuum barrier between conical tip and semiconducting plate [14]. In the previous work [15] the influence of three-dimensional geometry of the grains on the thermoelectric efficiency of such nanocomposite was considered for the case of vacuum barriers. The grain geometry was modeled by two truncated cones with the same base (Fig. 1).

It was shown that in the case of vacuum barriers the thermoelectric efficiency of composite material can reach the values $ZT = 3.0 - 4.0$ at room temperature [15]. In the present work the results of the previous consideration [15] are extended to take into account the lattice thermal conductivity of intergrain dielectric media κ_d. The range of κ_d values and parameters of tunneling barrier that gave $ZT > 1$ were examined. In addition the influence of the space charge inside the barrier and possibility of nonlinearity of current-voltage dependence of tunneling junction are discussed.

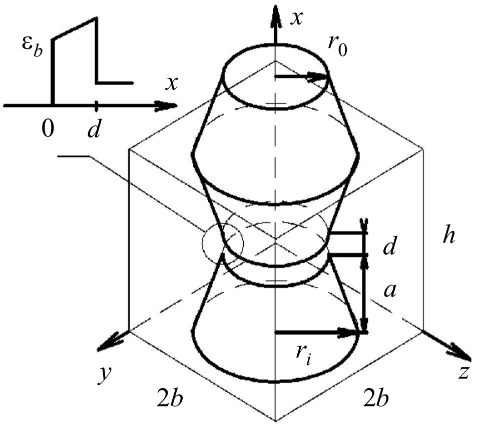

Fig. 1. Schematic drawing of the nanoparticle modeled as two truncated cones. 2a – nanoparticle length, r_0 – the radius of truncated part, r_l – the radius of base of the cone, h and 2b – height and width of elementary cell, d – width of tunneling barrier. In the inset the tunneling barrier of height ε_b under applied voltage difference is schematically drawn.

Calculation of electric and heat currents in tunneling junction

In the calculation it was assumed that the tunneling current flows only through the cylindrical part with the height d and base radius r_0 and the energy height of barrier is ε_b. The total energy ε of electron is conserved during the trip across the gap. Due to the conservation of the component of the momentum parallel to the electrode surface $k_{\|}$ the component of the energy corresponding to the movement perpendicular to that surface ε_x is conserved as well. This value is a sum of kinetic energy and potential energy inside the barrier

$$\varepsilon_x = \frac{\hbar^2 k_x^2(x)}{2m} + U(x). \tag{2}$$

The energy is considered to be zero at the bottom of the conduction band of the first electrode. The number of electrons with a given energy ε_x inside the interval $\mathrm{d}k_x$ can be calculated as

$$\frac{\mathrm{d}N(x)}{\mathrm{d}k_x} = \frac{2}{V}\sum_{k_{\|}} f_0(\varepsilon_{\|} + \varepsilon_x - \mu) = \frac{m k_0 T}{2\pi^2 \hbar^2} \ln\left(1 + e^{-(\varepsilon_x^* - \mu^*)}\right). \tag{3}$$

Here, μ is the chemical potential, m is the electron effective mass, f_0 is the Fermi-Dirac distribution function and all variables with asterisks are measured in k_0T units. The same quantity per unit interval of energy is

$$\frac{\mathrm{d}N_x(x)}{\mathrm{d}\varepsilon_x^*} = \frac{(m k_0 T)^{3/2}}{2^{3/2} \pi^2 \hbar^3 \sqrt{\varepsilon_x^* - U^*(x)}} \ln\left(1 + e^{-(\varepsilon_x^* - \mu^*)}\right). \tag{4}$$

The contribution of the electrons in the energy interval (ε_x, $\varepsilon_x + \mathrm{d}\varepsilon$) to the current density flow equals to

$$\mathrm{d}j_x = -e\,v_x\,\mathrm{d}\,N_x(x) = -e\,\frac{m\left(k_0\,T\right)^2}{2\,\pi^2\,\hbar^3}\ln\left(1+e^{-\left(\varepsilon_x^*-\mu^*\right)}\right)\mathrm{d}\varepsilon_x^*. \tag{5}$$

The current flow in the vertical direction (x-axis) inside the tunneling gap is given by the following equation

$$j_x = -e\,\frac{m\left(k_0\,T_1\right)^2}{2\,\pi^2\,\hbar^3}\int_0^\infty D(\varepsilon_x^*)\,\nu(\varepsilon_x^*,\mu_1^*)\left(1-\frac{T_2}{T_1}\frac{\nu(\varepsilon_x^*,\mu_2^*)}{\nu(\varepsilon_x^*,\mu_1^*)}\right)\mathrm{d}\varepsilon_x^*, \tag{6}$$

where indices $i = 1, 2$ denote two electrodes, $D(\varepsilon_x^*)$ is the electron tunneling probability and

$$\nu(x,y) = \ln\left(1+e^{-(x-y)}\right). \tag{7}$$

The equation for the heat flow is similar to (6)

$$q_x = \frac{m\left(k_0\,T_1\right)^3}{2\,\pi^2\,\hbar^3}\int_0^\infty D(\varepsilon_x^*)\,\theta(\varepsilon_x^*,\mu_1^*)\left(1-\left(\frac{T_2}{T_1}\right)^2\frac{\theta(\varepsilon_x^*,\mu_2^*)}{\theta(\varepsilon_x^*,\mu_1^*)}\right)\mathrm{d}\varepsilon_x^*, \tag{8}$$

where

$$\theta(x,y) = \frac{1}{6}\left(\frac{\pi^2}{2}+3(x-y)^2+6\,x\ln\left(1+e^{y-x}\right)\right)+\mathrm{Li}_2\left(-e^{x-y}\right), \tag{9}$$

and $\mathrm{Li}_2(x)$ is a dilogarithm.

In an external electric field the initial square barrier changes to a triangular. For the calculation of current and heat flow we use tunneling probability in WKB approximation for a triangular barrier [16]:

$$D_{tri}(\varepsilon_x) = \begin{cases} \exp\left(-\dfrac{4}{3}\sqrt{\dfrac{2m}{\hbar^2}}\dfrac{\left(\varepsilon_b-\varepsilon_x\right)^{3/2}-\left(\varepsilon_b-F\,d-\varepsilon_x\right)^{3/2}}{F}\right), & \varepsilon_x < \varepsilon_b - F\,d \\ \exp\left(-\dfrac{4}{3}\sqrt{\dfrac{2m}{\hbar^2}}\dfrac{\left(\varepsilon_b-\varepsilon_x\right)^{3/2}}{F}\right), & \varepsilon_b - F\,d < \varepsilon_x < \varepsilon_b \\ 1, & \varepsilon_x > \varepsilon_b \end{cases} \tag{10}$$

In this equation $F = -eE$ is the force acting on the electron in electrical field E.

When temperature difference is smaller than the average temperature $|\Delta T| = |T_2 - T_1| << \overline{T}$ and the potential drop on the single barrier $\mu_2 - \mu_1 = -e\Delta V$ is small $|e\Delta V| << k_0\,\overline{T}$, ε_b linear transport coefficients can be obtained neglecting the change of the barrier shape. For example, electric current density can be written as [20, 21]

$$j_x = \int_{v_x>0}\frac{2\,d^3\mathbf{k}}{(2\,\pi)^3}\left\{-e\,v_x(\mathbf{k})\,D(\mathbf{k})\left(-\frac{\partial f_0(\varepsilon^*-\mu_1^*)}{\partial\varepsilon^*}\right)\left(\frac{e\Delta V}{k_0\,T_1}-(\varepsilon^*-\mu_1^*)\frac{\Delta T}{T_1}\right)\right\}. \tag{11}$$

The equation for heat current density q_x can be obtained from (11) replacing $-ev_x(\mathbf{k})$ with

$(\varepsilon - \mu_1)v_x(\mathbf{k})$. It is useful to introduce an integral

$$J_n = \int\limits_{v_x>0} \frac{2d^3\mathbf{k}}{(2\pi)^3} \left\{ (\varepsilon^* - \mu_1^*)^n \; v_x(\mathbf{k}) \; D(\mathbf{k}) \left(-\frac{\partial f_0(\varepsilon^* - \mu_1^*)}{\partial \varepsilon^*} \right) \right\}. \tag{12}$$

Then expressions for tunneling electrical conductivity σ_t, thermopower S_t and thermal conductivity at zero voltage drop $\kappa_{t,\Delta V=0}$ can be written as

$$\sigma_t = (e^2 / k_0 T_1) J_0 , \; S_t = (e / T_1) J_1 / \sigma_t , \; \kappa_{t,\Delta V=0} = k_0 J_2 . \tag{13}$$

Usual thermal conductivity at zero electric current can be expressed as $\kappa_t = \kappa_{t,\Delta V=0} - S_t^2\sigma_t T_1$ [18].

For the case considered here, when tunneling probability depends only on ε_x and effective masses in electrodes and barrier are the same, integration in (12) – (13) can be partially performed analytically. These equations were obtained in the previous work [15] and are given in the appendix.

Note that the units of barrier kinetic coefficients σ_t and κ_t are different from that of a bulk sample as they connect flow density with potential and temperature difference and not with potential and temperature gradients. For comparison with the bulk values it is convenient to use values of $\sigma_t d$ and $\kappa_t d$.

The dependence of current density on voltage drop is shown in Fig. 2. In the calculations the effective mass was assumed to be equal to that of free electron m_0. The figure shows that there is a wide range of voltages for which the junction operates in a linear region. Usually, the practical current densities start from 1 A/cm^2. In Fig. 2 it can be seen that such currents are attainable for the barrier height of several tenths of eV and barrier thickness of several nanometers even in a linear regime of operation. Though the smallest available work function up to date [19-21] is about 0.8 eV, in heterostructures the barrier height ε_b is determined by the difference in the energy positions of conduction (valence) band in the material of grains and matrix which can be smaller (of the order of 0.1 eV). So, the values $\varepsilon_b \sim 0.1$ eV look quite reasonable.

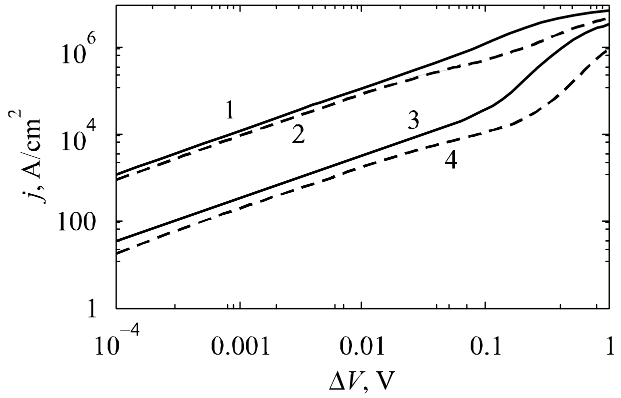

Fig. 2. Current-voltage dependences of tunneling contact. ε_b = 0.1 eV (1, 2), 0.2 eV (3, 4); d = 2 nm (1, 3), 5 nm (2, 4).

In Fig. 3 the plot of the Peltier coefficient $\Pi_t = q/j$ is presented. It can be seen that the values of the Peltier coefficient are greater than conventional values for room temperature thermoelectrics based on Bi_2Te_3-Sb_2Te_3 solid solutions. The values of the Peltier coefficient increase when the relative contribution of more energetic carriers to the heat flow increases. The energy filtering of carriers in a linear region of operation is determined by the exponential dependence of tunneling probability on carrier energy. So, the contribution to the heat flow from carriers with energies lower than ε_b is small.

At larger voltages the shape of barrier changes from square to triangular. Generally, this can lead to stronger energy filtering and increase in the Peltier coefficient. But this effect can be seen only for large ε_b (see 5 in Fig. 3). For smaller ε_b this effect is less important and the increase of tunneling probability for all electrons with energies lower than ε_b leads to decrease in Peltier coefficient (see curves 1 – 4 in Fig. 3).

In a bulk composite material with grains of 20 – 30 nm in size the voltage drop and temperature difference are small, as was discussed in the previous work [15]. For example, if the size of the sample is 1mm, and the grain size is 20 nm, then ΔT is $5\cdot10^4$ times smaller than total temperature difference of the order of 100 K, so $\Delta T \sim 2\cdot10^{-3}$ K $<< \bar{T}$. This can lead to the total voltage difference due to the Seebeck effect of the order of 0.1 V for large $S = 10^3$ μV/K and $\Delta V \sim 2$μV. So, even for the several orders of magnitude increase in total voltage difference the single junction will operate in a linear regime. As can be seen from Figs. 2 and 3, a linear region of operation can be attractive for getting large Peltier coefficients and reasonable current densities. Therefore, only this region will be considered.

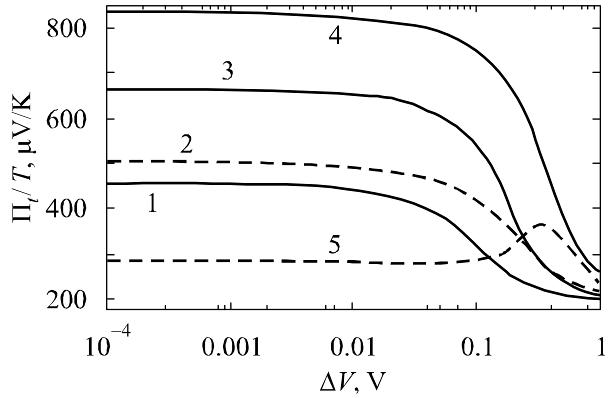

Fig. 3. Dependences of the Peltier coefficient of tunneling contact on voltage.
(1 – 4 – see Fig. 2; 5 – ε_b = 0.5 eV, d = 2 nm).

The dependences of the electrical conductivity and thermopower on the barrier thickness in a linear operation region are plotted in Fig. 4, as calculated using equations from the previous work [15]. It can be seen that for small *d* the electrical conductivity decreases with the increase of *d* due to decrease of the tunneling probability and then it slowly increases as it is proportional to barrier thickness for ballistic transport. The thermopower, on the contrary, increases with *d* due to better energy filtering of heat carriers.

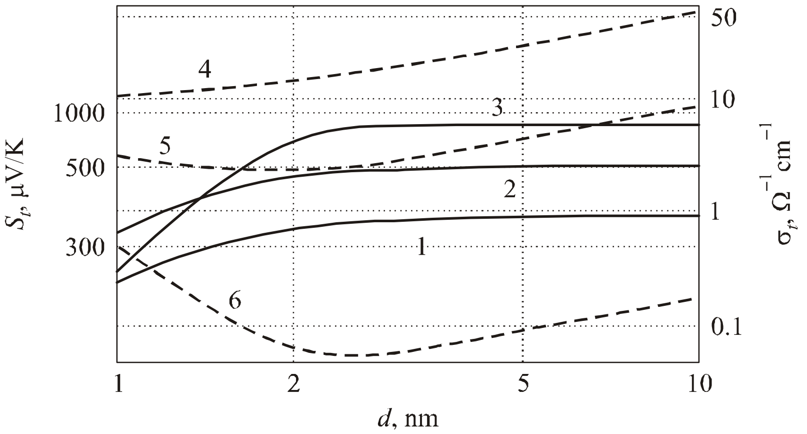

Fig. 4. Dependences of the Seebeck coefficient (1 – 3) and electrical conductivity (4 – 6)
on barrier thickness. ε_b = 0.05 eV (1, 4); 0.1 eV (2, 5); 0.2 eV (3, 6).

The potential barrier can be changed not only due to external electric field but also due to charge buildup and image charge effects. The latter effect decreases the energy height of the potential barrier that leads to increase in current density. However, the former effect leads to the increase of the barrier height. The influence of both effects is less pronounced in dielectric media with permittivity $\varepsilon_d > 1$. In order not to complicate the treatment they are not included in consideration. We just estimate the possible influence of the charge buildup effect as the one that worsens the situation and show that for small d this effect is negligible. The effect is connected with the electrons which have enough energy to penetrate into barrier region and create negative charge that prevents other electrons from getting there. This leads to effective increase of the barrier height and decrease of the current density. This effect was taken it into account in [11, 22] for the case of thermionic emission and classical statistics. The simple equation for barrier form in equilibrium given in [11] reads

$$U(x) = \varepsilon_b + 2k_0 T \ln\left[\cos\left((x - d/2)c/2x_l\right)/c\right], \tag{14}$$

where $x_l^2 = \left(\varepsilon_d \sqrt{\pi}\,\hbar^3 / 4e^2 \sqrt{2k_0 T}\, m^{3/2}\right) e^{\varepsilon_b^* - \mu^*}$ and constant c can be determined from equation $\cos(dc/4x_l) = c$ for $0 < c < 2\pi x_l/d$. This effect is most important for small ε_b. But it appears that for small barrier thickness the change of the barrier height is less than several percent. For example for $\varepsilon_b = 0.1$ eV and $d = 2, 5, 10$ nm the increase in barrier height is 0.23, 1.4 and 5 percent, respectively. In these estimations ε_d is taken to be unity. In dielectric media $\varepsilon_d > 1$ so the barrier increase will be even less. So, for a linear operation region this effect can be disregarded.

Kinetic coefficients of a composite medium

A fruitful method for calculation of thermoelectric effective kinetic coefficients in two-phase structures was suggested in [23]; then the method was generalized and developed (see the review [24]). The method allows establishing an exact conformity (isomorphism) between calculation of effective kinetic coefficients for system with thermoelectric phenomena and effective electric conductivity in a medium without thermoelectricity. But if it is impossible to represent a system as consisting of two phases, the problem of determination of effective values becomes much more complicated, as the isomorphism method in this case cannot be used. An example of such situation is bulk nanocomposite [15]; the approach to calculation effective kinetic coefficients in this case is discussed in [25]. To calculate the effective coefficients for composite material, we will be limited to a model similar to the previous one [15].

The nanoparticle is modeled with the help of two truncated cones with the same base. The nanocomposite is formed from the primitive cells depicted in Fig. 1. The geometric parameters are the following: a is the height of each truncated cone, so $2a$ is the size of nanoparticles along the vertical direction. Radii r_0 and r_1 are the smaller and larger radii of the cone bases and 2θ is the cone aperture angle. The primary cell has a square base in horizontal plane with size $2b$. The height of the elementary cell is $h = 2a + d$. The analytical solution for effective kinetic coefficients was obtained previously but the lattice thermal conductivity of dielectric κ_d was not taken into account [15].

Due to the complexity of the geometry of the considered object and the fact that $\kappa_d \neq 0$ the variables cannot be separated and the analytical solution for kinetic coefficients was not found. In the present work the numerical solution of equations for heat and current flow was used for calculation of the effective kinetic coefficients. In the following treatment the index n for kinetic coefficient σ_n, S_n, κ_n corresponds to nanograin.

In our calculations the system of differential equations for the temperature and electrical potential distribution was solved numerically [26]

$$\begin{gathered}\operatorname{div}(-\sigma\alpha\nabla T)+\operatorname{div}(-\sigma\nabla\phi)=0,\\ \operatorname{div}(-(\sigma\alpha^2 T+\kappa)\nabla T)+\operatorname{div}(-\sigma\alpha T\nabla\phi)=\sigma((\nabla\phi)^2+\alpha\nabla T\nabla\phi),\end{gathered}\tag{15}$$

where ϕ is electrical potential.

To calculate the effective coefficients of the nanostructures material, one has to set the boundary conditions. The set of 5 elementary cells stacked in the vertical direction and connected to metallic contacts were considered and in the horizontal direction the structure was considered to be periodic. The comparison with the case of only one cell showed that the influence of contacts is negligible. The boundary conditions on outer boundaries are the following: on the left, right, front and back sides of the primary cell normal components of electrical and heat currents are set to zero $j_n = 0$, $q_n = 0$; on the top $T_1 = 300$ K, $\phi_1 = 0$; on the bottom side one can fix either temperature and potential T_0, ϕ_0 or inflowing heat and current fluxes $j_n = j_0$, $q_n = q_0$. Here, the second type of conditions was used because they provide better convergence during numerical calculations. The boundary conditions on the inner boundaries are the continuity of the normal components of current and heat fluxes determined and continuity of temperature and potential fields. These boundary conditions automatically include the Peltier effect at the contact of two dissimilar materials.

For each set of parameters two calculations were performed. In the first run the heat flow density was fixed q_0 and $j_0 = 0$. Then the temperature T_0 and potential ϕ_0 on the bottom contact were calculated. From this run the effective thermal conductivity and thermopower can be calculated $\kappa_{eff} = -q_0 / (T_1 - T_0)L$, $\alpha_{eff} = -(\phi_1 - \phi_0)/(T_1 - T_0)$. Here L is the size of the considered part of the sample along the vertical direction. Next we perform another calculation with $q_0 = 0$ and fixed j_0 and determine the electrical conductivity $\sigma_{eff} = -j_0 / (\phi_1 - \phi_0 + \alpha_{eff}(T_1 - T_0)L$.

In the calculations two possible material sets were considered. In the first one the grains were assumed to consist of typical thermoelectric semiconducting material with $\mu = 0$, $\sigma_n = 1000$ S/cm, $\alpha_n = 200$ μV/K, $\kappa_{n,ph} = 1$ W/m·K. These values are close to transport coefficients of $p\text{-}Bi_2Te_3$ in cleavage plane (normal to trigonal axis). In the second parameter set the nanograin was assumed to consist of metal (*Ag*) with $\mu = 5.49$ eV, $\sigma_n = 6.3\cdot10^5$ S/cm, $\alpha_n = 1.33$ μV/K, $\kappa_n = 430$ W/m·K. The effective coefficients were calculated for the following geometries: $2a = 10, 20, 30$ nm, $d = 1, 2, 5$ nm, $\varepsilon_b - \mu = 0.05, 0.1, 0.2$ eV, $b = 1.1\,a$, $\theta = 15°, 30°$. Note that for metal nanoparticles ε_b is counted from the chemical potential level.

Typical dependencies of effective thermoelectric figure of merit on dielectric thermal conductivity are presented in Fig. 5 for $\theta = 15°$ and $2a = 20$ nm. The dashed curves correspond to metallic grains and solid curves correspond to semiconducting ones. From Fig. 5 it can be seen that the thermoelectric efficiency can be greater than unity if thermal conductivity of dielectric $\kappa_d < 0.01 \div 0.02$ W/m·K at $\varepsilon_b = 0.1$ eV and for $\kappa_d < 0.05$ W/m K at barrier height of 0.05 eV. The increase in electrical conductivity is preferable for increase of $Z_{eff}T$. Hence $Z_{eff}T$ is greater for smaller ε_b. It is interesting that for sufficiently small ε_b the electrical conductivity ($\sigma_t d$) increases with the increase of barrier thickness as it should be for ballistic transport. This leads to larger $Z_{eff}T$ values for larger d (compare curves 1 and 2 in Fig. 5). Further increase of $Z_{eff}T$ with d is limited by the number of factors, e.g. due to increase of space charge effect or transition from ballistic to diffusive transport in barriers where the approach developed in this paper is inapplicable.

The comparison of $Z_{eff}T$ for semiconducting and metallic grains shows their similarity. As the main contribution to the thermal conductivity is due to tunneling barrier, the effective Seebeck coefficient is not very sensitive to the value of S_n. But the thermal conductivity of nanograin should be increased so that the temperature difference on the tunneling junction is increased as well. This leads to larger $Z_{eff}T$ values for metallic nanoinclusions (compare solid and dashed curves in Fig. 5).

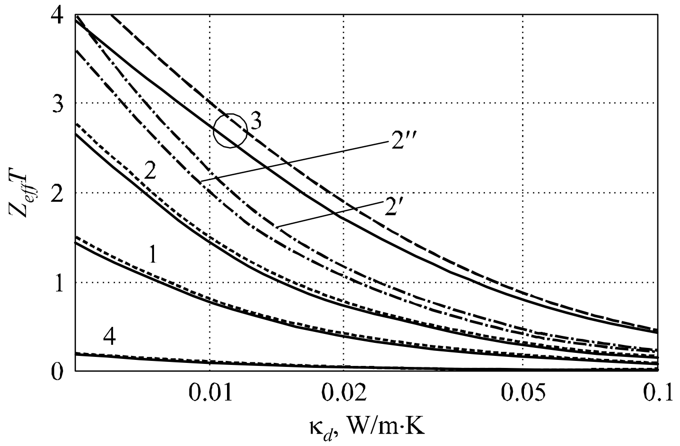

Fig. 5. Dependences of the thermoelectric figure of merit on dielectric thermal conductivity for different material parameters. Solid and dashed curves are plotted for semiconducting and metallic nanoparticles correspondingly assuming the same effective mass in nanoparticle and barrier. Dash-dotted curves are plotted taking into account the influence of anisotropy of semiconducting material (see text for details). Barrier parameters d and ε_b are the following: 1 – 2 nm, 0.1 eV; 2, 2', 2'' – 5 nm, 0.1 eV; 3 – 5 nm, 0.05 eV; 4 – 5 nm, 0.2 eV.

It is interesting also to estimate the influence of the anisotropy of semiconducting material on the obtained results. The anisotropy can enter the calculations in two ways: due to anisotropy of band structure and the anisotropy of transport coefficients. Bi_2Te_3 is a layered material of rhombohedral symmetry. Usually trigonal axis normal to cleavage planes is denoted as crystallographic direction 3. If axis 1 lies in the plane and directed along one of binary axes, then the remaining 2nd direction lies in one of mirror planes. The anisotropy of transport coefficients for holes in Bi_2Te_3 is $\sigma_{11} / \sigma_{33} = 2.7$ and $\kappa_{ph,11} / \kappa_{ph,33} = 3$, while thermopower is isotropic [27]. The band structure of Bi_2Te_3 can be described by 6-ellipsoidal Drabble-Wolfe model [28]. The effective masses of holes $m_1 = 0.73\, m_0$, $m_2 = 0.064\, m_0$, $m_3 = 0.196\, m_0$ and tilt angle $\theta = 39.6°$ are given in [29]. The probability of tunneling through the square potential barrier for the case of anisotropic energy spectrum is given in [30]. Let's assume that the anisotropic energy spectrum for one ellipsoid can be written as $\varepsilon^{(n)} = (\hbar^2 / 2m_0)\mathbf{k}^{(n)}\cdot\alpha^{(n)}\cdot\mathbf{k}^{(n)}$, where $\alpha^{(n)}$ is inverse effective mass tensor in crystal axes and indices $n = 1, 2$ are for semiconductor and barrier, respectively. Components of the wave vector parallel to interface $k_{2(3)}$ and total energy ε conserve during tunneling. Tunneling probability can be written as [30]

$$D(\mathbf{k}) = \begin{cases} \left(1 + \dfrac{(\xi_1^2\,\alpha_{11}^{(1)} / \alpha_{11}^{(2)} + \xi_2^2\,\alpha_{11}^{(2)} / \alpha_{11}^{(1)})^2}{4\xi_1^2\,\xi_2^2}\mathrm{sh}^2(\xi_2\, d)\right)^{-1}, & \xi_2^2 > 0 \\ \left(1 + \dfrac{(\xi_1^2\,\alpha_{11}^{(1)} / \alpha_{11}^{(2)} - \left|\xi_2^2\right|\alpha_{11}^{(2)} / \alpha_{11}^{(1)})^2}{4\xi_1^2\left|\xi_2^2\right|}\sin^2(\left|\xi_2\right| d)\right)^{-1}, & \xi_2^2 < 0 \end{cases} \tag{16}$$

Here the following notation was used $\xi_1^2 = \left(2m_0 / \hbar^2\,\alpha_{11}^{(1)}\right)\varepsilon_x^{(1)}$, $\xi_2^2 = \left(2m_0 / \hbar^2\,\alpha_{11}^{(2)}\right)\left(\varepsilon_b - \varepsilon_x^{(2)}\right)$ and $\varepsilon_x^{(n)} = \varepsilon - \left(\hbar^2 / 2m_0\right)\sum_{i,j=2,3}\left(\alpha_{i,j}^{(n)} - \alpha_{i,1}^{(n)}\,\alpha_{1,j}^{(n)} / \alpha_{11}^{(n)}\right)k_i\,k_j$.

The difficulty in calculations of tunneling transport coefficients for this case comes from the fact that tunneling probability $D(\mathbf{k})$ depends not only on energy ε_x in the direction of tunneling but on all components of wave vector **k** and the expressions for transport coefficients (12) – (13) involve triple integration. To estimate the influence of anisotropy, we calculated tunneling transport coefficients for three possible orientations when x axis of tunneling was directed along one of three crystallographic directions mentioned above. The effective mass in barrier was assumed to be m_0 for comparison with previous estimations. Tunneling transport coefficients for these cases are listed in Table 1.

Table 1

Tunneling transport coefficients for barrier parameters d = 5 nm and ε_b = 0.1 eV

	$S_{t,ii}$, μV/K	$\sigma_{t,ii}$, S/cm	$\kappa_{t,ii}$, W/m·K
Isotropic WKB approximation	504	4.47	0.002
$i = 1$	518	6.94	0.0029
$i = 2$	516	6.76	0.0028
$i = 3$	504	7.43	0.003

From the Table 1 it can be seen that the thermopower in all tree cases differs insufficiently from WKB approximation. When we took into account the influence of anisotropy of effective mass in the semiconductor and its difference from barrier effective mass, tunneling current from single ellipsoid became smaller than in the isotropic case. But for considered material when x axis is parallel to directions 1 or 2 there are two sets of 2 and 4 equivalent ellipsoids, while when x is parallel to trigonal axis all 6 ellipsoids are equivalent. As a result, total electrical and thermal conductivities appeared to be 1.5 – 1.7 times larger than in the isotropic WKB case. Tunneling transport coefficients are almost isotropic and for directions 1 and 2 are almost equal.

The influence of the anisotropy of transport coefficients of Bi_2Te_3 is illustrated in Fig. 5. Curves 2', 2" are plotted for directions 1 and 3 mentioned above taking into account anisotropy of both semiconductor and tunneling transport coefficients. These curves can be compared to curve 2 obtained in the isotropic WKB approximation. From the figure it can be seen that the anisotropy of semiconducting material did not change qualitatively the results of estimations. The main impact on the results of estimations comes from the change of tunneling probability, and the anisotropy of semiconductor transport coefficients is less important.

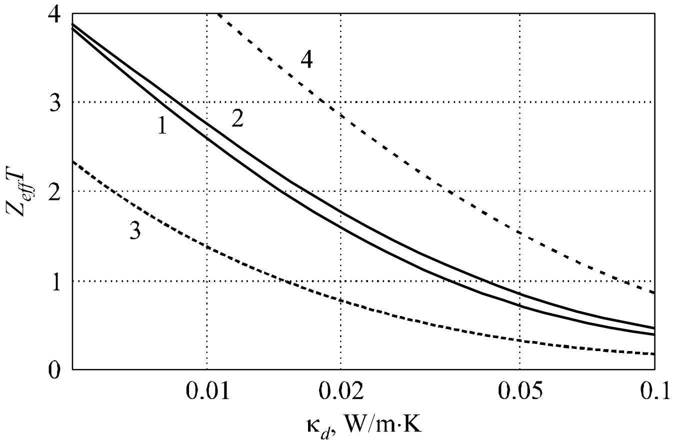

Fig. 6. Dependences of the thermoelectric figure of merit on dielectric thermal conductivity for semiconducting grains and different geometric parameters. Barrier parameters ε_b = 0.05 eV, d = 5 nm. 1 and 2 – θ = 15°, 2a = 30 nm and 10 nm; 3 – θ = 30°, 2a = 10 nm; 4 – layered geometry 2a = 10 nm.

In Fig. 6 the dependence of effective thermoelectric figure of merit on the geometric parameters is illustrated. For getting larger $Z_{eff}T$ values the smaller grain size is preferable to increase the barrier contribution to Seebeck coefficient (compare 1 and 2 on fig. 6). In Fig. 6 curve 4 is plotted for layered geometry and it can be seen that in this case larger $Z_{eff}T$ values can be obtained for the same κ_d. This is because in the layered geometry the area of tunneling contact increases which leads to the increase of effective electrical conductivity. The decrease of the thermoelectric figure of merit for the larger θ with the other parameters unchanged is due to the same reason (curve 3 in Fig. 6).

Conclusions

In the present work effective transport coefficients and thermoelectric figure of merit were calculated for nanostructured composite material that consists of conductive grains separated by a dielectric matrix. The tunneling current and heat flow through the dielectric barrier was calculated for the linear and nonlinear regions of operation. It was shown that the current density can be larger than 1 A/cm^2 even in the linear operating region if barrier height ε_b is less than about 0.2 eV and barrier width d is less than about 5 nm. Estimations showed that at such small barrier widths the increase of the barrier height due to the free electron space charge inside the barrier is negligible.

A range of the lattice thermal conductivity of dielectric that can lead to $Z_{eff}T > 1$ was estimated. This range depends on the parameters of tunneling barriers and grain size, e.g. for barriers with the thickness of 5 nm and height 0.05 – 0.1 eV κ_d values should be less than 0.02 – 0.05 W/m K. This result was compared to the layered geometry and it was shown that for the same barrier parameters the upper limit for κ_d is expanded to 0.1 W/m K. Thus there are three types of requirements that should be satisfied in order to get $Z_{eff}T > 1$. The first one is the barrier thickness less than 5 nm – this can be readily satisfied with current level of material technology. The second requirement is low thermal conductivity of the barrier (less than 0.05 – 0.1 W/m K). The third one is the barrier height less than 0.1 eV.

The second and third conditions can at the first glance seem to be incompatible. To resolve this contradiction, one of the possibilities is to use porous materials with a low thermal conductivity. For example, in sintered aerogel films (porous SiO_2) the thermal conductivity can be well below 0.1 W/m K [31]. But in the case of porous material the tunneling barrier height is determined by the work function that could hardly be less than 0.8 eV [19-21]. In this case, if the pores are filled with a gas, then even tiny thermal conductivity of gaseous phase would completely cancel the effect of thermoelectric efficiency increase due to tunneling through the barrier structure. The contradiction of the second and the third requirement for this case can be resolved only with vacuum barriers. The vacuum is a unique dielectric material that can satisfy all requirements. So, one of the possibilities is that corresponding thermoelectric material with good efficiency could be a porous nanostructure based on bismuth telluride with vacuum pores.

The second possibility that has emerged recently is to use dense materials with ultralow thermal conductivity [32]. Usually the low limit of thermal conductivity is connected with disordered materials [33] where the mean free path for phonons is about interatomic distances. But in the multilayered WSe_2 material the thermal conductivity as low as 0.05 W/m K was observed [32]. It is interesting that in this material low thermal conductivity is connected with the phonon scattering on the precisely ordered Se-W-Se layers connected with weak van der Waals forces. Taking into account that bismuth telluride also consists of layers connected by van der Waals forces, it possible to imagine the preparation of at least layered structure from thin barrier WSe_2 layers with low thermal conductivity and layers of bismuth telluride as a good thermoelectric material. For the bulk material electron affinity and band gap of WSe_2 are about 4 eV and 1.2 eV, respectively [34]. For Bi_2Te_3 the electron affinity is similar about 4.125 – 4.525 eV [35]. This suggests that if the proper doping levels are achievable, then one can obtain the work function difference and corresponding barrier height about 0.1 – 0.05 eV. To confirm this possibility, further investigation of the band diagram and transport properties of this type of structure are required.

Acknowledgement. The work was supported by the ZT Plus-Amerigon.

Appendix

The expressions for tunneling transport coefficients obtained in [15] can be written as follows:

$$\sigma_t = \frac{e^2\, m\, k_0\, T}{2\pi^2\, \hbar^3} \int_0^{\infty} D(\varepsilon_x^*)\, f_0(\xi)\, \mathrm{d}\varepsilon_x^*, \tag{17}$$

$$|\beta_t| = \frac{e\, m\, k_0^2\, T}{2\pi^2\, \hbar^3} \int_0^{\infty} D(\varepsilon_x^*)\left(\xi f_0(\xi) + \ln\left(1 + e^{-\xi}\right)\right)\mathrm{d}\varepsilon_x^*, \tag{18}$$

$$\kappa_{t,\Delta V=0} = \frac{m\, k_0^3\, T_1^2}{2\pi^2\, \hbar^3} \int_0^{\infty} D(\varepsilon_x^*)\left(\xi^2 f_0(\xi) + 2\xi F_0(-\xi) + 2F_1(-\xi)\right)\mathrm{d}\varepsilon_x^*. \tag{19}$$

In these expressions ξ is defined as $\xi = \varepsilon_x^* - \mu_1^*$. The Fermi integrals are defined as $F_n(y) = \int_0^{\infty} f_0(x - y)\, x^n\, \mathrm{d}x$. It can be shown that $F_n(y) = -\Gamma(n+1)\,\mathrm{Li}_{n+1}(-e^y)$, where $\Gamma(n+1)$ and $\mathrm{Li}(x)$ are gamma-function and poly-logarithm. Using this relation the expression for $\kappa_{t,\,\Delta V=0}$ was rewritten in a more compact form compared to [15].

References

1. A.J. Minnich, M.S. Dresselhaus, Z.F. Ren, and G. Chen, *Energy Environ. Sci.* **2**, 466 (2009).
2. A.V. Dmitriev, I.P. Zvyagin, *Physics-Uspekhi* **53**, 789 (2010).
3. B. Poudel, Q. Hao, Y. Ma, Y. Lan, A. Minnich, B. Yu, X. Yan, D. Wang, A. Muto, D. Vashaee, X. Chen, J. Liu, M.S. Dresselhaus, G. Chen, and Zh. Ren, *Science* **320**, 634 (2008).
4. Y. Lan, A.J. Minnich, G. Chen, and Zh. Ren, *Advanced Functional Materials* **20**, 357 (2010)
5. L.P. Bulat, V.B. Osvensky, G.I. Pivovarov, A.A. Snarskii, E.V. Tatyanin, and A.A.O. Tay, *Proc. 6th Europ. Conf. on Thermoelectrics* (Paris, France, 2008), I2-1 – I2-6 p.
6. L.P. Bulat, I.A. Drabkin, V.V. Karataev, V.B. Osvenskii, and D.A. Pshenai-Severin, *Physics of the Solid State* **52**(9), 1836 – 1841 (2010).
7. L.P. Bulat, V.T. Bublik, I.A. Drabkin, V.V. Karataev, V.B. Osvenskii, Yu.N. Parkhomenko, G.I. Pivovarov, D.A. Pshenai-Severin, and N.Yu. Tabachkova, *J. Electronic Materials* **39**(9), 1650-1653 (2010).
8. L.P. Bulat, D.A. Pshenai-Severin, I.A. Drabkin, V.V. Karatayev, V.B. Osvensky, Yu.N. Parkhomenko, V.D. Blank, G.I. Pivovarov, V.T. Bublik, N.Yu. Tabachkova, *J. Thermoelectricity*, **1**, 13 – 18 (2011).
9. K.F. Hsu, S. Loo, F. Guo, W. Chen, J.S. Dyck, C. Uher, T. Hogan, E.K. Polychroniadis and G. Kanatzidis, *Science* **303**, 818(2004).
10. J.P. Heremans, C.M. Thrush, and D.T. Morelli, *J. Appl. Phys.* **98**, 063703 (2005).
11. G.D. Mahan, *J. Appl. Phys.* **76**, 4362 (1994).
12. G.D. Mahan, L.M. Woods, *Phys. Rev. Lett.* **80**, 4016 (1998).

13. Y. Hishinuma, T.H. Geballe, B.Y. Moyzhes, and T.W. Kenny, *Appl. Phys. Lett.* **78**, 2572 (2001).
14. U. Ghoshal, *Proceedings of the XXI International Conference on Thermoelectrics* (N.Y., USA, 2002), 540 p.
15. L.P. Bulat, D.A. Pshenai-Severin, *Physics of the Solid State* **52**, 485 (2010).
16. L.D. Landau and E.M. Lifshitz, *Quantum Mechanics Non-Relativistic Theory* (Course of Theoretical Physics, Volume 3, 3rd edition) (Elsevier, 2003), 692 p.
17. E. Burstein, S. Lundqvist (ed.) *Tunneling Phenomena in Solids* (N.Y., Plenum Press, 1969), 422 p.
18. M. Bartkowiak, G.D. Mahan, *Proc. Symp. Mat. Res*. Soc. **545**, 265 (1999).
19. A.H. Sommer. *Photoemissive Materials* (Krieger, New York, 1980), 256 p.
20. S.A. Lindgren, L. Wallden, *Phys. Rev.* ***B*** **22**, 5967 (1980).
21. G.G. Magera, P.R. Davis, *J. Vac. Sci. Technol.* ***A*** **11**, 2336 (1993).
22. J.B. Scott, *J. Appl. Phys*. **52**, 4406 (1981)
23. J.P. Straley, *J. Phys.* ***D*** **14**, 2101 (1981).
24. A.A. Snarskii, I.V. Bezsudnov, *J. Thermoelectricity* **3**, 7 – 23, (2005).
25. A.A. Snarskii, A.K. Sarychev, I.V. Bezsudnov, and A.N. Lagarkov, *Semiconductors* **46**, 659 (2012)
26. M. Jaegle, "Multiphysics Simulation of Thermoelectric Systems - Modeling of Peltier-Cooling and Thermoelectric Generation" in *Proceedings of the COMSOL Conference 2008 Hannover,* http://www.comsol.com/papers/5256
27. B.M. Goltsman, V.A. Kudinov, and I.A. Smirnov, *Thermoelectric Semiconductor Materials Based on* Bi_2Te_3 (Nauka, Moscow, 1972; Army Foreign Science and Technology Center, Charlottesville, Virginia, United States, 1973)
28. J.R. Drabble and R. Wolfe, *Proc. Phys. Soc., London, Sect. B* **69**, 1101 (1956).
29. M. Stordeur, M. Stoelzer, H. Sobotta, and V. Riede, *Phys. Status Solidi B* **150**, 165 (1988).
30. K.-Y. Kim, B. Lee, *Phys. Rev.* ***B*** **58**, 6728 (1998)
31. A. Jain, S. Rogojevic, Sh. Ponoth, W.N. Gill, J.L. Plawsky, E. Simonyi, Sh.-T. Chen, and P.S. Ho, *J. Appl. Phys*. **91**, 3275 (2002).
32. C. Chiritescu, D.G. Cahill, N. Nguyen, D. Johnson, A. Bodapati, P. Keblinski, and P. Zschack, *Science* **315**, 351 (2007).
33. D.G. Cahill, S.K. Watson, and R.O. Pohl, *Phys. Rev.* ***B*** **46**, 6131 (1992).
34. O. Lang, Y. Tomm, R. Schlaf, C. Pettenkofer and W. Jaegermann, *J. Appl. Phys*. **75**, 7814 (1994).
35. J. Nagao, E. Hatta, K. Mukasa, *Proceedings of the XV International Conference on Thermoelectrics* (Pasadena, CA, USA, 1996), 404 p.

Submitted 15.01.2013.

D.M. Freik[1], C.A. Kryskov[2], I.V. Horichok[1], T.S. Lyuba[1],
O.S. Krynytsky[1], O.M. Rachkovsky[2]

[1]Institute of Physics and Chemistry, Vasyl Stefanyk Precarpathian National University,
57, Shevchenko Str., Ivano-Frankivsk, 76018, Ukraine;
[2]Physics Department, Kamyanets-Podilsky State University, 61, Ogienko Str,
Kamyanets-Podilsky, 32300, Ukraine

SYNTHESIS, PROPERTIES AND MECHANISMS OF DOPING WITH *Sb* OF THERMOELECTRIC LEAD TELLURIDE *PbTe*:*Sb*

The effect of Sb doped lead telluride n-PbTe:Sb fabrication factors on the electric conductivity and the Seebeck coefficient values was studied. It was established that optimal properties are inherent in the samples with impurity content 0.3 at% Sb the thermoelectric power of which reaches a maximum at a temperature of T = 500 K and makes $\alpha^2\sigma \approx 70$ *μW/(K²cm). The crystal-chemical doping mechanisms and the dominant point defects of investigated crystals were determined.*

Key words: lead telluride, doping mechanisms, thermoelectric properties.

Introduction

Lead telluride is a promising thermoelectric material for medium-temperature (500 – 700) K thermal energy converters [1-3]. The properties of *PbTe* can be improved by chemical composition modification, in particular, by doping and optimization of technological processes of compound synthesis and preparation of thermoelectric pellets.

Considerable interest has been shown recently in the investigation of properties of lead chalcogenides doped with V group elements of the periodic table [4]. According to [5], *Sb* and *Bi* impurities in *PbTe* are donors and the share of electrically active atoms is appreciably less than the number of introduced ones. It is explained either by formation of electrically inactive complexes in the lattice of Sb_2Te_3 type compound, or the distribution of impurity between the cation (where it is a donor) and anion (where it is apparently an acceptor) sublattices [4, 6, 7]. In [4, 8] by means of the emission Mőssbauer spectroscopy technique on ^{119}Sb (^{119m}Sn) isotope it is shown that *Sb* impurity atoms in lead chalcogenide sublattices are distributed between the cation and anion sublattices, in which case in the electron samples the main share of *Sb* is localized in the anion sublattice, and in the hole samples – in the cation sublattice.

Thus, doping of lead telluride with *Sb* should result in the optimization of material thermoelectric parameters: increase in the electric conductivity of samples and reduction of their thermal conductivity. However, despite the already established general concepts of *PbTe*:*Sb* doping, the issue remains open as to the effect of samples preparation process on the mechanism of entering *Sb* impurity atoms into lead telluride crystal lattice and its influence on the thermoelectric figure of merit of material as a whole.

In this paper, the effect of *PbTe*:*Sb* samples fabrication and thermal treatment on their electrical characteristics is studied, and crystal-chemical models of crystal doping mechanisms are proposed.

Experimental procedure

Impurity-free and doped lead telluride was obtained by direct melting of prepurified components agitated during synthesis. To remove the impurities, metal lead was placed into cleaned and dried Pyrex or molybdenum ampoules which were evacuated to residual pressure 10^{-4} Pa, sealed and placed into a double-zone electric furnace. The temperature in heating zone was set 70 to100°K higher than lead melting point. The temperature maintained in substance-free ampoule area was 340 to 350 K. In this state the ampoule was maintained for 5-6 hours. During this time, impurities with melting point lower than that of lead were evaporated and due to the effect of temperature gradient they were transferred to free ampoule end, being deposited on its walls. Following that, the free ampoule end was removed from the furnace and the ampoule was inclined in such a way that liquid lead slowly spread over the walls and immediately solidified. As long as lead oxide has melting temperature about 1160 K, it remained on the ampoule walls at loading place, together with high-melting impurities.

Sublimation technique was employed to purify tellurium from impurities. The evacuated ampoule with tellurium was placed into a double-zone furnace inclined in such a way that evaporation area (hot zone) was 7 to 10 cm lower than condensation area (cold zone). The hot zone temperature was set as 770 °K and in condensation area – 690 K. The process duration was up to 120 hours.

Purified components *Pb*, *Te* and *Sb* doping impurity in the appropriate mass ratios were loaded into prepared ampoules of C5-1 quartz glass. The ampoules were evacuated to a residual pressure of 10^{-4} Pa and sealed. Then they were placed in a double-zone resistance electric furnace, and chromel-alumel thermocouples were arranged on the ampoule edges for temperature control. The temperature 800 K was set in the furnace, whereby all the components passed into a liquid phase. To increase compound homogeneity [9], the electric furnace performed 6 full-wave oscillations with a deviation from the horizontal position by the angles ± 30°. After that, the electric furnace was held for 50 hours for the diffusion processes. Then, at a temperature of 1240 K, the furnace again made 6 full-wave oscillations. Afterwards, the electric furnace was installed horizontally, and in this state the process of synthesis lasted for another 70 hours.

The electric furnace with a synthesized compound was cooled down to 700 K at a rate of 5 K/hour, and, subsequently, at a double rate to room temperature.

The obtained material was ground in agate mortar and, on separating fractions of size 0.05 – 0.5 mm, it was compacted under pressure 0.5 – 1 GPa, which yielded cylinder-shaped samples with $d = 5$ mm and $l \approx 5 - 10$ mm. Following that, the samples were again annealed in the air for 5 hours at a temperature of 500 K.

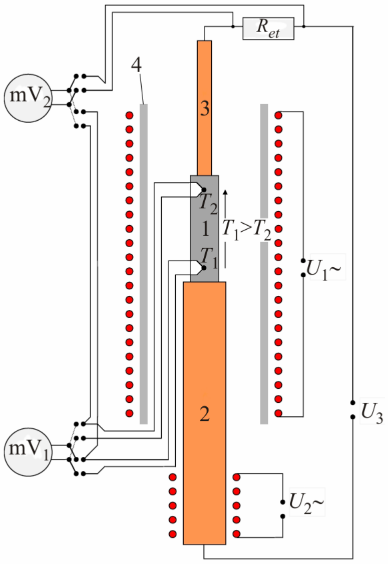

Fig. 1. Schematic of installation for measuring the Seebeck coefficient and electric conductivity: 1 – sample; 2, 3 – copper rods; 4 – quartz tube.

The thermoEMF (α) and electric conductivity (σ) values were determined by standard procedure on the installation schematically shown in Fig. 1. The sample was placed in a furnace between two copper rods one of which was heated to create temperature gradient (≈ 10 K) on the sample. The temperature was measured by two chromel-alumel thermocouples placed in the holes drilled in the sample. The electric conductivity was found by measuring a drop in the sample voltage generated by constant voltage source U_3. In the process, one of the legs of each thermocouple was used as current conductor.

Experimental results

The resulting samples possessed stable *n*-type conductivity, and their thermoEMF and electric conductivity grew with a rise in temperature (Fig. 2). As is evident from the figures, doping of *PbTe* with *Sb* leads to improvement of its basic thermoelectric characteristics. Thus, for instance, the electric conductivity grows from the values of $\sigma \approx (100-200)\ (\Omega\cdot\text{cm})^{-1}$ for impurity-free *PbTe* to $\sigma \approx (700-800)\ (\Omega\cdot\text{cm})^{-1}$ for *PbTe* doped with 0.3 at.% *Sb*. The Seebeck coefficient in this case is reduced on the average by 50 μV/K over the entire temperature range, but the absolute value remains sufficiently high (≈ 300 μV/K). Increase in impurity concentration to 1.0 at. % *Sb* leads not only to essential reduction of the Seebeck coefficient, but also to decreased electric conductivity of doped samples.

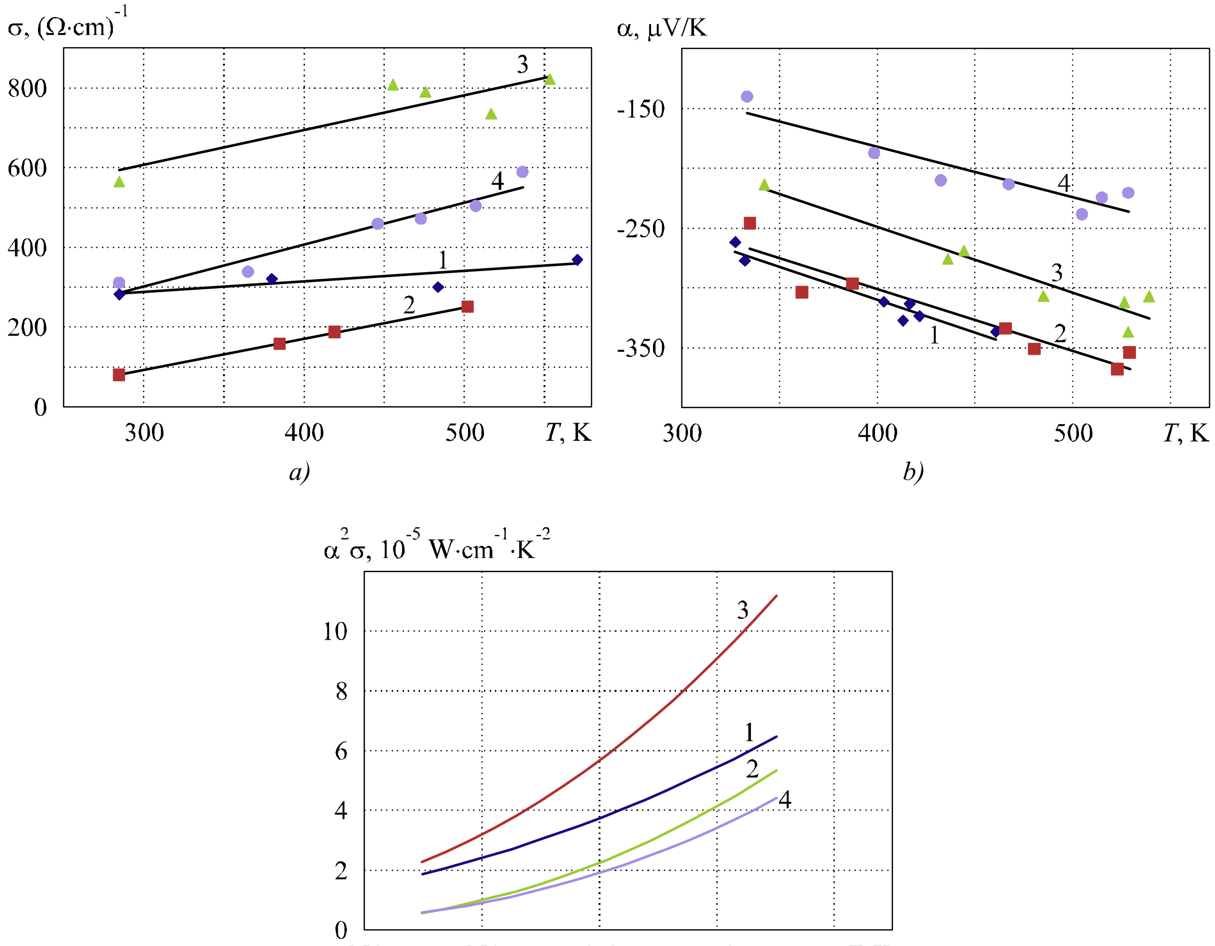

a) *b)*

c)

Fig. 2. The temperature dependence of electric conductivity σ (a), Seebeck coefficient α (b) and thermoelectric power α²σ (c) of PbTe:Sb. The content of Sb, at %: 1 (♦) – 0, 2 (■) – 0.1, 3 (▲) – 0.3, 4 (●) – 1.0.

Thus, based on the presented dependences, it can be stated that the optimal thermoelectric parameters are inherent in a material with impurity concentration 0.3 at.% *Sb*. The value of thermoelectric power for samples made of such material at a temperature of $\approx 500\ \mathrm{K}$ is $\alpha^2\sigma \approx 70\ \mu\mathrm{W/(K^2cm)}$, which is a fairly high figure.

Crystal-chemical doping mechanisms

The behaviour of electron concentration depending on the content of *Sb* impurity can be related to the character of crystalline structure defect subsystem – the kind of point defects and their charge state [5]. The fact that *Sb* can occupy both lead and tellurium positions in *PbTe* crystalline structure can be described by its charge state disproportioning. *Sb*, when substituting lead in its sublattice, is a donor. In so doing, it is ionized from $Sb^0(5s^25p^3)$ state to $Sb^{3+}(5s^25p^0) + 3e^-$ state. Relative to Pb^{2+} sublattice, the impurity is in $Sb^{3+} \to Sb^{1+}_{Pb}$ state. In tellurium sublattice *Sb* is ionized as $Sb^0(5s^25p^3) \to Sb^{3-}(5s^25p^6) + 3h^+$ and is an acceptor, with that, relative to Te^{2-} sublatice the impurity is in $Sb^{3-} \to Sb^{1-}_{Te}$ state. Hence, impurity disproportioning will be written as follows:

$$Sb^0 \to Sb^{3+}_{1-z} + Sb^{3-}_{z} + 3(1-z)e^- + 3zh^+. \tag{1}$$

Here z is the value of *Sb* charge state disproportioning. It is the ratio between the concentrations of Sb^{3+} and Sb^{3-} that will determine the donor or acceptor effect of doping impurity.

In terms of crystal-quasi-chemical approach based on the concept of antistructure [10], doping cluster for *Sb* impurity under condition of *Sb* ions location both in the cation and anion sublattices will be represented as follows:

$$V^{//}_{Pb}V^{\bullet\bullet}_{Te} + Sb^0 \to \left[V^{//}_{z}Sb^{\bullet}_{1-z}\right]_{Pb}\left[V^{\bullet\bullet}_{1-z}Sb^{/}_{z}\right]_{Te} + 3(1-z)e^- + 3zh^+. \tag{2}$$

Here $V^{//}_{Pb}V^{\bullet\bullet}_{Te}$ is *PbTe* antistructure, $V^{//}_{Pb}, V^{\bullet\bullet}_{Te}$ are *Pb* and *Te* vacancies, respectively, e^- is electron, $h^{\bullet}$ is hole, „/", „•", „*x*" are the negative, positive and neutral charges, respectively.

Crystal-quasi-chemical formula of *n-PbTe* with a complicated spectrum of point defects in the cation sublattice (single- and double-charge lead vacancies $V^{/}_{Pb}, V^{//}_{Pb}$), according to [11], is of the form:

$$\left[Pb^{x}_{1\text{-}\alpha\sigma}V^{//}_{\alpha\sigma(1\text{-}\delta)}V^{/}_{\alpha\sigma\delta}\right]_{Pb}\left[Te^{x}_{1\text{-}\alpha}V^{\bullet\bullet}_{\alpha}\right]_{Te}\left(Pb^{\bullet\bullet}_{\alpha\sigma}\right)_i + (2\alpha + \alpha\sigma\delta)e^-. \tag{3}$$

Its superposition with the doping cluster will represent the crystal-quasi-chemical formula of *n-PbTe*: *Sb*:

$$\begin{aligned}
&(1-x)\left\{\left[Pb^{x}_{1-\alpha\sigma}V^{//}_{\alpha\sigma(1-\delta)}V^{/}_{\alpha\sigma\delta}\right]_{Pb}\left[Te^{x}_{1-\alpha}V^{\bullet\bullet}_{\alpha}\right]_{Te}\left(Pb^{\bullet\bullet}_{\alpha\sigma}\right)_i + (2\alpha + \alpha\sigma\delta)e^{/}\right\} + \\
&+x\left\{\left[V^{//}_{z}Sb^{\bullet}_{1-z}\right]_{Pb}\left[V^{\bullet\bullet}_{1-z}Sb^{/}_{z}\right]_{Te} + 3(1-z)e^- + 3zh^+\right\} \to \\
&\to \left[Pb^{x}_{(1-x)(1\text{-}\alpha\sigma)}Sb^{\bullet}_{(1-z)x}V^{//}_{\alpha\sigma(1-\delta)(1-x)+zx}V^{/}_{\alpha\sigma\delta(1-x)}\right]_{Pb}\left[Te^{x}_{(1-\alpha)(1-x)}Sb^{/}_{zx}V^{\bullet\bullet}_{\alpha(1-x)+(1-z)x}\right]_{Te}\left(Pb^{\bullet\bullet}_{\alpha\sigma(1-x)}\right)_i + \\
&+\left\{\left(2\alpha + \alpha\sigma\delta\right)\left(1-x\right) + 3(1-z)x\right\}e^- + 3zxh^+.
\end{aligned} \tag{4}$$

Here, x is an atomic share of *Sb*, α is the value of initial deviation from stoichiometry on the side of *Pb*, δ is disproportioning coefficient of the charge state of lead vacancies, σ is the share of interstitial lead atoms.

The proposed doping mechanism and the obtained crystal-quasi-chemical formulae yield the analytical dependences of the concentration of individual point defects and current carriers on the deviation from stoichiometric composition in the basic compound α, the value of *Sb* atoms charge state disproportioning z and its content x. Thus, according to crystal-quasi-chemical formula, full electroneutrality equation will be written as follows:

$$\begin{gathered} n+\left|q_{V''_{Pb}}\right|[V''_{Pb}]+\left|q_{V'_{Pb}}\right|[V'_{Pb}]+\left|q_{Sb^{/}_{Te}}\right|[Sb^{/}_{Te}]= \\ p+\left|q_{V^{\bullet\bullet}_{Te}}\right|[V^{\bullet\bullet}_{Te}]+\left|q_{Pb^{\bullet\bullet}_{i}}\right|[Pb^{\bullet\bullet}_{i}]+\left|q_{Sb^{\bullet}_{Pb}}\right|[Sb^{\bullet}_{Pb}], \end{gathered} \tag{5}$$

where $n=A\big((2\alpha+\alpha\gamma\delta)(1-x)+3(1-z)x\big)$, $p=3Azx$ $[Sb^{/}_{Te}]=Azx$, $[V''_{Pb}]=A\big(\alpha\sigma(1-\delta)(1-x)+zx\big)$, $[V'_{Pb}]=A\alpha\sigma\delta(1-x)$, $[Sb^{\bullet}_{Pb}]=A(1-z)x$, $[V^{\bullet\bullet}_{Te}]=A\big(\alpha(1-x)+(1-z)x\big)$, $[Pb^{\bullet\bullet}_{i}]=A\alpha\sigma(1-x)$, $\left|q_{V'_{Pb}}\right| = \left|q_{Sb^{\bullet}_{Pb}}\right| = \left|q_{Sb^{/}_{Te}}\right| = 1$, $\left|q_{V''_{Pb}}\right| = \left|q_{V^{\bullet\bullet}_{Te}}\right| = \left|q_{Pb^{\bullet\bullet}_{i}}\right| = 2$. Here, $A=\frac{2Z}{a^3}$, Z is the number of structural units in the unit cell, a is lattice parameter. The Hall concentration of current carriers n_H in this case will be determined as:

$$n_H = A\left|(2\alpha+\alpha\gamma\delta)(1-x)+3(1-z)x-3zx\right|. \tag{6}$$

Figs. 3 to 5 represent calculations of the Hall concentration of current carriers and the concentration of point defects in *PbTe*:*Sb* crystals versus the impurity content and *Sb* atoms charge state disproportioning.

From the calculation of the Hall concentration (Fig. 3) it is seen that with the value of $z < 0.5$ the impurity has a donor effect ($[Sb^{1+}_{Pb}] > [Sb^{1-}_{Te}]$), and with the prevalence of antimony ions in tellurium positions ($z > 0.5$) – an acceptor effect. Thus, for the case of $z = 0.7$ with a growth in concentration of introduced impurity there is a decrease in the concentration of the major electrons, conversion of n- to p-type conductivity and further growth of hole concentration (Fig. 3 – curve 4). In the case of $z = 0.5$ (Fig. 3 – curve 3) there is full self-compensation of impurity (equal concentrations of Sb^{1+}_{Pb} and Sb^{1-}_{Te} ions) and the Hall concentration in both cases is reduced only marginally. The above behaviour peculiarities of the Hall concentration of current carriers versus the impurity content and its charge state are well illustrated in the space diagram (Fig. 4).

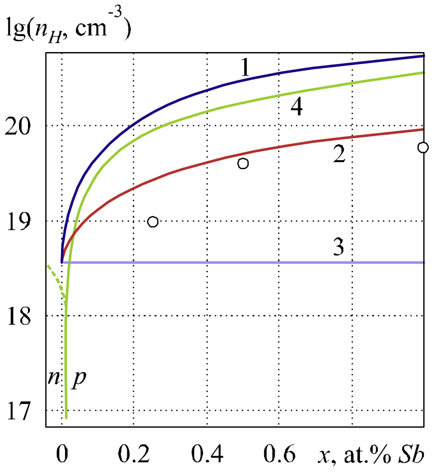

Fig. 3. The Hall concentration of current carriers in n-PbTe:Sb crystals versus Sb content for different values of Sb atoms charge state disproportioning z: 1 – 0.2; 2 – 0. 45; 3 – 0. 5; 4 – 0. 7. The points correspond to experiment [7], the curves – to calculation.

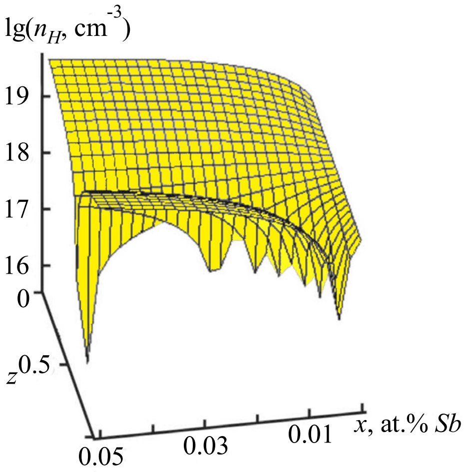

Fig. 4. Space diagram of the Hall concentration of current carriers for n-PbTe:Sb crystals versus the content of Sb x and the value of its charge state disproportioning z.

From the calculation of point defects concentration for the case of doping with *Sb* (Fig. 5) it is seen that the dominant defects are *Sb* ions introduced both into lead sublattice Sb_{Pb}^{+} and into tellurium sublattice Sb_{Te}^{-} of lead telluride, the concentration of which grows with increasing the content of *Sb* doping impurity. Considerable support to conductivity is also added by double ionized lead vacancies V_{Pb}^{2-} and double charged tellurium vacancies V_{Te}^{2+} whose concentration grows with increasing the impurity content.

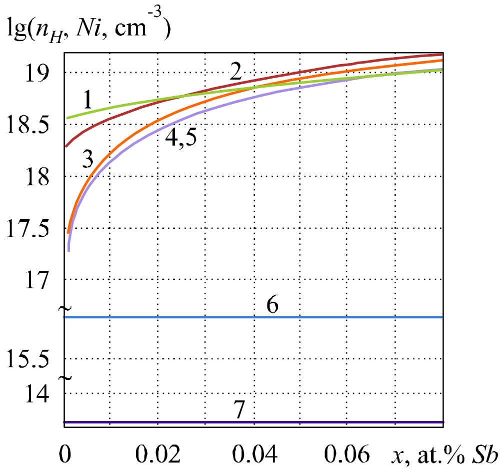

Fig. 5. The Hall concentration of current carriers (1 – n_H) and the concentration of dominant point defects N_i for n-PbTe:Sb crystals versus the content of Sb impurity (x) at z = 0.45.

N_i: 2 – $\left[V_{Te}^{2+}\right]$; 3 – $\left[Sb_{Pb}^{+}\right]$; 4 – $\left[Sb_{Te}^{-}\right]$; 5 – $\left[V_{Pb}^{2-}\right]$; 6 – $\left[Pb_{i}^{2+}\right]$; 7 – $\left[V_{Pb}^{-}\right]$; 8 – $\left[Te_{i}^{0}\right]$.

Analysis of investigation results

Based on the obtained experimental data, as well as the results of works [7, 12] on the donor impurity effect and taking into account possible models of crystal-chemical mechanisms of doping *n-PbTe*:*Sb*, it can be concluded that in our case the concentration of bismuth ions in Sb_{Pb}^{1+} state is in excess over Sb_{Te}^{1-} concentration. In particular, by comparison of the experimental data of the Hall concentration in *PbTe* versus the content of *Sb* [7] with the calculations performed (Fig. 3), the value of *Sb* impurity charge state disproportioning was determined as $z \approx 0.45$.

The character of obtained temperature dependences of the Seebeck coefficient corresponds to similar data in [12] and [7]. First, temperature growth causes an increase in the absolute value of α [7] and, second, on the concentration dependence of the Seebeck coefficient there is a maximum near the concentration of impurity 0.3 at.% *Sb* [12]. It is noteworthy that [7] dealt with investigation of crystalline samples cut of a synthesized ingot whose chemical formula is represented as $Pb_{1-x}Sb_xTe$. That is, the impurity was added with regard to substitution of lead atoms by *Sb* atoms. At the same time, in [12] the chemical formula of investigated samples obtained by the Bridgman method is represented as *PbTe*+*x* at.% *Sb*. In so doing, at room temperature and equal impurity concentrations, the Seebeck coefficient value for samples investigated in [12] exceeds almost twice a similar value for samples investigated in [7].

This regularity is confirmed by the results of the present and one of our previous works [13]. That is, from the standpoint of α increase, doping with *Sb* by adding to stoichiometric charge of *PbTe*, is more efficient. In so doing, the fabrication technique of thermoelectric samples, namely cutting of synthesized ingot, cutting of ingot obtained by the Bridgman method or the use of metalloceramic method is not a governing factor for the Seebeck coefficient increase in the course of doping.

A change in the electric conductivity of samples with increasing amount of introduced impurity (Fig. 2.) is similar to that obtained in [7] and differs from a similar dependence obtained in [12]. Thus, according to [12], the increased number of *Sb* in *PbTe* causes a monotone reduction of σ value in the concentration range from 0 to 0.5 at.% *Sb*, whereas in [7] there was a growth in the electric conductivity of samples with increasing impurity concentration from 0.25 to 0.5 at.% *Sb* and its subsequent reduction at 1.0 at.% *Sb*. Note that the numerical value of the electric conductivity of undoped samples ($\approx 300\ (\Omega\cdot\mathrm{cm})^{-1}$) is close to the value represented in [12] ($\approx 400\ (\Omega\cdot\mathrm{cm})^{-1}$).

The temperature change in electric conductivity, unlike that represented in [7], is characterized by a positive slope. Representation of $\sigma(T)$ dependence in $\ln(\sigma) - 1/T$ coordinates allowed estimating the activation energies of conductivity which for samples doped with Sb in the amount of 0.1 and 0.3 at. % is $\approx (0.01 - 0.02)$ eV.

Assuming that at temperatures under study the dominant mechanism is electron scattering on optical phonons [14-15], based on the obtained $\alpha(T)$ dependences one can determine the position of the Fermi level which is one of the basic characteristics of semiconductor material and largely defines its kinetic properties. For this purpose, the Pisarenko formula valid for carrier concentrations less than 10^{19} cm^{-3} [7] was used in the form:

$$\begin{aligned}\alpha &= \frac{k}{e}\left(\frac{5}{2} + r + \ln\left(\frac{N_C}{n}\right)\right) \\ &= \frac{k}{e}\left(\frac{5}{2} + r + \ln\left(\frac{N_C}{N_C \cdot F_{1/2}(\mu, T)}\right)\right) = \frac{k}{e}\left(\frac{5}{2} + r - \ln\left(F_{1/2}(\mu, T)\right)\right).\end{aligned} \tag{7}$$

Here, $N_C = (2\pi m_e^* kT / h^2)^{3/2}$ is the density of states in conduction band, $n = N_C \cdot F_{1/2}(\mu, T)$ is electron concentration in conduction band, $F_{1/2}(\mu, T)$ is the Fermi integral of order one-half.

From formula (7) we obtain $F_{1/2}(\mu, T) = \exp(5/2 + r - \alpha\cdot e/k)$. Then for impurity concentration 0.3 at.% *Sb* the chemical potential of electrons at a temperature of 300 K is 0.12 eV, and at 500 K – 0.05 eV. Accordingly, the electron concentrations are $\lg(n) = 18.6$ cm^{-3} and $\lg(n) = 18.1$ cm^{-3}. In so doing, it is taken into account that the effective mass of electrons is a function of their concentration [16]:

$$m^* = m_0\left(1+\frac{2\mu}{E_g}\right). \tag{8}$$

Hence, crystals under study are weakly degenerate semiconductors where electron concentration decreases with a rise in temperature. The same $n(T)$ dependence was obtained in Ref. [7].

However, despite the position of the Fermi level, it is more reasonable to use instead of formula (7) the dependence

$$S = \frac{k}{e}\cdot\frac{\pi^2}{3}\frac{kT}{\mu}\left(r+\frac{3}{2}\right), \tag{9}$$

which is valid exactly for the degenerate semiconductors [1].

In this case, for the impurity concentration 0.3 at % *Sb* the chemical potential of electrons at temperatures 300 K and 500 K is 0.075 eV and 0.080 eV, and the respective electron concentrations found with the use of a numerical calculation of the Fermi integral are equal to $\lg(n) = 18.54$ cm^{-3} and $\lg(n) = 18.97$ cm^{-3}. As with the use of (7), the effective mass dependence on their concentration was taken into account according to (8). Hence, with the use of (9) the electron concentration increases with a rise in temperature.

From the analysis of the calculated temperature dependence $n(T)$ represented in coordinates $\ln(n) - 1/T$ the activation energy 0.01 eV was obtained for *PbTe* crystals with *Sb* content 0.3 at. % *Sb*. Taking into account the proximity of determined activation energies from the temperature dependences of electric conductivity and electron concentration, it can be concluded that the main factor of σ growth is activation of electrons from defect levels, which is also confirmed by crystal-chemical analysis.

The obtained n values and represented in Fig. 2 $\sigma(T)$ dependences were used to determine the electron mobility. In particular, at impurity concentration 0.3 at.% *Sb* and temperatures 300 K and 500 K the values of μ are equal to ≈ 1180 (cm^2/V·s) and ≈ 540 (cm^2/V·s), respectively. Such high mobilities can testify to structural perfection of the obtained crystals.

It is noteworthy that the calculations performed are of approximate nature due to the fact that the semiconductor is weakly degenerate and the employed formulae are valid for material which is nondegenerate (7) and strongly degenerate (9). Besides, the Fermi integral used for the calculation of F and n, is represented in the approximation $E \sim k^2$, whereas in reality the conductivity band of *PbTe* is not parabolic.

Conclusions

1. Synthesis was conducted and the temperature dependences of the electric conductivity and the Seebeck coefficient of *Sb* doped lead telluride *n-PbTe*:*Sb* were studied. It was established that doping promotes improvement of the basic thermoelectric characteristics of material.
2. Based on the proposed crystal-quasi-chemical formulae for nonstoichiometric crystals *n-PbTe*:*Sb* taking into account a complicated spectrum of point defects in lead telluride (V_{Pb}^{2-}, V_{Pb}^{1-}, V_{Te}^{2+}, Pb_i^{2+}, Te_i^0) and different charge state of impurity atoms Sb^{3+} and Sb^{3-}, it was established that doping mechanism consists in the substitution by *Sb* atoms of both cation and anion vacancies, and its donor effect is determined by prevailing substitution by *Sb* atoms of cation vacancies ($[Sb_{Pb}^{1+}] > [Sb_{Te}^{1-}]$). The value of *Sb* impurity charge state disproportioning is $z = 0.45$.

3. Optimal parameters required of a material for *n*-legs of thermoelectric converters are inherent in lead telluride samples with the concentration of 0.3 at.% *Sb*, the thermoelectric power of which at a temperature of ≈ 500 K is $\alpha^2\sigma \approx 70$ μW/(K^2·cm). The obtained samples possess a perfect structure, as evidenced by high values of current carrier mobility (≈ 540 cm^2/V·s).

References

1. L.I. Anatychuk, *Thermoelements and Thermoelectric Devices* (Kyiv: Naukova Dumka, 1979), 768 p.
2. L.I. Anatychuk, *Thermoelectricity, Vol. 1, Physics of Thermoelectricity* (Kyiv, Chernivtsi: Institute of Thermoelectricity, 1998), 376 p.
3. E.P. Sabo, Technology of Chalcogenide Thermoelements. Thermoelectric Figure of Merit Improvement, *J. Thermoelectricity* **4**, 50 – 58 (2000).
4. V.F. Masterov, F.S. Nasredinov, S.A. Nemov, P.P. Seregin, N.N. Troitskaya, S.I. Bondarevsky, Position of Impurity Antimony Atoms in *PbTe* Lattice Determined by Emission Mőssbauer Spectroscopy Method, *Semiconductors* **34** (8), 1321 – 1322 (1997).
5. Yu.I. Ravich, B.A. Yefimova, and I.A. Smirnov, *Semiconductor Research Methods as Applied to Lead Chalcogenides* (Moscow: Nauka, 1968), 384 p.
6. S.A. Nemov, P.P. Seregin, S.M. Irkayev, and N.P. Seregin, Position of Impurity Arsenic Atoms in *PbTe* Lattice, *Semiconductors* **37** (3), 279 – 281 (2003).
7. Chr. Jaworski, J. Tobola, E.M. Levin, Kl. Schmidt-Rohr, and J. Heremans, Antimony as an Amphoteric Dopant in Lead Telluride, *Physical Review B* **80**, 125208-1 – 125208-10 (2009).
8. G.A. Bordovsky, S.A. Nemov, A.V. Marchenko, A.V. Zaitseva, M.Yu. Kozhokar, P.P. Seregin, States of Antimony and Tin Atoms in Lead Chalcogenides, *Semiconductors* **45** (4), 437 – 440 (2011).
9. O.I. Vlasenko, S.M. Levitsky, C.A. Kryskov, and A.A. Kryskov, *Patent of Ukraine 43898*, Method for Preparation of Highly Homogeneous A_4B_6 Chalcogenide Semiconductor Materials, 2009.
10. S.S. Lysnyak, Crystal-Quasi-Chemical Model of Research in Solid State Chemistry, *Inorganic Materials* **32** (2), 1913 – 1917 (1992).
11. V.M. Boichuk, O.V. Tkachik, L.V. Turovska, and N.I. Dikun, Crystal-Quasi-Chemical Formulae of Nonstoichiometric Lead Telluride with a Complicated Spectrum of Point Defects and Self-Doping Processes, *Physics and Chemistry of Solid State* **8** (2), 366 – 373 (2007).
12. L.D. Borisova, Thermoelectric Properties of Impurity Doped *PbTe*, *Phys. Stat. Sol. (a)* **53**, K 19 – K22 (1979).
13. D.M. Freik, I.V. Horichok, R.O. Dzumedzei, Yu.V. Lysyuk, V.P. Koznyuk, and A.P. Koznyuk, Synthesis and Thermoelectric Properties of *PbTe*:*Sb*, Physics and chemistry of Solid State **13** (1), 220 – 223 (2012).
14. R.O. Dzumedzei, High-Temperature Scattering in Doped Crystals of Lead Telluride *PbTe*:*Sb*(*Bi*, *In*), *Physics and Chemistry of Solid State* **11** (4), 844 – 848 (2010).
15. D.M. Zayachuk, On the Issue of Dominant Mechanisms of Charge Carrier Scattering in Lead Telluride, *Semiconductors* **31** (2), 217 – 221 (1997).
16. I.N. Dubrovskaya, Yu.I. Ravich, Research on the Nonparabolicity of *PbTe* Conduction Band by Measuring ThermoEMF in a Strong Magnetic Field, *Physics of the Solid State* **8** (5), 1455 – 1460 (1966).

Submitted 28.11.2012.

V.A. Romaka[1,2], Yu.V. Stadnyk[3], P. Rogl[4], V.V. Romaka[2],
V.Ya. Krayovsky[2], O.I. Lakh[5], A.M. Horyn[3]

[1] Ya. Pidstryhach Institute for Applied Problems of Mechanics and Mathematics National Academy of Sciences of Ukraine, 3-b, Naukova Str., Lviv, 79060, Ukraine;
[2] National University "Lvivska Polytechnika", 12, S. Bandera Str., Lviv, 79013,Ukraine;
[3] Ivan Franko National University of Lviv, 6, Kyryla and Mefodiya Str., 79005, Lviv, Ukraine;
[4] Institut für Physikalische Chemie, Universität Wien, Wien, A-1090, Austria;
[5] V.I. Lakh NVO "Termoprylad", 3, Naukova Str., 79060, Lviv, Ukraine;

PARAMETER OPTIMIZATION OF THERMOELECTRIC MATERIAL BASED ON *n-ZrNiSn* INTERMETALLIC SEMICONDUCTOR

The structural, energy, electrokinetic and magnetic characteristics of intermetallic n-ZrNiSn semiconductor heavily doped with Ni impurity are investigated. A new method for parameter optimization of thermoelectric material based on n-ZrNiSn using peculiarities of its crystalline structure is proposed. The mechanism for accumulation in the tetrahedral voids of ZrNiSn compound of both intrinsic and impurity excess atoms generating previously unknown energy levels in the semiconductor is established. It is shown that the obtained thermoelectric material $(Zr_{1-y}Ni_y)Ni_{1+x}Sn$ *has high efficiency of thermal into electric energy conversion in the range of investigated temperatures.*

Key words: crystal and electronic structures, semiconductor, conduction.

Introduction

It is known that parameter optimization of thermoelectric materials to obtain maximum values of thermoelectric figure of merit *Z* depends on a series of factors, in particular, current carrier concentration, scattering mechanisms, thermal conductivity, the choice of crystallographic orientation, etc. [1]. Therefore, it is precisely these factors that formed the basis for an algorithm of a new method for parameter optimization of thermoelectric material based on intermetallic *n-ZrNiSn* semiconductor proposed below.

Analyzing the results of studies on *n-ZrNiSn* semiconductor, as well as thermoelectric materials on its basis in various research centres [2-6], we have revealed the presence of essential differences (orders of magnitude) in parameter values under identical temperatures, in particular, electric conductivity, the Seebeck coefficient, thermal conductivity and magnetic susceptibility. Since the purity of precursor components of *ZrNiSn* compound is almost the same in all research laboratories and synthesis methods are also similar, then what is it that provokes the irreproducibility of *n-ZrNiSn* characteristics and virtually eliminates it from the range of materials that can be used for thermal into electric energy conversion?

In the present work, we have not only found the reason for such behaviour of *n-ZrNiSn* characteristics, but on the basis of identified solutions we propose a new method for parameter optimization of thermoelectric material based on *n-ZrNiSn* semiconductor, using the established features of its crystalline and electronic structures. It was preceded by the following reasoning.

1. We proceeded from the assumption that semiconductor properties are largely determined by

the concentration and type of impurities, as well as the depth of their occurrence and the concentration ratio of acceptors and donors (compensation degree) [7]. Therefore, structural defects of *n-ZrNiSn* were analyzed as one of the sources of semiconductor impurity states. Thus, in [6] it was established that crystalline structure of *ZrNiSn* compound is disordered, i.e. crystallographic position of *Zr* ($4d^2 5s^2$) atoms up to~ 2 at.% ($y \leq 0.02$) is occupied with *Ni* ($3d^8 4s^2$) atoms which generates donor-nature structural defects and makes the semiconductor heavily doped and compensated [7]. Precisely this “self-doping” or “a priori doping” method [8] assures the electron type of semiconductor conductivity. In the presence of this structural defect, the compound formula is transformed and has the form of $(Zr_{1-y}Ni_y)NiSn$. Besides, it was established that under certain conditions, in particular, on introducing the atoms of rare-earth metals into *ZrNiSn* compound, its structure is arranged in an ordered fashion, i.e. the smallest-size *Ni* atoms ($r_{Ni} = 0.125$ nm) return from *Zr* position ($r_{Zr} = 0.160$ nm) to position of their own [6].

2. Analyzing phase equilibrium diagram of *Zr-Ni-Sn* system, we noticed that alongside with *ZrNiSn* compound (structural type *MgAgAs*, space group $F\bar{4}3m$), there is $ZrNi_2Sn$ compound (structural type $MnCu_2Al$, space group $Fm\bar{3}m$). Moreover, it turned out that crystalline structures of the above compounds are related [9]. The difference in them lies in the fact that in *ZrNiSn* compound coordination of *Ni* atoms around *Sn* atoms is tetrahedral, whereas in $ZrNi_2Sn$ it is octahedral. The absence of symmetry centre in *ZrNiSn* is caused by the presence of strong tetrahedral covalent bonds between atoms which, on the one hand, is a guarantee of semiconductor compound properties, and, on the other hand, creates in the unit cell a volume making ~ 24 % from the total one which is unoccupied with atoms (the tetrahedral void) (Fig. 1).

By the “relationship” crystallographers mean the following. If we assume hypothetically that the smallest-size *Ni* atoms can be arranged in the tetrahedral voids of *ZrNiSn* and consider a void as a vacancy (*Vac*) of crystallographic position 4*d*, then occupation by *Ni* atom of 4*d* position (vacancy occupation) will result in a change of crystal symmetry and realization under certain *Ni* concentrations of $ZrNi_2Sn$ compound.

Based on the relationship between crystalline structures of *ZrNiSn* and $ZrNi_2Sn$ compounds, we asked ourselves the following questions:

a) can *Ni* atoms in *ZrNiSn* compound, apart from being arranged in their own crystallographic position and partially (up to 2 at.%) in *Zr* position [6], not hypothetically, but virtually occupy the tetrahedral voids of *ZrNiSn* crystalline structure, generating thereby the earlier unknown structural defects which will result in the redistribution of semiconductor electron density and change its properties? In other words, can tetrahedral voids available in the structure act as traps and accumulate both the excess atoms of *ZrNiSn* compound components and other controlled or uncontrolled impurity atoms?

b) if a certain number of atoms, say, *Ni*, is accumulated in the tetrahedral void of *ZrNiSn,* is the resulting structural defect of a donor, acceptor or neutral nature?

в) how many excess atoms of the smallest-size *Ni* can be accumulated in the unit cell of a semiconductor, without changing its crystalline structure?

Below, based on the results of experimental studies and theoretical calculations, we will show that in *ZrNiSn* compound *Ni* atoms can simultaneously occupy both their own crystallographic position and partially position of *Zr* atoms [6], as well as be arranged in the tetrahedral voids of compound crystalline structure (Fig. 1), generating the earlier unknown donor-nature structural defects. In other words, a situation is created when the excess number of Ni_{1+x} atoms is accumulated in *ZrNiSn* crystal, and compound formula is $(Zr_{1-y}Ni_y)Ni_{1+x}Sn$. With a certain number of excess *Ni* atoms, another $ZrNi_2Sn$ compound is formed. It is precisely the mechanism of accumulation in the tetrahedral voids of *ZrNiSn* compound of both excess and impurity atoms that generates new energy levels in the semiconductor accounting for the characteristics irreproducibility of *n-ZrNiSn* synthesized in various research centres [2-6].

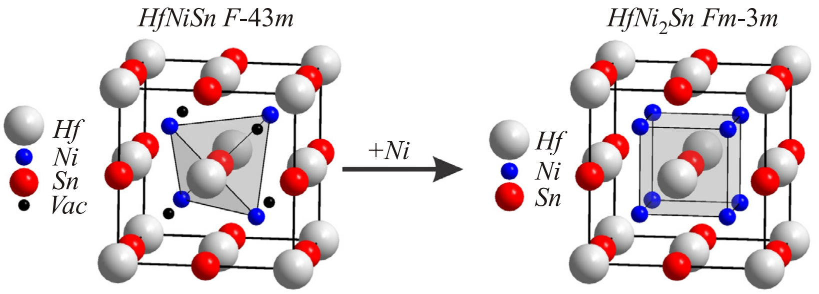

Fig. 1. Transformation of crystalline structure of ZrNiSn compound in $ZrNi_2Sn$ *while accumulating excess* Ni_{1+x} *atoms in the tetrahedral voids (occupation of vacant positions by Ni atoms).*

Note that our new method of doping *n-ZrNiSn* semiconductor with *Ni* donor impurity meets the condition of getting maximum values of thermoelectric power factor [10].

Research methods

The object to be investigated included crystalline structure, electron density distribution (DOS), electrokinetic, magnetic and energy characteristics of $(Zr_{1-y}Ni_y)Ni_{1+x}Sn$. The samples were synthesized in the laboratory of Institute for Physical Chemistry, Vienna University. Structural studies were performed for samples of composition $(Zr_{1-y}Ni_y)Ni_{1+x}Sn$, $x = 0 \div 1.0$ and electrokinetic and magnetic – for $x = 0 \div 0.10$. The *X*-ray structural analysis method was used to obtain the values of $(Zr_{1-y}Ni_y)Ni_{1+x}Sn$, $x = 0 \div 0.10$ crystal lattice periods and to establish its parameters: atom coordinates, thermal parameters and occupancy of crystallographic positions [11]. The data arrays obtained by powder method with a stepwise recording of Bragg reflections intensity were used (diffractometer Guinier-Huber image plate system, $CuK\alpha_1$-radiation; $8° \leq 2\theta \leq 100°$). Calculations related to interpretation and refinement of $(Zr_{1-y}Ni_y)Ni_{1+x}Sn$ crystalline structure were made with the use of WinCSD program [12]. The phase and chemical compositions were controlled by scanning electron microscope (SEM, Zeiss Supra 55VP) and microprobe analyzer (EPMA, energy-dispersive *X*-ray analyzer). The calculation of DOS was made by KKR-CPA-LDA method (AkaiKKR program [13]). The temperature and concentration dependences of the electrical resistivity ρ, the Seebeck coefficient α and magnetic susceptibility χ of $(Zr_{1-y}Ni_y)Ni_{1+x}Sn$ were measured in the ranges: $T = 80 \div 400$ K, $N_D^{Ni} \approx 9.5 \cdot 10^{19}$ cm^{-3} $(x = 0.005 \div 0.1) \div 1.9 \cdot 10^{21}$ cm^{-3} and magnetic field intensity $H \leq 10$ kgf.

Research on $(Zr_{1-y}Ni_y)Ni_{1+x}Sn$ crystalline structure

X-ray phase and structural analyses have shown that the investigated samples of $(Zr_{1-y}Ni_y)Ni_{1+x}Sn$, $0 \leq x \leq 0.30$ and $0.65 \leq x \leq 1.0$ are single-phase, *X*-ray diffractograms are indexed in *MgAgAs* and $MnCu_2Al$ structural types, respectively, and Bragg R_{Br} factor of a discrepancy between crystalline structure model and the experimental results of structural studies does not exceed 1 % (Table). The composition of semiconductor solid solution $(Zr_{1-y}Ni_y)Ni_{1+x}Sn$, $x \leq 0.30$, fixes the solubility limit of *Ni* atoms in the structure of *ZrNiSn* compound. At the same time, samples of compositions $(Zr_{1-y}Ni_y)Ni_{1+x}Sn$, $0.30 \le x \le 0.65$ are not single-phase, pointing to the absence of a continuous solid solution between *ZrNiSn* and $ZrNi_2Sn$ compounds.

Table

Structural and metallographic characteristics of $ZrNi_{1+x}Sn$, $(0 \le x \le 1)$

Compound composition	$ZrNi_{1+x}Sn$ $(0 \le x \le 0.3)$		$ZrNi_{1+x}Sn$ $(0.65 \le x \le 1)$
Space group	$F\bar{4}3m$, *MgAgAs*		$Fm\bar{3}m$, $MnCu_2Al$
Composition (SEM), at. %	$Zr_{32.5}Ni_{35.5}Sn_{32.5}$	$Zr_{31.5}Ni_{37.5}Sn_{31.0}$	$Zr_{27.5}Ni_{46.7}Sn_{27.0}$
Composition (EPMA), at.%	$Zr_{33.1}Ni_{33.8}Sn_{33.1}$	$Zr_{33.0}Ni_{34.0}Sn_{33.0}$	$Zr_{25.6}Ni_{48.9}Sn_{25.6}$
a (nm)	0.611173(2)	0.611081(3)	0.627252(7)
R_{Br} (%)	0.0084	0.0069	0.0172
Atom parameters:			
Zr in 4*a* (0, 0, 0)	–	–	–
B_{iso} (10^2 nm^2)	0.92(4)	0.57(6)	0.41(11)
Sn in 4 *b* (1/2, 1/2, ½)	–	–	–
B_{iso} (10^2 nm^2)	0.36(3)	0.38(5)	0.54(9)
Ni in position:	4*d* (3/4, 3/4, 3/4)	8*c* (1/4, 1/4, 1/4)	*Ni* in position:
Ni/*Vac*.	0.09/3.91	0.13/3.87	*Ni*/*Vac*.
B_{iso} (10^2 nm^2)	0.86(4)	0.87(5)	B_{iso} (10^2 nm^2)
Ni in 4*c* (1/4, 1/4, 1/4)	–	–	*Ni* in 4*c* (1/4, 1/4, 1/4)
B_{iso} (10^2 nm^2)	0.86(4)	0.87(5)	B_{iso} (10^2 nm^2)

The fact that the investigated samples comprise an excess number of Ni_{1+x} atoms whose concentration corresponds to the composition of input components charge mixture is empirically supported by the results of measuring concentration of *Ni* atoms on the surface of samples (Table). In so doing, which is of principal importance, the spatial relationship of atoms in the basic array of compound compositions $(Zr_{1-y}Ni_y)Ni_{1+x}Sn$, $0 \le x \le 0.30$ and $0.65 \le x \le 1.0$, is not changed. This is indicated by the low values of R_{Br} factor of a discrepancy between the experimental results and the model arrangement of atoms in a space typical of structural types *MgAgAs* and $MnCu_2Al$ (Table).

As long as we are interested in *ZrNiSn* compound, it is reasonable to ask: where are Ni_{1+x} excess atoms accumulated in $(Zr_{1-y}Ni_y)Ni_{1+x}Sn$, $0 \le x \le 0.30$, and what is the nature of structural defects generated thereby which define the semiconductor properties?

The refinement of crystalline structure of $(Zr_{1-y}Ni_y)Ni_{1+x}Sn$, $0 \le x \le 0.30$ samples has shown that when excess Ni_{1+x} atoms are arranged in crystallographic position 4*d* (the tetrahedral void), the discrepancy factor does not exceed 0.8 %, which is even slightly incorrect, since it exceeds the accuracy of the measuring system. Thus, doping of *n-ZrNiSn* semiconductor with *Ni* atoms results in the formation of point structural defects – *Ni* atoms in the interstitial site (the tetrahedral voids), the type of which will be established from the results of calculating the semiconductor electron structure and the electrokinetic properties.

The refinement of crystalline structure of samples also allowed establishing an important result which in the future will help to identify the type of defects that are generated in the crystal. It turned out that doping of *n-ZrNiSn* with *Ni* atoms is accompanied by ordering semiconductor crystalline structure through return of Ni_y atoms from *Zr* crystallographic position to their own crystallographic position (Fig. 2). If we take into account that exactly Ni_y atoms, partially occupying *Zr* crystallographic position, generate donor-nature structural defects in the crystal, then ordering of crystalline structure on introduction of excess Ni_{1+x} atoms will be accompanied by a decrease in donor concentration ("healing" of donor-nature structural defects). As can be seen from Fig. 2, at concentration of excess Ni_{1+x} atoms that corresponds to compositions $(Zr_{1-y}Ni_y)Ni_{1+x}Sn$, $x \geq 0.07$, there are no donor-nature structural defects in the crystal that are related to "a priori doping" of a semiconductor.

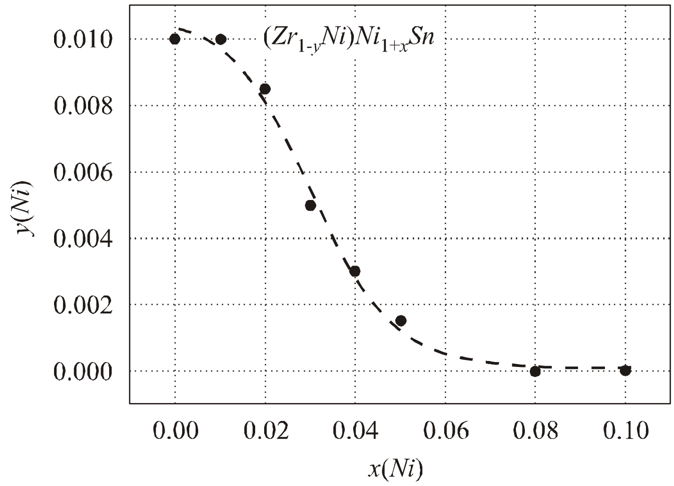

Fig. 2. Dynamics of change in the concentration of Ni_y *atoms in Zr crystallographic position* $(Zr_{1-y}Ni_y)Ni_{1+x}Sn$, $x \leq 0.10$.

Thus, structural studies of *n-ZrNiSn* heavily doped with *Ni* atoms have confirmed the above assumption that crystal can accumulate an excess amount of Ni_{1+x} atoms in the tetrahedral voids. In so doing, in a semiconductor there takes place a dynamic change in the compensation degree which reduces the concentration of donor-nature defects related to a reduced amount of donor-nature structural defects (Ni_y atoms in *Zr* position). At the same time, structural studies cannot identify the nature of defects that arose while accumulating Ni_{1+x} atoms in the semiconductor tetrahedral voids.

Research on electron density distribution in $(Zr_{1-y}Ni_y)Ni_{1+x}Sn$

To predict the behaviour of the Fermi level ε_F, the energy gap ε_g, the electrokinetic and magnetic characteristics of *n-ZrNiSn* doped with *Ni* atoms, the electron density distribution was calculated with regard to the contribution of Ni_{1+x} excess atoms located in the tetrahedral voids of semiconductor structure. Taking into consideration that introduction of excess Ni_{1+x} atoms into *ZrNiSn* compound arranges in an ordered fashion its crystalline structure, calculation of DOS was carried out for the case of ordered crystalline structure. Introduction of excess Ni_{1+x} atoms into concentrations of $(Zr_{1-y}Ni_y)Ni_{1+x}Sn$, $0 \leq x \leq 0.30$, does not radically change the shape of electron density distribution in conformity to hybridization between all the elements (Fig. 3). There is an increase in the "tails" of continuous energy bands, leading to a slight reduction in the values of efficient energy gap (Fig. 4 *a*, insert) in $(Zr_{1-y}Ni_y)Ni_{1+x}Sn$.

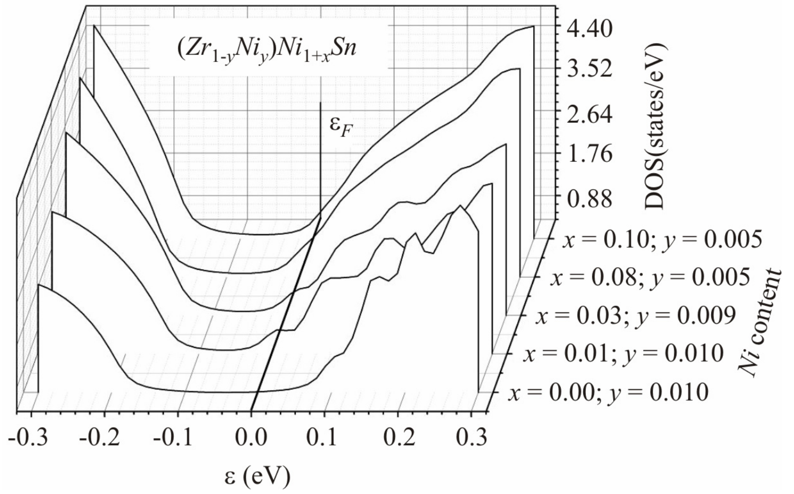

Fig. 3. Calculation of change in the edge profiles of continuous energy bands in $(Zr_{1-y}Ni_y)Ni_{1+x}Sn$.

As is evident from Fig. 4 *b*, with an increase in concentration of Ni_{1+x} atoms, the density of states on the Fermi level DOSε_F in $(Zr_{1-y}Ni_y)Ni_{1+x}Sn$ is also increased, and the Fermi level moves in the direction of conduction band (Fig. 4 *a*, dependence 1). In a semiconductor, this is possible only on condition of its doping with donor impurity. Note that the results of calculating the position of the Fermi level relative to the edge of conduction band in $Zr_{1-y}Ni_y)Ni_{1+x}Sn$ are of a more complicated character than a regular drift due to the effect of electron-type *Ni* donor impurity introduced into a semiconductor. Apart from the drift caused by a reduction in semiconductor compensation degree, there is also a reduction in the values of effective energy gap ε_g from $\varepsilon_g\,(x = 0) = 287.7$ meV to $\varepsilon_g\,(x = 0.01) = 181.7$ meV due to increase in band "tails" changing the profile of continuous energy bands (Fig. 4 *a*, insert).

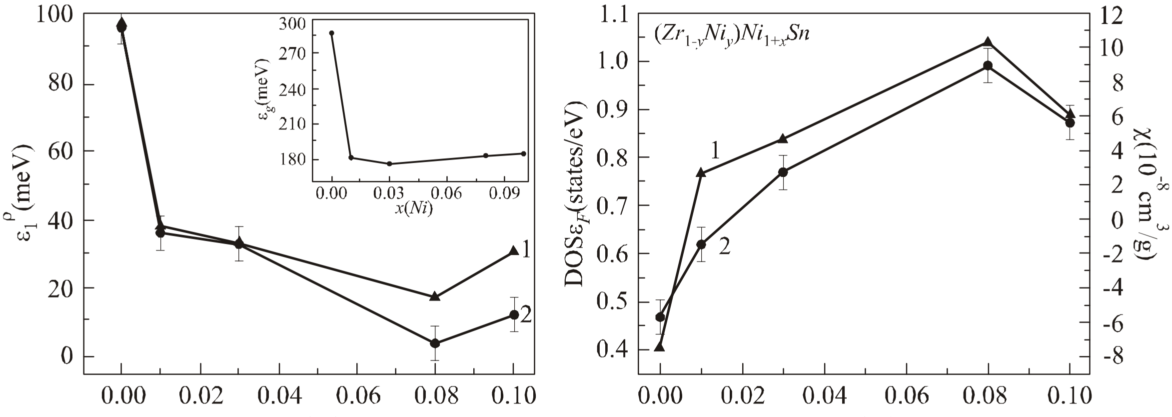

a)

b)

Fig. 4. A change in the values of activation energy ε_1^{ρ} *from the Fermi level to percolation level of conduction band (a): 1 – from* ln$\rho(1/T)$ *dependences; 2 – calculation; insert – energy gap* ε_g *and density of states on the Fermi level DOS*ε_F *(1), magnetic susceptibility* χ *(2) at* $T = 300$ *K, (b)* $(Zr_{1-y}Ni_y)Ni_{1+x}Sn_x$.

Thus, the results of calculation of electron density distribution in $(Zr_{1-y}Ni_y)Ni_{1+x}Sn_x$ based on the results of structural research point to a donor nature of generated structural defects, and experimental studies will allow checking the adequacy of calculation results, hence of selected model of semiconductor structure.

Research on the magnetic characteristics of $(Zr_{1-y}Ni_y)Ni_{1+x}Sn$

Research on the field and temperature dependences of magnetic susceptibility χ $(Zr_{1-y}Ni_y)Ni_{1+x}Sn$ provided additional information as to the reasons for a change in the electronic structure of a semiconductor. Fig. 4 *b* shows the results of measuring $\chi(x)$ values at $T = 300$ K and magnetic field intensity $H = 10$ kgf. The *n-ZrNiSn* is known to be a weak diamagnetic ($\chi_{x=0} = -0.057\cdot10^{-6}$ cm^3/g) [8]. Introduction of weak concentrations of Ni_{1+x} atoms reduces the diamagnetic component $\chi_{x=0.01} = -0.015\cdot10^{-6}$ cm^3/g, and with the concentration $x \geq 0.03$ the semiconductor becomes the Pauli paramagnetic and $\chi_{x=0.03} = 0.027\cdot10^{-6}$ cm^3/g. In this case, the magnetic susceptibility $(Zr_{1-y}Ni_y)Ni_{1+x}Sn$ is governed by the major carriers, and its values are proportional to concentration of free electrons n (for the Pauli paramagnetic $\chi \sim n$). Taking into account that $\chi(x)$ dependence in $(Zr_{1-y}Ni_y)Ni_{1+x}Sn$ grows, we can state that donor-nature structural defects are generated in the crystal when the tetrahedral voids are occupied by *Ni* atoms.

Research on the electrokinetic characteristics of $(Zr_{1-y}Ni_y)Ni_{1+x}Sn$

The temperature dependences of electric resistivity $\ln\rho(1/T)$ and the Seebeck coefficient $\alpha(1/T)$ for samples of $(Zr_{1-y}Ni_y)Ni_{1+x}Sn$, $x = 0 \div 0.10$ are represented in Fig. 5 and are typical of doped and compensated semiconductors with high and low-temperature activation regions. Such regions of dependences $\ln\rho(1/T)$ were used to calculate the values of activation energy from the Fermi level ε_F to percolation level of conduction band (ε_1^{ρ}) and electron hops (ε_3^{ρ}) in the states with energies close to ε_F, and dependences $\alpha(1/T)$ were used to calculate the values of activation energies ε_1^{α} and ε_3^{α}, proportional to modulation amplitude of continuous energy and small-scale fluctuation zones, respectively [14].

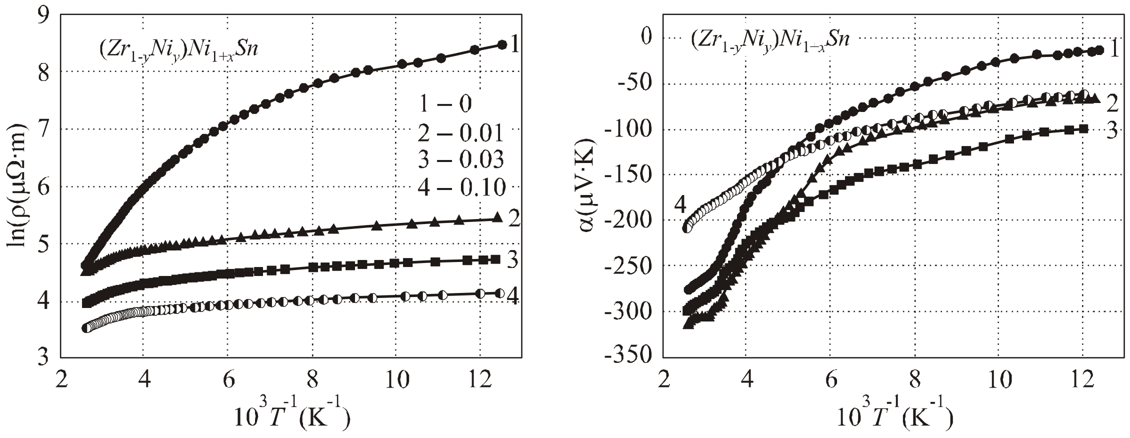

a) *b)*

Fig. 5. Temperature dependences of electric resistivity ρ *(a) and the Seebeck coefficient* α *(b)* $(Zr_{1-y}Ni_y)Ni_{1+x}Sn$: *1 – x = 0; 2 – x = 0.01; 3 – x = 0.03; 4 – x = 0.10.*

As can be seen from Figs. 5 *b* and 6 *b*, the Seebeck coefficient $(Zr_{1-y}Ni_y)Ni_{1+x}Sn$, $x = 0$, (*n-ZrNiSn*) has negative values, and electrons are major carriers. This is a well-known and expected result which is related to the donor nature of intrinsic structural defects in a semiconductor due to partial occupation by Ni_y atoms of *Zr* crystallographic position ("a priori doping") [6]. In this case, the Fermi level ε_F is located close to the bottom of conduction band at the distance of $\varepsilon_1^{\rho}(x = 0) = 97.6$ meV from the percolation level, and $\varepsilon_1^{\alpha}(x = 0) = 83.8$ meV determines the modulation amplitude of continuous energy bands of *n-ZrNiSn* (Fig. 4 *a*).

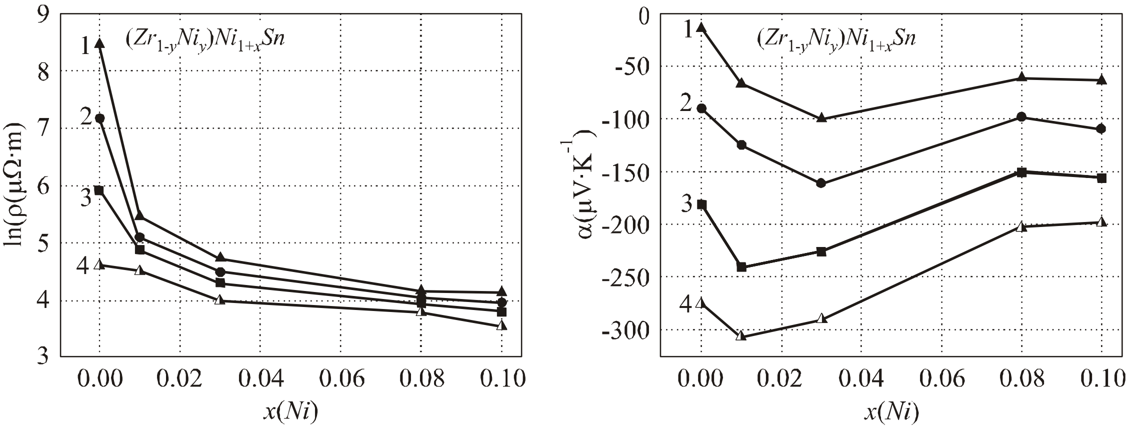

a) *b)*

Fig. 6. A change in the values of electric resistivity ρ *(a) and the Seebeck coefficient* α *(b)* $(Zr_{1-y}Ni_y)Ni_{1+x}Sn$ *at different temperatures: 1 – T = 80 K; 2 – T = 160 K; 3 – T = 250 K; 4 – T = 380 K.*

Introduction into *ZrNiSn* compound of the smallest concentrations of Ni_{1+x} atoms leads to a drastic reduction of electric resistivity values, for instance, at 80 K, from the values of $\rho(x = 0) = 4751.1$ μOhm·m to $\rho(x = 0.01) = 231.0$ μOhm·m and $\rho(x = 0.10) = 62.8$ μOhm·m. Such behaviour of $\rho(x)$ dependence testifies that donor-nature structural defects are created in the crystal whose concentration grows with increasing the content of Ni_{1+x} atoms. This is regardless of the fact that, as follows from structural studies, introduction of excess Ni_{1+x} atoms first reduces the number of donor-nature structural defects due to return of Ni_y atoms from *Zr* position to their own crystallographic position.

Thus, the results of electrokinetic research on $(Zr_{1-y}Ni_y)Ni_{1+x}Sn$ lead to the conclusion as to the donor type of defects generated in the crystal of *ZrNiSn* compound while introducing excess Ni_{1+x} atoms and accumulating these atoms in the tetrahedral voids of the structure. In this case, the degree of semiconductor compensation is reduced, and the dependence in Fig. 2 describes the dynamics of change in the number of various types of structural defects of $(Zr_{1-y}Ni_y)Ni_{1+x}Sn$.

The fact that donor-nature structural defects are generated in the crystal while introducing excess Ni_{1+x} atoms is evidenced by the character of the Fermi level drift in the direction of conduction band (Fig. 4 *a*, dependence 1). We can see that introducing the lowest concentrations of excess Ni_{1+x} atoms into *n-ZrNiSn* is accompanied by a drastic decrease in the values of activation energy ε_1^{ρ} from the Fermi level to percolation level of conduction band from $\varepsilon_1^{\rho}(x = 0) = 97.6$ meV to $\varepsilon_1^{\rho}(x = 0.01) = 38.3$ meV. On the other hand, if the degree of semiconductor compensation is reduced, then it is quite logical that the values of modulation amplitude of continuous energy bands [7] will be reduced to values $\varepsilon_1^{\alpha}(x = 0.01) = 51.4$ meV and $\varepsilon_1^{\alpha}(x = 0.10) = 31.9$ meV. Besides, exactly due to this at low temperatures the length of electron hop ε_3^{ρ} will decrease in the states close to the Fermi energy from the values of $\varepsilon_3^{\rho}(x = 0) = 11.5$ meV to $\varepsilon_3^{\rho}(x = 0.01) = 4.4$ meV and $\varepsilon_3^{\rho}(x = 0.08) = 1.4$ meV. Note that concentration of excess Ni_{1+x} atoms introduced into *n-ZrNiSn* proved to be insufficient for the intersection by the Fermi level of the percolation level of conduction band and realization of dielectric-metal transition in the conductivity [7].

Thus, the experimentally observed drastic decrease in the values of electric resistivity $\rho(x)$ (Fig. 6 *a*), activation energy $\varepsilon_1^{\rho}(x)$ from the Fermi level to the percolation level of conduction band (Fig. 4 *a*), as well as the negative values of the Seebeck coefficient $\alpha(x)$ is related both to increased concentration of donor-nature defects and decreased energy gap between continuous energy bands, which facilitates throwing of electrons from the donor levels to the conduction band of a heavily doped and compensated semiconductor $(Zr_{1-y}Ni_y)Ni_{1+x}Sn$. This statement makes specific the consequence of structural research and confirms that which is based on the results of calculating the semiconductor electronic structure and its magnetic characteristics.

Thermoelectric power factor of $(Zr_{1-y}Ni_y)Ni_{1+x}Sn$

Maximum values of thermoelectric power factor Z^* ($Z^* = \alpha^2\sigma$, where α is the Seebeck coefficient, σ is electric conductivity) are attained under condition when the Seebeck coefficient is still high and the electric conductivity values of $(Zr_{1-y}Ni_y)Ni_{1+x}Sn$ semiconductor solid solution have become even higher [10]. Under these conditions, on $Z^*(x)$ dependences there are extremes at all temperatures under study. Fig. 7 *a* shows $Z^*(x)$ dependence from which it is seen that the value of thermoelectric factor in $(Zr_{1-y}Ni_y)Ni_{1+x}Sn$ is higher than in the undoped semiconductor *n-ZrNiSn*. Besides, with a rise in temperature the absolute values of $Z^*(T)$ are still further increased (Fig. 7 *b*). Taking into account that calculations show a slight (by ~ 5 %) increase of thermal conductivity κ for $(Zr_{1-y}Ni_y)Ni_{1+x}Sn$, $x = 0.03$, the values of thermoelectric figure of merit Z with this impurity concentration will be higher than in the undoped semiconductor *n-ZrNiSn*.

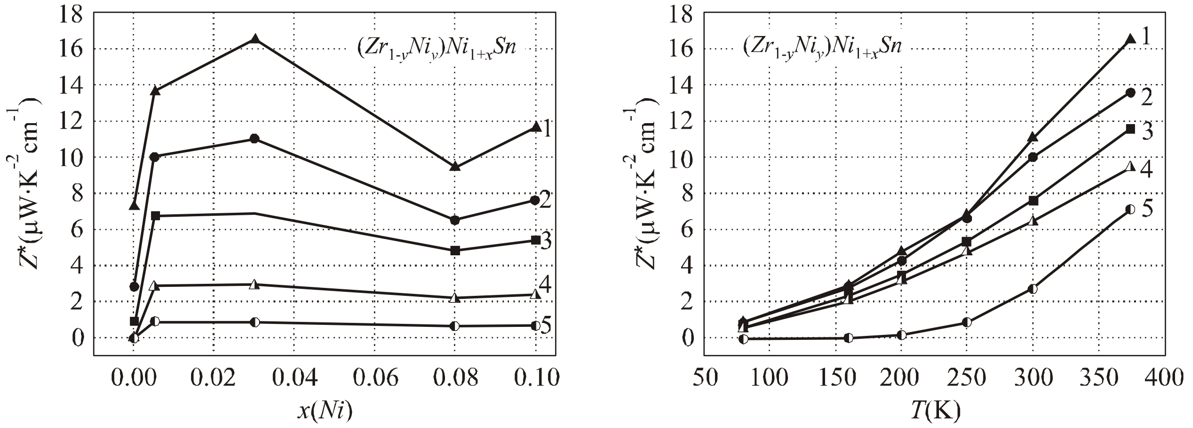

a) *b)*

Fig. 7. Changes in the values of thermoelectric power factor Z^* $(Zr_{1-y}Ni_y)Ni_{1+x}Sn$ with a change in composition (a): 1 – T = 375 K; 2 – T = 300 K; 3 – T = 250 K; 4 – T = 160 K; 5 – T = 80 K and temperature (b): 1 – x = 0.03; 2 – x = 0.005; 3 – x = 0.10; 4 – x = 0.08; 5 – x = 0.

Conclusions

As a result of integrated research on the crystalline structure, energy spectrum, electrokinetic and magnetic characteristics of intermetallic semiconductor *n-ZrNiSn* heavily doped with a donor impurity *Ni*, the effect of accumulation of excess Ni_{1+x} atoms in the tetrahedral voids of $(Zr_{1-y}Ni_y)Ni_{1+x}Sn$ structure up to concentrations $0 \leq x \leq 0.30$ has been revealed, and the donor nature of such structural defect has been established. The use of this effect for semiconductor doping is a new mechanism for parameter optimization of thermoelectric material based on *n-ZrNiSn*. It is shown that the obtained thermoelectric material $(Zr_{1-y}Ni_y)Ni_{1+x}Sn$ has high efficiency of thermal into electric energy conversion in the range of investigated temperatures.

The work was performed in the framework of grants of the National Academy of Sciences of Ukraine (№ 0106U000594) and Ministry of Education and Science, Youth and Sports of Ukraine (№ DR 0111U001088).

References

1. L.I. Anatychuk, *Thermoelements and Thermoelectric Devices [Handbook]* (Kyiv: Naukova Dumka, 1979), 768 p.
2. T.M. Tritt, Thermoelectric Materials, Phenomena, and Applications: A Bird's Eye View, *MRS Bulletin* **31**, 188 (2006).
3. S.R. Culp, S.J. Poon, N. Hickman, T.M. Tritt, and J. Blumm, Effect of Substitutions on the Thermoelectric Figure of Merit of Half-Heusler Phases at 800 °C, *Appl. Phys. Letters* **88** (16), 042106-1-3 (2006).
4. Y. Kawaharada, H. Uneda, H. Muta, K. Kurosaki, S. Yamanaka, High Temperature Thermoelectric Properties of *NiZrSn* Half-Heusler Compounds, *J. Alloys and Compounds* **364**, 59 (2004).
5. C. Uher, J. Yang, S. Hu, D.T. Morelli, and G.P. Meisner, Transport Properties of Pure and Doped *MNiSn* (*M = Zr, Hf*), *Phys. Rev. B* **59** (13), 8615 (1999).
6. V.A. Romaka, D. Fruchart, E.K. Hlil, P.E. Gladyshevsky, D. Gignoux, V.V. Romaka, B.S. Kuzhel, R.V. Krayovsky, Features of *n-ZrNiS*n Intermetallic Semiconductor Heavily Doped with Atoms of Rare-Earth Metals, *Semiconductors* **44** (3), 310 (2010).
7. B.I. Shklovsky, A.L. Efros, *Electronic Properties of Doped Semiconductors* (Moscow: Nauka, 1979), 416 p.
8. V.A. Romaka, V.V. Romaka, and Yu.V. Stadnyk, *Intermetallic Semiconductors: Properties and Appications* (Lviv: Lvivska Politekhnika, 2011), 488 p.
9. R. Ferro and A. Saccone, *Intermetallic Chemistry* (Amsterdam: Elsevier, 2008), 786 p.
10. V.A. Romaka, D. Fruchart, Yu.V. Stadnyk, J. Tobola, Yu.K. Horelenko, M.G. Shelyapina, L.P. Romaka, V.F. Chekurin, Conditions for the Attainment of Maximum Values of Thermoelectric Power Factor in the Intermetallic Semiconductors of *MgAgAs* Structural Type, *Semiconductors* **40** (11), 1309 (2006).
11. V.K. Pecharsky, P.U. Zavalij, *Fundamentals of Powder Diffraction and Structural Characterization of Materials* (New York: Springer, 2005), 713 p.
12. L.G. Akselrud, Yu.N. Grin, P.Yu. Zavalii, V.K. Pecharsky, V.S. Fundamenskii, CSD – Universal Program Package for Single Crystal or Powder Structure Data Treatment, *12 Eur. Crystallogr. Meeting Coll. Abstr., Vol. 3* (Moscow: Nauka, (1989), 155 p.
13. M. Schröter, H. Ebert, H. Akai, P. Entel, E. Hoffmann, G.G. Reddy, First-Principles Investigations of Atomic Disorder Effects on Magnetic and Structural Instabilities in Transition-Metal Alloys, *Phys. Rev. B* **52**, 188 (1995).
14. V.A. Romaka, Yu.V. Stadnyk, V.V. Romaka, D. Fruchart, YU.K. Horelenko, V.F. Chekurin, and A.M.Horyn, Conduction Peculiarities of *n-ZrNiSn* Intermetallic Semiconductor Heavily Doped with In Acceptor Impurity, *Semiconductors* **41** (9), 1059 (2007).

Submitted 23.10.2012.


E.I. Rogacheva

E.I. Rogacheva, O.S. Vodorez

National Technical University «Kharkiv Polytechnic
Institute», 21, Frunze Str., Kharkiv, 61002, Ukraine


O.S. Vodorez

PECULIARITIES OF THE CONCENTRATION DEPENDENCES OF STRUCTURAL AND THERMOELECTRIC PROPERTIES IN SOLID SOLUTIONS *PbTe-PbSe*

New experimental results and an overview of the results obtained earlier by the authors on the dependences of structure, mechanical, galvanomagnetic and thermoelectric properties on the composition of isovalent semiconductor solid solutions PbTe-PbSe in the range of small concentrations of PbSe (0 – 5 mol.%) as well as on the temperature dependences of galvanomagnetic properties (80 – 300 K) are presented. For the first time within the studied range of concentrations, an anomalous increase in electrical conductivity, charge carrier mobility and the exponent in the temperature dependence of charge carrier mobility under increasing PbSe content and an oscillatory behavior of the dependences of X-ray linewidth, microhardness, the Hall coefficient and the Seebeck coefficient on composition were registered. The observed effects are attributed to the existence of a percolation-type phase transition, presumably typical for all solid solutions, and to the self-organization processes occurring in solid solutions under the transition to the impurity continuum.

Key words: *PbTe-PbSe* solid solution, composition, heat treatment, percolation threshold, temperature dependence, microhardness, diffraction line width, electroconductivity, charge carrier mobility, Hall coefficient, Seebeck coefficient.

Introduction

The solid solution method proposed far back by academician A.F. Ioffe is still one of the main methods for improving the thermoelectric (TE) figure of merit Z of materials ($Z = S^2\sigma/\lambda$, where S is the Seebeck coefficient, σ is electric conductivity, λ is thermal conductivity) [1-3]. In so doing, it is generally supposed that increase in the concentration of introduced component is accompanied by a monotonous change in TE properties. However, in a number of solid solutions based on semiconductor compounds of the type IV-VI (*PbTe*, *SnTe*, *GeTe*) we have discovered a nonmonotonous character of concentration dependences of various properties in the region of low impurity content (see, for instance, [4-9]) and it was conjectured [10, 11] that the observed effect is typical of all solid solutions and is due to critical phenomena attending a transition from the dilute to concentrated solid solutions.

Recently, when investigating the concentration dependences of TE properties of *PbTe*-based solid solutions in $PbTe\text{-}Bi_2Te_3$ system we have discovered [12] another effect, namely an oscillatory behaviour of the composition dependences of properties, which we attributed to structural rearrangements occurring in a concentrated solid solution with increase in impurity content.

The importance of observed effects in terms of TE material science stimulates the expansion of the scope of investigated solid solutions and a more detailed study of the concentration dependences of properties. In particular, it is interesting to clear out whether the above effects will manifest themselves on composition-property dependences in case of isovalent and isostructural solid solutions. Such materials include solid solutions *PbTe-PbSe*, promising TE materials used in thermogenerators working in medium-temperature region (600 – 900 K) [2, 3]. Note that exactly this system was one of the first to demonstrate the efficiency of using the solid solution method for Z increase.

Binary compounds *PbTe* and *PbSe* are crystallized in the structure of *NaCl* type with the unit cell parameters $a = 0.645$ nm and $a = 0.612$ nm, respectively [13]. These are nonstoichiometric compounds with double-sided homogeneity areas with n-type conductivity at lead excess and p-type conductivity at chalcogen excess. The maxima on the liquidus and solidus curves in *Pb-Te* and *Pb-Se* systems do not coincide with the stoichiometric composition, being slightly displaced toward *Te* excess (50.002 at.%) or *Se* excess (50.005 at.%), which determines p-type conductivity of stoichiometric compositions *PbTe* and *PbSe* and undoped solid solutions *PbTe-PbSe* [13]. *PbTe* and *PbSe* have a complicated structure of valence band consisting of two overlapping subbands with different density of states [14].

PbTe and *PbSe* form a continuous series of isovalent and isotructural solid solutions with a minimum at 18 mol.% *PbSe* [13]. Depending on composition, the unit cell parameter changes in a linear fashion, with a slight negative deviation from linearity [13, 15], and microhardness grows as compared to the initial compounds, forming a curve with a maximum [16]. As far as we know, neither of the works dealing with the unit cell parameter and microhardness have studied alloys with *PbSe* content less than 5 mol.%. The energy gap of *PbTe-PbSe* alloys determined by self-absorption edge is a monotonous function of composition and almost linearly increases with increasing *PbSe* content [14, 15]. In [17], TE properties of solid solutions *PbTe-PbSe* of both n- and p-type were studied. Research on *Na*-doped *p-PbTe-PbSe* (0 – 15 mol.% *PbSe*) alloys has shown that the use of solid solutions allows reducing phonon thermal conductivity without major deterioration of electrical properties and that maximum value of Z ($Z = 2.0 \cdot 10^{-3}$ K^{-1}) exceeding by 30 % the value of Z for *p-PbTe* is achieved at 650 K for a solid solution with 5 mol.% *PbSe* and 0.7 at.% *Na*.

The existing works on TE properties of solid solutions *PbTe-PbSe* are mainly concerned with doped alloys of electron or hole types with different impurity concentration. In these works, the compositions and doping level optimal from the standpoint of practical applications, that is, with maximum Z values, are determined. However, to reveal the concentration anomalies of properties related to transition into heavy doping area, investigations should be conducted on the undoped stoichiometric solid solutions, where the role of impurity is played by the second component (in the case at hand it is selenium).

In [18-22] we reported on the results of measuring various properties of solid solutions *PbTe-PbSe* in the range of concentrations not exceeding 5 mol.% *PbSe*. It was established that isotherms of microhardness H, the Seebeck coefficient S, the Hall coefficient R_H, electric conductivity σ and the Hall mobility of charge carriers μ_H comprise anomalous parts on which a monotonous change of properties with composition is violated.

The purpose of this work is a more detailed additional study and analysis of the character of change in the structure and TE properties depending on the composition and temperature in the undoped polycrystalline solid solutions *PbTe-PbSe* in the range of compositions 0 – 5 mol.% *PbSe*. As long as in the manufacture of TE devices wide use is made of material pressing which allows increasing the strength and homogeneity degree of samples as compared to cast ones and generally followed by annealing, a question arises as to the relation between the characteristics of cast and pressed, annealed and unannealed samples of the same material.

Having analyzed the obtained results, we managed to reveal new effects taking place in solid solutions under study and governing the specific character of the composition and temperature dependences of TE properties.

Experimental procedure

Polycrystalline samples of *PbTe-PbSe* system (0 – 5 mol.% *PbSe*) were prepared by direct alloying of *Pb*, *Te* and *Se* elements of high degree of purity (99.999 % of basic component) in evacuated quartz ampoules at a temperature of 1250 ± 10 K for 6 hours with the use of vibratory agitation and subsequent annealing at a temperature of ~ 870 K for 250 hours (series 1). Some of the samples of series 1 were used to manufacture pressed samples at a temperature of 670 K and pressure 400 MPa (series 2), which after measurement were subject to homogenizing annealing in vacuum at 770 K for 260 hours (series 3). Besides, in the range of concentrations 0 – 2.5 mol.% *PbSe* the alloys were subject to additional heat treatment, namely after the synthesis the alloys were annealed at a higher temperature 1020 K for 200 hours (series 4). The alloys of each series were prepared simultaneously, so as to assure the identical conditions of their production. *X*-ray spectroscopy and chemical analysis methods were used to establish the homogeneity of samples. It was shown that a deviation of chemical composition from the assigned value did not exceed ± 0.02 at.%.

Microhardness was measured at room temperature on PMT-3 microhardness tester, using a diamond pyramid, under a constant load on the indentor $P = 0.49$ N. To establish the necessary load value, prior to measurement of *H,* dependences *H(P)* were studied in the range of $P = 0.03 – 0.49$ N, and it was shown that *H* is reduced with increase in *P* and is practically independent of load, starting from $P \sim 0.30$ N. As an example, Fig. 1 shows dependences *H*(*P*) for alloys of series 4. The time of loading, the time of exposure to load and the time of unloading were 10 s each. Device adjustment was performed using fresh chips of *NaCl* crystals. Surface preparation for measuring *H* (grinding, mechanical polishing and etching) was identical for all samples. Measuring *H* of each sample was performed at least at 30 points of a sample with subsequent statistical processing of results. Relative mean-square fluctuation for all samples did not exceed 3 %.

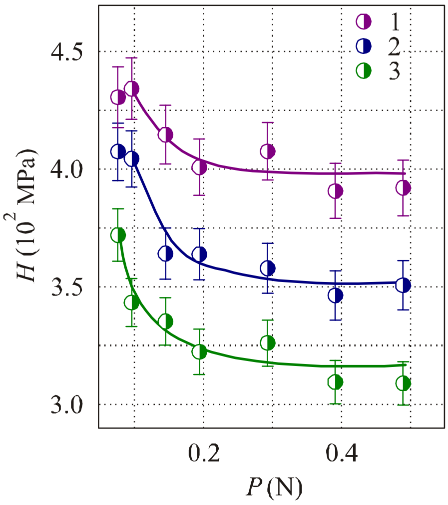

Fig. 1. Microhardness of solid solutions PbTe-PbSe versus the load on the indentor: 1 – PbTe, 2 – 1 mol.% PbSe, 3 – 1.5 mol.% PbSe.

The unit cell parameters *a* were determined on *X*-ray diffractometer DRON-2 with the Bragg-Brentano focusing geometry in filtered radiation of *X*-ray tube copper anode to an accuracy not lower than $\Delta a = 2 \cdot 10^{-4}$ nm.

The Hall coefficient R_H and electric conductivity σ were measured with the use of standard *dc* method in the range of temperatures from 80 to 300 K. The error of measuring R_H and σ did not exceed 5 %. The Hall mobility was calculated by the formula $\mu_H = \sigma \cdot R_H$. The Seebeck coefficient *S* was measured by compensation method according to copper electrodes at room temperature at no fewer than 20 sample points with subsequent statistical processing of measured data. The root mean square relative error for all samples did not exceed 3 %. All the samples, except for samples of series 3, were of *p*-type conductivity.

Discussion of the results

According to the results of microstructural and *X*-ray diffraction analyses, over the entire investigated range of compositions the alloys were single-phase and had crystalline structure of *NaCl* type. Fig. 2, a shows a dependence of the unit cell parameter on the composition of *PbTe-PbSe* alloys in the range of 0 – 5 mol.% *PbSe* for series 1 and 4 at room temperature. It is seen that for both series the points fall on one straight line which to a high accuracy corresponds to the Vegard line, confirming the fact of formation of a continuous series of solid solutions in the investigated range of concentrations.

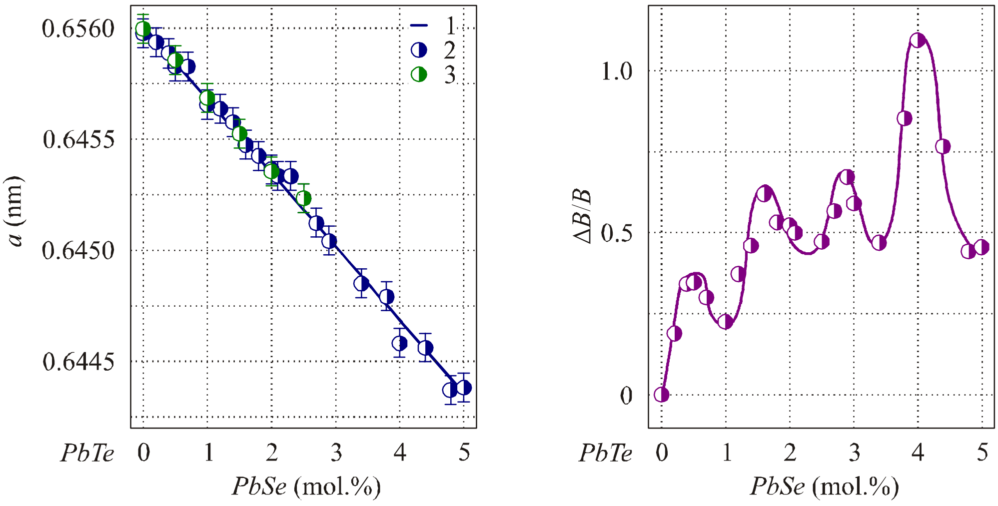

a) *b)*

Fig. 2. Dependence of unit cell parameter a (a) and a relative change in diffraction line width $(644)_\alpha+(820)_\alpha$ $\Delta B/B$ (b) on the composition of solid solution PbTe-PbSe for samples of series 1.
a) 1 – the Vegard curve; 2 – series 1; 3 – series 4.

Unlike the unit cell parameter, dependence of *X*-ray line width *B* on the composition of alloys is not monotonous. From Fig. 2, b it is evident that with a general tendency to growth of relative change in Δ*B/B* with increasing *PbSe* concentration, the dependence has a distinct oscillatory behaviour.

Fig. 3 shows dependences of *H* on the composition of *PbTe-PbSe* alloys prepared with the use of various techniques, and it is seen that neither of these dependences is monotonous, which was to be expected at formation of a perfect solid solution. On introduction of the first portions of *PbSe* (up to ~ 0.5 mol.%), the value of *H* for all series of samples is increased, pointing to crystal strengthening with introduction of Se impurity. However, with further increase in *PbSe* concentration, the behaviour of *H* – composition dependences is different for different series, though the general tendency to *H* increase within the entire concentration range (0 – 5 mol.% *PbSe*) is retained. Thus, for cast samples of series 1 in the range of compositions 0.5 – 1.25 mol.% *PbSe* there is a horizontal pad on the dependence; a similar pad is also observed for pressed unannealed samples (series 2), but its concentration range is somewhat expanded (0.5 – 1.75 mol.% *PbSe*). In so doing, for pressed samples there is a more considerable *H* increase in the range of 0 – 0.5 mol.% *PbSe* than for cast samples, though *H* values of series 1 and 2, achieved on the boundary of investigated composition range, are practically identical. Annealing of pressed samples in vacuum (series 3) leading to inversion of conductivity sign ($p \rightarrow n$) changes considerably the composition dependence of *H*: in the range of 0.5 – 2.5 mol.% *PbSe* on the isotherm of *H* there are distinct oscillations, following which *H* increases drastically when approaching the composition of 5 mol.% *PbSe* (Fig. 3, *c*). A similar oscillatory behaviour of *H* dependence is observed for cast samples subject to high-temperature annealing (series 4), that were prepared in the range of concentrations 0 – 2.5 mol.% *PbSe*. From Fig. 3, *d* it is seen that such oscillatory bahaviour of the composition dependence of *H* is also retained for series 4 with a change in the indentor load.

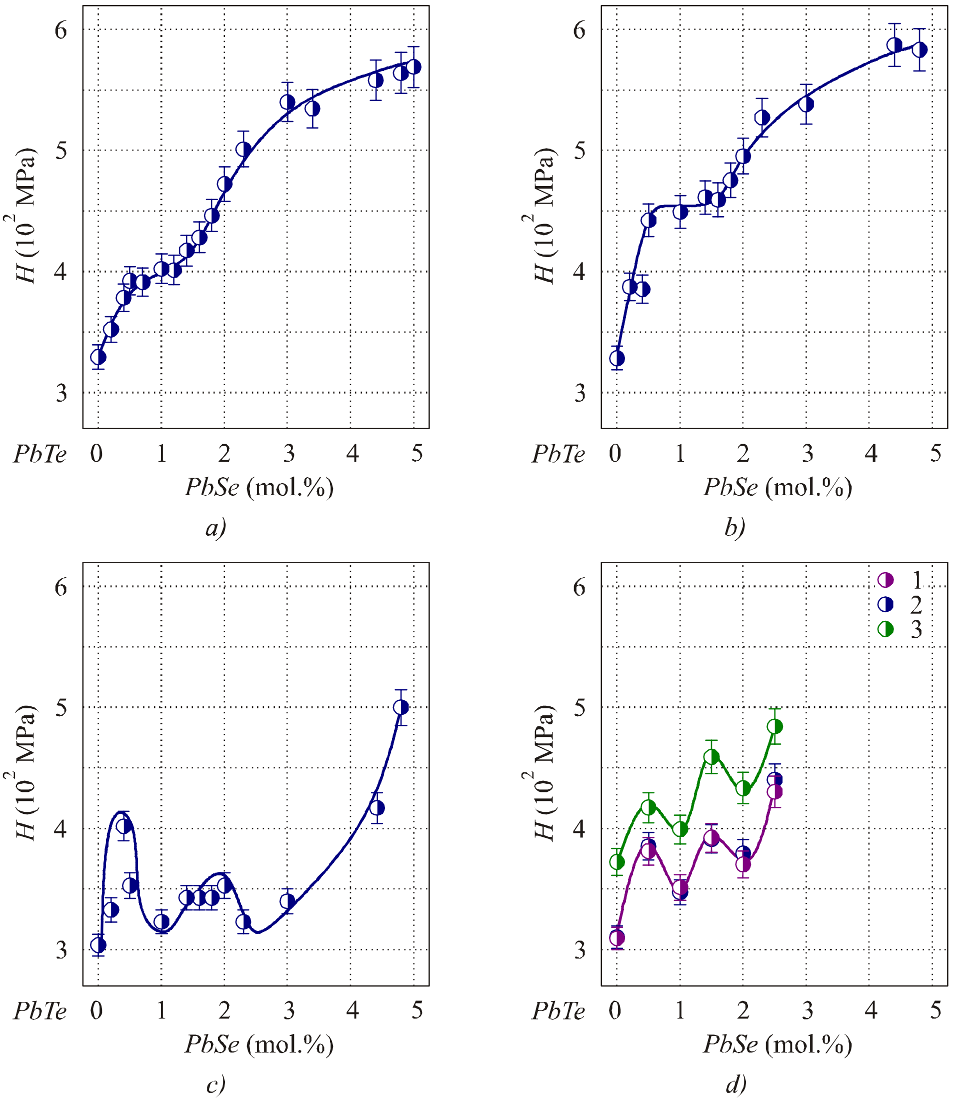

Fig. 3. Dependence of microhardness H on the composition of solid solution PbTe-PbSe for samples prepared by different methods: a) – series 1; b) – series 2; c) – series 3 and d) – series 4: 1 – 0.049 N, 2 – 0.39 N, 3 – 0.49 N.

Thus, irrespective of sample preparation technique (cast or preseed) and heat treatment, introduction of up to 0.5 mol.% *PbSe* leads to a drastic increase of *H*. The effect of solid-solution hardening on the introduction of impurities related to blocking of dislocations by impurity atoms is well known [23]. However, demands explanation the fact that starting from ~ 0.5 mol.% *PbSe*, for all series there is a qualitative change in dependence, namely the appearance of plateaus or oscillations.

Studies on the kinetic properties at room temperature have proved the existence of concentration anomalies in solid solutions *PbTe-PbSe*. From Fig. 4, *a* and *b*, showing dependences of σ and μ_H on composition for cast polycrystalline samples of series 1, one can see that these dependences have a behaviour uncommon for solid solutions: after a drop in said parameters with increase in *PbSe* concentration to 0.5 – 0.75 mol.% there is a drastic (more than 100 %) growth of σ and μ_H over a sufficiently narrow concentration range, following which σ and μ_H again drop with increase in *PbSe* content to 5.0 mol.%. The parts of σ and μ_H drop with a growth in *PbSe* concentration can be adequately explained, since with introduction to crystal of impurity atoms the mobility of charge carriers is generally reduced due to increased imperfection of crystal lattice and the emergence of additional centres of charge carrier scattering, but growth of σ and μ_H from this standpoint is anomalous.

Even more complicated composition dependence is observed for the Hall and Seebeck coefficients (Fig. 4, *c*, *d*): up to ~ 2.5 mol.% *PbSe*, despite the general tendency to reduction of R_H and S with a growth in concentration *PbSe*, parts of drop in R_H and S interchange with parts of growth, owing to which the composition dependence of R_H and S exhibits a distinct oscillatory behaviour.

The nonmonotonous behaviour of kinetic coefficients is also responsible for a complicated dependence of TE power $P = S^2\sigma$ on the composition (Fig. 4, *e*).

Research on the effect of pressing on the values of S, σ and μ_H of polycrystals of solid solutions *PbTe-PbSe* in the range of concentrations 0 – 5.0 mol.% *PbSe* at room temperature performed in [21] has shown that in pressed samples the values of S remain almost unchanged, and σ and μ_H are reduced as compared to cast samples. Annealing of pressed samples leads to a reversal of hole to electron conductivity type, growth of σ and μ_H. However, concentration anomalies of properties in the range of compositions 0.5 – 2.5 mol.% *PbSe*, observed in cast samples and presumably related to a transition to impurity continuum also occur in pressed samples, confirming the fact of existence of percolation-type concentration phase transition.

Fig. 5 shows the temperature dependences of σ, μ_H and R_H for samples of series 1 of various composition. All the samples have *p*- conductivity over the entire investigated range of temperatures and compositions. For samples of all compositions a rise in temperature leads to a monotonous decrease in σ and μ_H and a slight increase in R_H. Unlike other lead chalcogenides, where, as a rule, $R_H(T)$ dependence in the range from helium to room temperature and higher is very weak, in *p-PbTe* at higher than 150 K there is a marked growth of R_H. Such R_H behaviour in *p-PbTe* is attributable to the influence of the second valence band characterized by larger effective mass and located below the edge of light holes at the distance of order 0.1 eV. Due to a low mobility and a larger effective mass of holes in the second valence band, their contribution to the Hall effect is relatively small, and as the holes go over to the second band, with a rise in temperature, the effective concentration of charge carriers is decreased, and R_H is increased. Taking into consideration the presence of light and heavy holes, the expression for R_H can be written as follows:

$$R_H = \frac{r}{e}\frac{p_1\mu_1 + p_2\,\mu_2}{(p_1\mu_1 + p_2\,\mu_2)^2} = \frac{r}{ep_1}\frac{1+\gamma f^2}{(1+\gamma f)^2}, \tag{1}$$

where p_1 and p_2 are concentrations of light and heavy holes, respectively, the sum of which does not depend on temperature and is equal to the number of acceptors, μ_1 and μ_2 are their mobilities, $\gamma = p_1/p_2$, $f = \mu_1/\mu_2$, r is Hall-factor depending on the degeneracy degree and the mechanism of charge carrier scattering. From formula (1) it follows that as the contribution of heavy holes increases with a rise in temperature, R_H increases as well. As is evident from Fig. 5, *a*, *b*, *c*, a similar effect occurs in solid solutions *PbTe-PbSe*, whose valence band structure is identical to that of lead telluride.

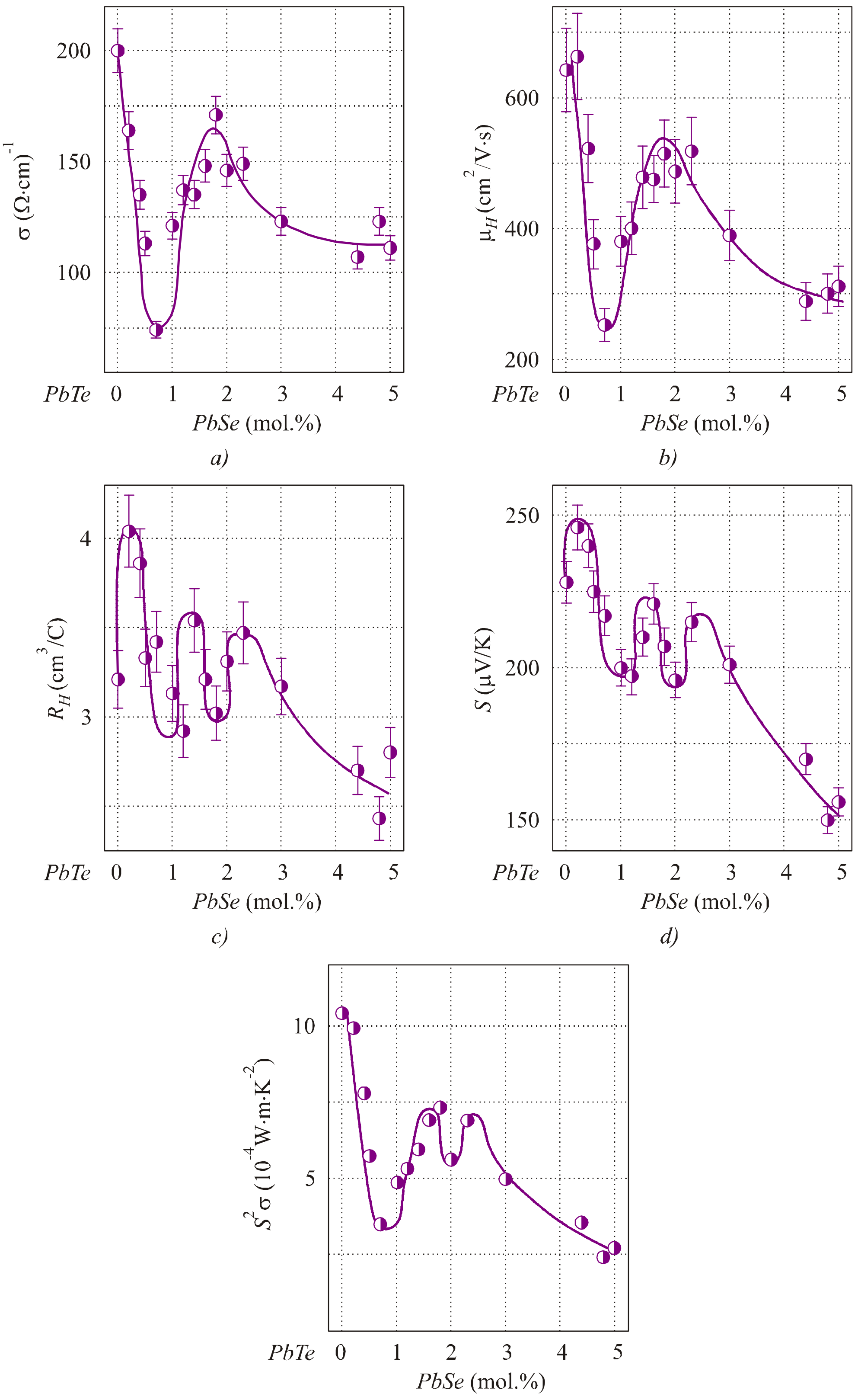

a) *b)*

c) *d)*

e)

Fig. 4. Dependence of electric conductivity σ (a), Hall mobility of charge carriers μ_H (b), Hall coefficient R_H (c), Seebeck coefficient S (d) and thermoelectric power $P = S^2\sigma$ (e) on the composition of solid solutions PbTe-PbSe for samples of series 1.

Of interest is the composition dependence of exponent ν in the temperature dependence of charge carriers mobility $\mu_H \sim T^{\nu}$ (Fig. 5, *d*), which, as the other characteristics, has a nonmonotonous behaviour. With a general tendency to drop of ν with increasing *PbSe* content, the curve has an anomalous part of exponent growth, which is additional proof of a complicated concentration dependence of properties in a solid solution *PbTe-PbSe*.

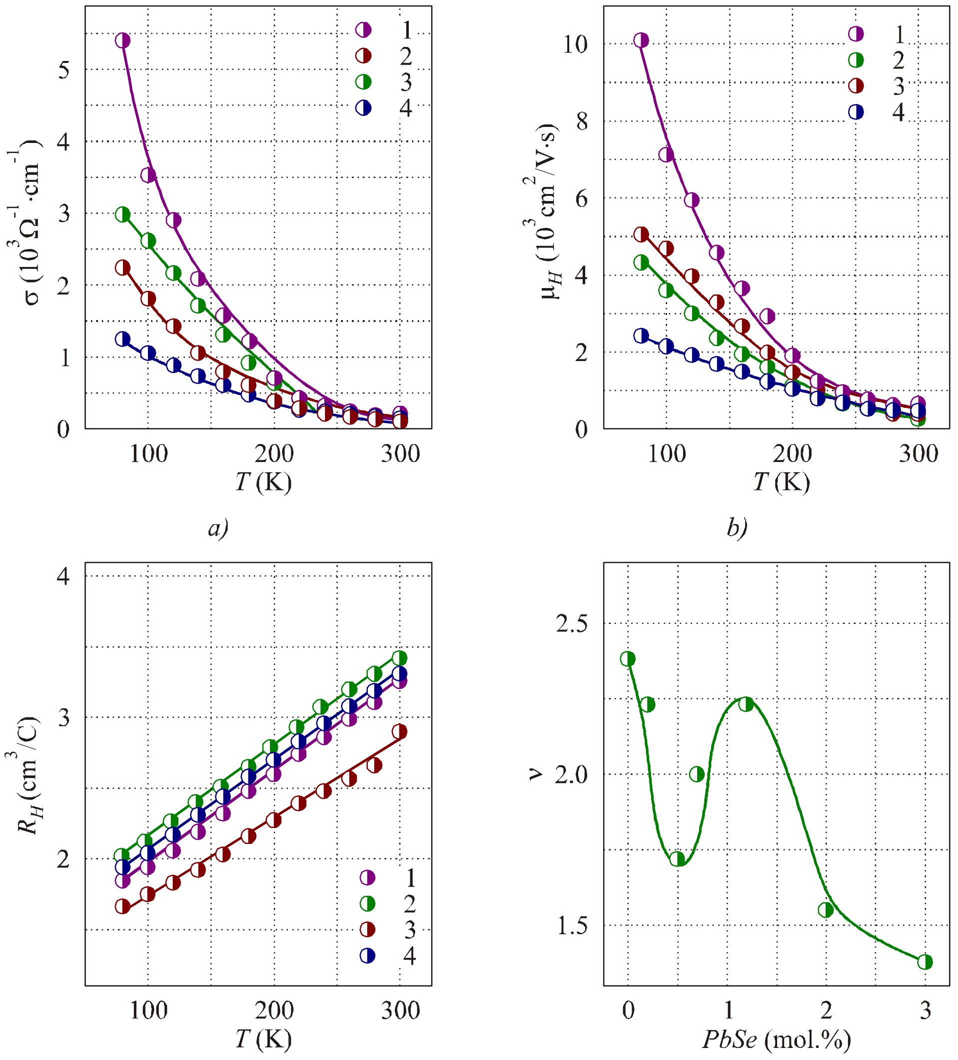

a) *b)*

c) *d)*

Fig. 5. Temperature dependences of electric conductivity σ (a), Hall mobility of charge carriers μ_H (b), Hall coefficient R_H (c) and exponent ν in the temperature dependence $\mu_H = A \cdot T^{\nu}$(d) 1 – PbTe; 2 – 0.7 mol.% PbSe; 3 – 1.2 mol.% PbSe; 4 – 2.0 mol. % PbSe.

For a qualitative explanation of a change in the composition dependence of properties, observed for all properties, starting from ~ 0.5 mol.% *PbSe*, one can use the concepts of percolation theory, as we did it for other semiconductor solid solutions [4-11]. It is supposed that in any solid solution, irrespective of the character of impurity interaction, there exists a critical concentration x_C – “percolation threshold”, whereby a continuous chain of interactions between impurity atoms is formed (“infinite cluster” in terms of percolation theory) [24]. As long as percolation transition refers to second-order phase transitions, it must be attended with critical phenomena, that is, a drastic change in properties. Using percolation theory approximation, it can be assumed that the onset of anomalous portions corresponds to reaching percolation threshold x_C, and in the concentration ranges corresponding to anomalous change of properties the density of infinite cluster is increased. On completion of the latter process, crystal goes over into a new state, i.e. impurity continuum, when impurity atoms become interconnected and their interaction acquires a cooperative nature. We think that exactly percolation threshold might serve the boundary that separates dilute solid solutions from concentrated ones. Of course, in the general case for various properties defined by various interaction types (deformation, Coulomb, dipole-dipole, etc), the values of percolation thresholds x_C for the same system can be different. However, in *PbTe-PbSe* system under investigation these values almost coincide – the anomalies start from ~ 0.5 – 0.75 mol.% *PbSe*.

Let us consider as an example such property as microhardness. It is known that the basic mechanism of solid-state hardening is related to elastic interaction of dislocation fields and impurity atoms, as a result of which the dislocation mobility is reduced, hence, strength characteristics, such as yield strength, microhardness, etc., increase. As long as marked displacements of atoms are created at the distance of one or two atomic spacings, one can consider the field of elastic deformations to be short-range and speak of a typical radius of deformation interaction r_0. With low impurity concentrations (in this case *Se* atoms), when the distance between them is much larger than r_0, the fields of elastic deformations created by individual impurity atoms are isolated from each other, almost not overlapped and make an additive contribution to *H* value. This results in *H* growth with increasing impurity concentration, which is observed in the range to ~ 0.5 mol.% *PbSe*.

With further increase in impurity atoms content for samples of series 1 and 2 on the isotherm of *H* there appear plateau in the range of 0.5 – 1.25 and 0.5 – 1.75 mol.% *PbSe*, respectively, and for samples of series 3 and 4 this dependence acquires oscillatory behaviour in the range of compositions 0 – 2.5 mol.% *PbSe*. This fact testifies to the presence of concentration phase transition which in the general case can be due to solid solution decomposition or rearrangement of crystal or electronic structure. The assumption of possible decomposition or change in crystal structure contradicts the results of *X*-ray structural analysis. The presence of anomalies on the curve *H* – composition points to a change in dislocation motion pattern, owing to which the dislocation motion grows and crystal softening occurs. This can be explained as follows. With increasing impurity concentration, the fields of elastic deformations start to be overlapped, leading to partial stress relief in a crystal. As long as impurity atoms are distributed in crystal lattice nonuniformly, some deformation spheres are overelapped, and the others – not, and portions with reduced stresses are formed in a crystal, which up to a certain concentration of impurity atoms are not interrelated. However, when concentration of impurity atoms becomes such that a continuous chain is formed, penetrating the entire crystal and interrelating impurity atoms through their deformation fields, the character of concentration dependence *H* should change, since dislocation motion pattern will change under the effect of applied load. As long as overlapping of deformation fields of two neighbouring atoms results in partial compensation of elastic stresses of opposite sign, formation of percolation channels will be matched by a drastic increase in dislocation mobility, hence, a decrease in *H*. The specific mechanism of collective effect of impurities on crystal plastic properties, which is a function of many factors and governs crystal softening, is not known so far and calls for special consideration. After crystal goes over into a qualitatively new state, related to formation of “impurity condensate”, new centres appear which impede the dislocation motion, and *H* grows again.

As can be seen from Fig. 3, the character of *H* dependence on composition and the character of concentration anomaly in this area is affected by sample fabrication technique (cast or pressed), the presence or absence of annealing, as well as annealing temperature. It is quite natural to be expected, since the degree of phase transition smearing, the character of properties change with phase transition are essentially dependent on the defective structure of crystal, its homogeneity, kinetic factors which, in turn, are largely determined by thermal treatment. It can be supposed that with a rise in annealing temperature of cast samples from 870 to 1020 K and with annealing of pressed samples, firstly, higher homogenization degrees are achieved than for samples of series 1 and 2, and, secondly, the number of interstitial atoms is increased, which for series 4, possibly, become predominant point defects, taking into consideration that annealing of pressed samples is followed by inversion of conductivity type, caused, apparently, by slight losses of chalcogen at annealing. Microscopic mechanisms leading to oscillatory behaviour of *H* with composition in the intermediate range of compositions corresponding to transition from dilute to concentrated solid solutions are as yet unknown, but it is clear that considerable role in the manifestation of concentration anomalies is played by self-organization processes (when *H* drops), alternating with defect accumulation processes (when *H* increases). This assumption is supported by the presence of oscillatory concentration dependence of *X*-ray linewidth $(644)_\alpha + (820)_\alpha$ (Fig. 2, *b*). It is known that the main factors causing *X*-ray lines widening include fluctuations of atomic spacings due to microstresses and small size of coherent scattering areas [25]. In homogeneous solid solutions widening can be caused by disorder in the distribution of atoms of different sort and statistical displacements of atoms surrounding impurity atom relative to their position in a perfect crystal. So, widening of lines on introducing the first portions of impurity atoms can be readily explained. As long as all the samples were prepared by the same procedure, and *X*-ray study was identical, the change in $\Delta B/B$ with a variation of impurity atoms concentration can be due to internal structural changes caused by disorder in the distribution of impurity atoms and the microstresses they caused. When impurity concentration reaches x_C, the lattice stresses are partially relieved and dependence behaviour is changed.

The observed anomalous growth of σ and μ_H also testifies to qualitative changes of solid solution properties with a variation of impurity content. We observed similar concentration anomalies of σ and μ_H in the investigation of other solid solutions (*PbTe-MnTe* [7], *PbTe-GeTe* [9] etc.) and also attributed them to critical phenomena attending concentration phase transitions.

Considering these critical phenomena within the percolation theory [24], one can estimate the radius of impurity atom domain r_o, using equation for problem of spheres:

$$\frac{4\pi}{3} \cdot N_c \left(2r_0\right)^3 \approx 2.7, \tag{2}$$

where N_c is the average number of sphere centres in unit volume corresponding to percolation threshold. Such estimate for solid solutions *PbTe-PbSe* yields the value $r_o \approx 1.5\ a_0$ (a_0 is parameter of unit cell *PbTe*), which is in good agreement with the short-range character of impurity potential in compounds IV-VI [14].

Oscillatory behaviour of dependences of R_H, *S*, *H* and $\Delta B/B$ on composition with *PbSe* content less than ~ 2.5 – 3.0 mol.% shows that the system passes through a number of intermediate states with very close compositions, but different character of space correlations. Such behaviour can testify that, under certain concentrations of impurity components, self-organization processes interchange with defect accumulation processes in the ordered medium. We observed a similar situation in $PbTe\text{-}Bi_2Te_3$ system in the composition range up to ~ 3 mol.% Bi_2Te_3, namely concentration dependences of σ, R_H, μ_H, as well as $\Delta B/B$ were of oscillatory nature [12]. And this situation is not unique. There are well known nonstoichiometric phases of variable composition where homogeneity area is divided into a number of subareas with different type of long-range or short-range ordering and very close compositions.

The initial growth of R_H on the introduction of the first portions of *PbSe* – up to 0.2 mol.%

(Fig. 4, *e*) can be related to a complex mechanism of defects formation occurring in this case. The point is that with a small content of impurity atoms a change in free energy is caused mainly by entropy member, and the probability of processes related to configuration entropy growth is increased, stimulating such phenomena as delocalization of impurity atoms with respect to the main structural positions (for instance, their introduction to interstitial sites), formation of new defect types, etc. On introducing selenium impurity atoms into interstitial sites of anion sublattice, chalcogen atoms create equivalent number of once ionized vacancies exhibiting donor properties. Moreover, it should be taken into account that on introducing the first portions of impurity atoms, because of a change in the thermodynamic equilibrium conditions in a doped crystal there can be a change in the equilibrium concentration of nonstoichiometric cation vacancies possessing acceptor properties, leading to a reduction of hole concentration and, respectively, to growth of R_H. Subsequent reduction of R_H with increasing content of *PbSe* to ~ 0.75 mol.% is in good agreement with the reduction of the Seebeck coefficient (Fig. 4, *e*).

Processes of impurity atoms redistribution with increase in impurity concentration can include: 1) formation of superstructure with a periodic distribution of impurity atoms in the structure of basic material; 2) formation of structure with short-range ordering extending to one or several coordination spheres; 3) change in the character of impurity atoms localization; 4) formation of clusters whose structure is different from the structure of basic material.

A qualitative change in properties can be expected, when with increasing concentration of doping component the average distances between impurity atoms achieve the values whereby their interaction covers the entire crystal, stimulating self-organization processes leading to a reduction of the internal crystal energy and assuring solid solution stabilization. It can be assumed that formation of percolation channels through *Se* impurity atoms on achievement of percolation threshold stimulates self-organization processes or is attended with them. Note that the value $r_0 \approx 1.5\ a_0$ corresponds to close packing of impurity spheres with formation of face-centered cubic lattice with unit cell parameter $a = 4\ a_0$.

In heterovalent nonisotructural solid solutions between two chemical compounds after formation of “impurity continuum” there is high chance of short-range ordering of solid solution with formation in the initial compound of complexes with crystal structure different from die structure and corresponding to second component structure. As regards isovalent and isotructural solid solutions, including *PbTe-PbSe* solution, here the probability of long-range ordering is higher.

Thus, the results of this work provide another evidence of the universal character of critical phenomena attending a transition from weak doping to formation of impurity continuum and governing a complicated character of the concentration dependences of properties. Irrespective of the character of interaction between impurity atoms, crystal properties are fundamentally changed, when a continuous chain of interactions between impurity atoms is formed and the velocity of distribution of elementary excitations is varied. Moreover, the results obtained imply that the emergence of percolation channels in a solid solution initiates self-organization processes in a solid solution leading to complex concentration dependences of properties.

Conclusions

Dependences of structural, mechanical, galvanomagnetic and thermoelectric properties on the composition of isovalent and isostructural solid solutions *PbTe-PbSe* in the range of concentrations 0 – 5 mol.% *PbSe* exhibit a distinct nonmonotonous character. The observed concentration anomalies are proved by the fact of existence of percolation-type phase transition within any solid solution and testify to a complicated character of isotherms of properties in the transition area of concentrations between the dilute and concentrated solid solutions close to percolation area.

The obtained results should be taken into account in the investigation and interpretation of properties of solid solutions *PbTe-PbSe*, at their further doping for the purpose of optimization of thermoelectric parameters, as well as in the development of new thermoelectric materials based on lead telluride and other materials, as long as the discovered effects are, apparently, of a general nature.

The authors are grateful to student E. Martynova for the assistance in the work.

References

1. L.I. Anatychuk, *Thermoelements and Thermoelectric Devices: Reference Book* (Kyiv: Naukova Dumka Publishers, 1979), 768 p. [in Russian].
2. *CRC Handbook of Thermoelectrics*. Ed. Rowe D.M. (CRC Press, Boca Raton, London, New York, Washington, D.C., 1995), 701 p.
3. A.F. Ioffe, S.V. Airapetyants, A.V. Ioffe, N.V. Kolomoyets, and L.S. Stilbance, On the Improved Efficiency of Semiconductor Thermocouples, *Doklady AN SSSR* **106**, 981 – 982 (1956).
4. E.I. Rogacheva, N.K. Zhigareva, and A.B. Ivanova, *PbTe*-based Solid Solutions in the System *PbTe-CdTe*, *Izv. AN SSSR. Neorgan. Mater* **24**, 1394 – 1397 (1988).
5. E.I. Rogacheva, Concentration-Dependent Microhardness in Semiconductor Solid Solutions, *Izv. AN SSSR. Neorgan. Mater*. **25**, 643 – 646 (1989).
6. E.I. Rogacheva, A.S. Sologubenko, I.M. Krivulkin, Microhardness of $Pb_{1-x}Mn_xTe$ Semimagnetic Solid Solutions, *Inorganic Materials* **34,** 545 – 549 (1998).
7. E.I. Rogacheva and I.M. Krivulkin, The Temperature and Concentration Dependences of the Charge Carrier Mobility in *PbTe-MnTe* Solid Solutions, *Semiconductors* **36**, 966 – 970 (2002).
8. E.I. Rogacheva, O.N. Nashchekina, and M.S. Dresselhaus, Thermal Conductivity Isotherm Anomalies in Semiconductor Solid Solutions Based on IV-VI Compounds, *J. Thermoelectricity* **4**, 82 – 92 (2005).
9. E.I. Rogacheva, N.A. Sinelnik, and O.N. Nashchekina, Concentration Anomalies of Properties in $Pb_{(1-x)}Ge_{(x)}Te$ Solid Solutions, *Acta Phys. Polonica (A)* **84**, 729 – 732 (1993).
10. E.I. Rogacheva, Percolation Effects and Thermoelectric Materials Science, *J. Thermoelectricity* **2**, 61 – 72 (2007).
11. E.I. Rogacheva, Critical Phenomena in Heavily-Doped Semiconducting Compounds, *Jpn. J. Appl. Phys*. **32**, 775 – 777 (1993).
12. E.I. Rogacheva, O.S. Vodorez, and O.N. Nashchekina, Oscillations of Transport Properties in $PbTe\text{-}Bi_2Te_3$ Solid Solutions, *J. Phys. Chem. Solids* **74**, 35 – 39 (2013).
13. N.Kh. Abrikosov and L.E. Shelimova, *Semiconducting Materials Based on* A^4B^6 *Compounds* (Moscow: Nauka, 1975), 195 p. [in Russian].
14. Yu.I. Ravich, B.A. Yefimova, and I.A. Smirnov, *Semiconductor Investigation Methods as Applied to Lead Chalcogenides PbTe, PbSe and PbS* (Moscow: Nauka, 1968), 384 p.
15. A. Gangulee, On the Solid Solutions of the Quasibinary System *PbTe-PbSe*, *Trans. Metallurg Soc. AIME* **245**, 1830 – 1840 (1969).
16. M.S. Darrow, Micro-Indentation Hardness Variation as a Function of Composition for Polycrystalline Solutions in the Systems *PbS*/*PbTe*, *PbSe*/*PbTe*, and *PbS*/*PbSe*, *J. Mater. Sci.* **4**, 313 – 319 (1969).

17. I. Kudman, Thermoelectric Properties of *p*-type *PbTe-PbSe* Alloys, *J. Mater. Sci.* **7**, 1027 – 1029 (1972).
18. O.S. Vodoriz, O.I. Rogacheva, Mechanical Properties of Solid Solutions *PbTe-PbSe*, *Visnyk (Herald) of Lviv University. Physics series* **42**, 64 – 67 (2008).
19. O.S. Vodorez, A.A. Mesechko, V.I. Pinegin, and E.I. Rogacheva, Anomalous Change of the Seebeck Coefficient in Lead Telluride with Heavy Selenium Doping, *New Technologies* **2** (20), 118 – 124 (2008).
20. O.S. Vodorez, E.I. Rogacheva, Isotherms of the Hall Coefficient of Solid Solutions $PbTe_{1-x}Se_x$, *Metal Physics and Advanced Technologies* **30**, 47 – 55(2008).
21. O.S. Vodorez, E.I. Rogacheva, Effect of Pressing on the Properties of *PbTe-PbSe* Solid Solutions, *Scientific Herald of Uzhgorod University. Physics Series* **24**, 217 – 221 (2009).
22. E.I. Rogacheva, O.N. Nashchekina, and O.S. Vodorez, Enhancement in Charge Carrier Mobility under Transition to Heavy Doping, PHYSICS OF SEMICONDUCTORS: 29th International Conference on the Physics of Semiconductors. *AIP Conference Proceedings* **1199**, 83 – 84 (2009).
23. T. Suzuki, H. Yoshinaga, and S. Takeuchi, *Dislocation Dynamics and Plasticity* (Moscow: Mir, 1989), 78 p.
24. D. Stauffer and A. Aharony, *Introduction to Percolation Theory* (Washington, DC: Taylor & Francis, 1992), 127 p.
25. Ya.S. Umanskii, *X-Ray Study of Metals and Semiconductors* (Moscow: Metalurgiya, 1969), 38 p.

Submitted 09.04.2013.

L.M. Vikhor, V.Ya. Mykhailovsky, V.R. Bilinsky-Slotylo

Institute of Thermoelectricity NAS and MES of Ukraine,
1, Nauky Str., Chernivtsi, 58029, Ukraine

SEGMENTED AND MULTI-STAGE STRUCTURES BASED ON $PbTe/Zn_4Sb_3$ FOR THERMOELECTRIC GENERATOR MODULES

This paper presents the results of designing segmented thermoelectric modules, as well as functionally graded material (FGM)-based modules and multi-stage structures of $PbTe/Zn_4Sb_3$*-based materials for use in thermoelectric power converters with the hot side temperature level 780 K.*

Key words: generator modules, heat recovery, power converters.

Introduction

Among thermoelectric materials used for creation of generator modules for the hot side temperature level 775-875K, *PbTe* is traditionally employed [1]. At current stage of development of science and technology, the presence of lead and tellurium in this material is not a limiting factor for its mass use, in particular, for the recovery of waste heat from vehicles, industry, etc. However, unlike *n-PbTe*, *p*-type has a low mechanical strength and unstable parameters, especially at elevated temperatures [2]. Most frequently an alternative to *p-PbTe* is *GeTe-AgSbTe* [3-5], however, taking into account the world reserves and the cost of source elements listed in Table 1 [6], the use of *Ag*, *Ge* and *Te* as the basic components for creation of thermoelectric power converters should be restricted.

Table 1

The cost, production outputs and world reserves of components used for creation of medium-temperature thermoelectric materials [6]

Material / Characteristics	*Pb*	*Te*	*Ag*	*Ge*	*Sb*	*Zn*
Price (2011), $/kg	2.73	360	1109	1400	15.1	2.34
Production (2011),1000 t	4.5	0.12	23.8	118	169	12.4
World reserves, 1000 t	85	24	530	> 500	1800	250

Within recent years a number of researchers have obtained a series of thermoelectric materials with potentially high operating characteristics [7-10]. Among them, good promise is shown by β-Zn_4Sb_3 that has a high figure of merit ($ZT = 1.2 – 1.4$ at 675 K) with a rather low prime cost. The above factors prove the possibility of using β-Zn_4Sb_3 material as a *p*-type leg for medium-temperature thermoelectric modules.

The purpose of this work is to design and evaluate the efficiency of segmented, multi-stage and FGM modules based on $PbTe/Zn_4Sb_3$, as well as to optimize such structures for achieving maximum module efficiency.

Design of segmented thermoelectric modules and FGM modules

Calculation and design of modules was done with the use of optimal control theory methods [11] and experimentally measured concentration-temperature dependences of α, σ, κ parameters of *n*-type *PbTe* samples doped with iodine [12] and europium [13], as well as *p*-type samples of $Zn_{3.96+x}Cd_{0.04}Sb_3$ [14] and $(Zn_{1-x}Cd_x)_4Sb_3$ [15]. Such dependences for the best samples with different doping level, different composition and, respectively, different current carrier concentration are given in Figs. 1 and 2.

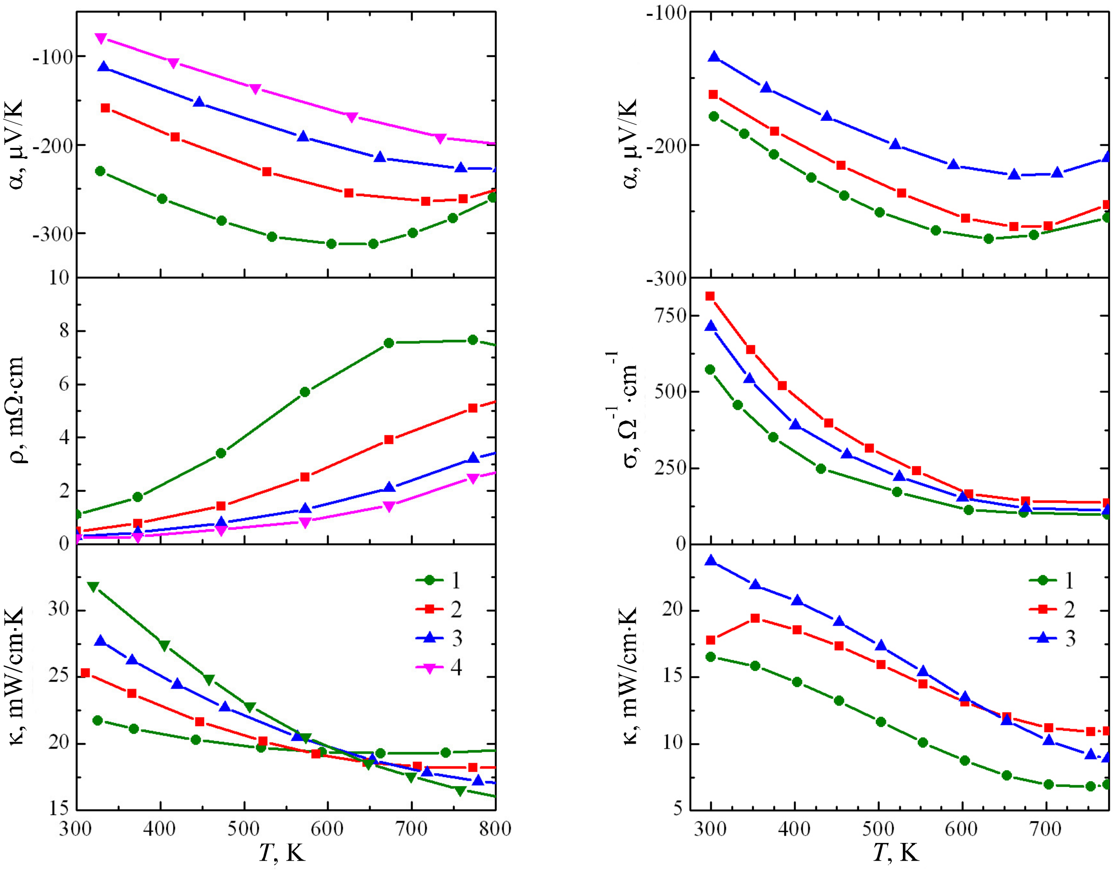

a) *b)*

Fig. 1. Temperature dependences of thermoelectric parameters of PbTe-based n-type materials:
a) PbTe+x mol.% PbI_2 (1 – x = 0.01; 2 – x = 0.03; 3 – x = 0.055; 4 – x = 0.1) [12];
b) PbTe+x % Eu (1 – x = 1; 2 – x = 2; 3 – x = 3) [13].

The temperature dependences shown in Figs.1 and 2 were approximated by two-dimensional polynomials in the form of $\alpha^{n,p} = \alpha^{n,p}(\sigma_0^{n,p}, T)$, $\sigma^{n,p} = \sigma^{n,p}(\sigma_0^{n,p}, T)$, $\kappa^{n,p} = \kappa^{n,p}(\sigma_0^{n,p}, T)$. Polynomial coefficients were introduced into computer program as input data for the design of thermoelectric modules. Designations of module legs of such materials are given in Table 2.

Calculated in maximum efficiency mode, optimal energy characteristics (current *I*, voltage *U*, power *P*, efficiency η) of one- and two-segment modules, as well as FGM modules comprising 32 thermoelements (the height of legs 5.6 mm, the cross-sectional area of legs 4×4 mm^2) are given in Table 3. The values of contact resistances in the calculations were assumed to be equal to $5 \cdot 10^{-5}$ $\Omega \cdot$cm^2. Optimization was performed by determination of such impurity concentrations in each segment material whereby thermoelement efficiency reaches a maximum with regard to optimal current densities in its legs and the height of segments.

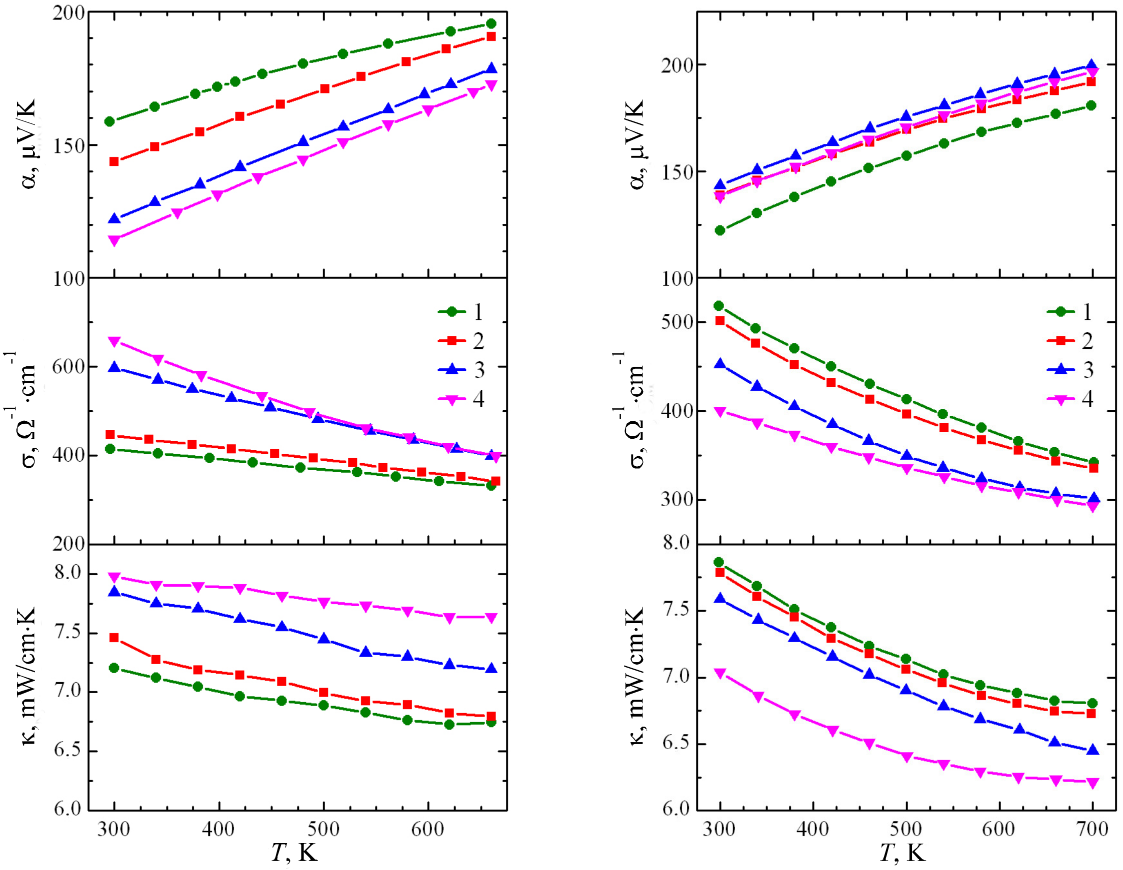

a) *b)*

Fig. 2. Temperature dependences of thermoelectric parameters of Zn-Sb-based p-type materials:
a) $Zn_{3.96+x}Cd_{0.04}Sb_3$ (1 – x = –0.05; 2 – x = 0; 3 – x = 0.05; 4 – x = 0.1) [14];
b) $(Zn_{1-x}Cd_x)_4Sb_3$ (1 – x = 0; 2 – x = 0.005; 3 – x = 0.01; 4 – x = 0.015) [15].

Table 2

Leg designations of generator modules of $PbTe/Zn_4Sb_3$-based thermoelectric materials

Designation	*n*-type leg	Designation	*p*-type leg
S1	*PbTe*<*x* mol.% PbI_2> ($x = 0.01 – 0.1$) [12]	S2	$Zn_{3.96+x}Cd_{0.04}Sb_3$ ($x = –0.05 – 0.1$) [14]
S3	*PbTe*<*x* % *Eu*> ($x = 1 – 3$) [13]	S4	$(Zn_{1-x}Cd_x)_4Sb_3$ ($x = 0 – 0.015$) [15]

Analysis of resulting data shows that one-segment modules S1-S2 and S1-S4 have commensurate efficiencies ($\eta \approx 7.5 – 7.6\%$). However, with transition to two segments, the efficiency of S1-S2 is $\eta = 14.65$ %, whereas the efficiency of module S1-S4 is considerably lower $\eta = 12.25$ %. Similar results were obtained for modules S3-S2 and S3-S4. With the use of europium-doped *PbTe* (S3) as *n*-type leg, the efficiency of one-segment modules is reduced ($\eta \approx 6$ %), and that of two-segment modules remains practically the same as in the case when iodine-doped lead telluride (S1) is selected as *n*-type leg.

Table 3

Characteristics of generator modules of PbTe/Zn_4Sb_3-based materials for the operating temperature range of 323 – 773 K

Designation of modules			Optimal parameters of leg materials (segments)	l_{leg} (l_{segm}), mm	P, W	I, A	U, V	η, %
One-segment (S1-S2)	n-type leg		$x = 0.02$	5.6	11	3.35	3.28	7.6
	p-type leg		$x = 0.062$	5.6				
Two-segment (S1-S2)	n-type leg	cold	$x = 0.01$	3.2	25.8	7.62	3.39	14.65
		hot	$x = 0.064$	2.4				
	p-type leg	cold	$x = -0.048$	2.4				
		hot	$x = 0.09$	3.2				
FGM module (S1-S2)	n-type leg		Fig 3 *a*	5.6	23.5	7.34	3.2	15.52
	p-type leg			5.6				
One-segment (S1-S4)	n-type leg		$x = 0.019$	5.6	10.59	3.125	3.39	7.47
	p-type leg		$x = 0.004$	5.6				
Two-segment (S1-S4)	n-type leg	cold	$x = 0.01$	3.3	19.26	5.47	3.52	12.25
		hot	$x = 0.059$	2.3				
	p-type leg	cold	$x = 0.0045$	2.3				
		hot	$x = 0.0075$	3.3				
FGM module (S1-S4)	n-type leg		Fig 3 *b*	5.6	18.5	5.6	3.31	14.04
	p-type leg			5.6				
One-segment (S3-S2)	n-type leg		$x = 1.65$	5.6	5.43	1.64	3.32	6.2
	p-type leg		$x = -0.048$	5.6				
Two-segment (S3-S2)	n-type leg	cold	$x = 1.1$	2.3	17.04	5.49	3.1	14.5
		hot	$x = 2.8$	3.3				
	p-type leg	cold	$x = -0.03$	3.3				
		hot	$x = 0.03$	2.3				
FGM module (S3-S2)	n-type leg		Fig. 3 *c*	5.6	19	6.13	3.1	15.49
	p-type leg			5.6				
One-segment (S3-S4)	n-type leg		$x = 1.73$	5.6	5.47	1.72	3.18	6.01
	p-type leg		$x = 0.0063$	5.6				
Two-segment (S3-S4)	n-type leg	cold	$x = 1.2$	2	14.3	4.5	3.17	12.67
		hot	$x = 2.43$	3.6				
	p-type leg	cold	$x = 0.006$	3.6				
		hot	$x = 0.0129$	2				
FGM module (S3-S4)	n-type leg		Fig. 3 *d*	5.6	15	4.84	3.1	13.88
	p-type leg			5.6				

Hence, in the selection of *n*-leg material, preference should be given to iodine-doped *PbTe* (S1), and *p*-leg material – $Zn_{3.96+x}Cd_{0.04}Sb_3$ (S2). Using materials with a certain impurity concentration distribution along the height of legs (Fig. 3), one can obtain modules characterized by higher efficiency values than their two-segment analogs (Table 3).

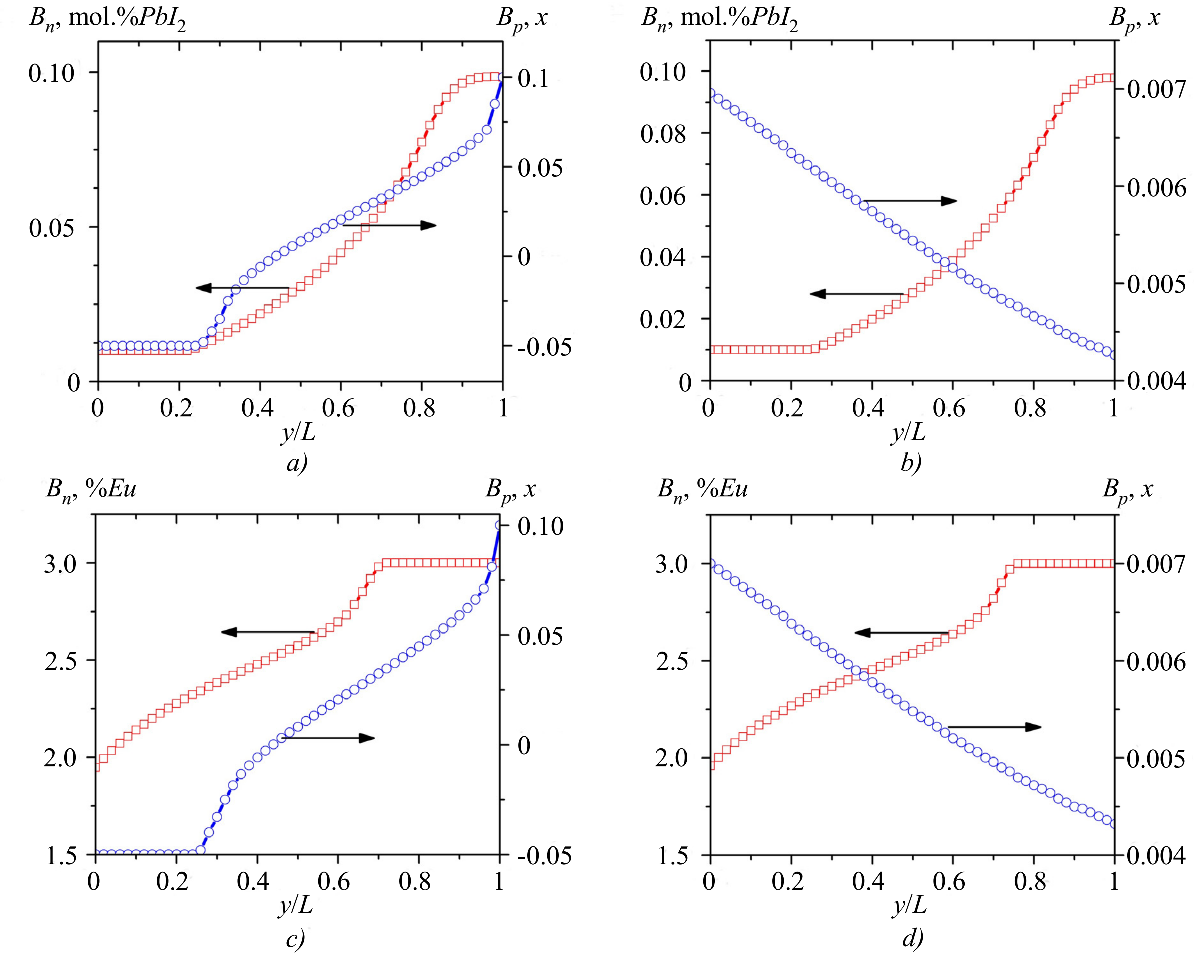

Fig. 3. Distribution of impurity content (composition) in FGM legs for generator modules: a) S1-S2; b) S1-S4; c) S3-S2; d) S3-S4.

Comparison of investigated segmented structures based on $PbTe/Zn_4Sb_3$ to modules based on *n*- and *p-PbTe* [16] shows that their efficiencies are commensurate, and the main advantage of β-Zn_4Sb_3 is its considerably lower cost and superior mechanical properties.

Multi-stage generator modules of $PbTe/Zn_4Sb_3$-based materials

The choice of leg materials for each module stage was done using optimal control theory methods [11], so that the cold and hot stages be characterized by maximum efficiency in the temperature range of 323 – 523 K and 523 – 773 K, respectively. The input data for optimization were experimentally measured temperature dependences of thermoelectric parameters (α, σ and κ) of iodine-doped *n-PbTe* [12] and *p*-$Zn_{3.96+x}Cd_{0.04}Sb_3$ [14] materials with different doping degrees (Fig. 1 *a*, 2 *a*), which showed the best results for the segmented modules. Optimal materials for two-stage module legs are listed in Table 4.

Using the optimal materials for *n*- and *p*-type legs, calculations of two-stage module structures were made (Table 5) with a series connection of the cold and hot stages, as well as thermal and electric matching of stages. The heat-absorbing and heat-releasing surfaces of modules are identical and make 40 × 40 mm^2.

Table 4

Optimal materials for a two-stage module

Designation of stages and legs		Leg material	Optimal concentration
cold	*n*-type	$PbTe+x$ mol.% PbI_2	$x = 0.01$
	p-type	$Zn_{3.96+x}Cd_{0.04}Sb_3$	$x = -0.048$
hot	*n*-type	$PbTe+x$ mol.% PbI_2	$x = 0.059$
	p-type	$Zn_{3.96+x}Cd_{0.04}Sb_3$	$x = 0.09$

From the data listed in Table 5 it is seen that with the increase in the dimensions of two-stage module thermoelements, a better efficiency is achieved with a considerably lower electric power (module № 1). To create a two-stage module with a maximum power for given operating temperature level, preference should be given to structure of module № 3. In so doing, the amount of thermoelectric material necessary for creation of a module is 1.5 times smaller compared to module № 2 and a factor of 3.6 smaller compared to module № 1.

Table 5

Calculated parameters of two-stage generator modules of $PbTe/Zn_4Sb_3$-based materials at T_h = 773 K, T_c = 323 K

№	Parameter	Parameter value		
		Module №1	Module №2	Module №3
1.	Cross-sectional area of the cold and hot stage legs, mm^2	4 × 4	1.8 × 4.3	1.5 × 1.5
2.	Cold stage leg height, mm	5.1	2.9	1.8
3.	Hot stage leg height, mm	5.8	3.2	2
4.	Number of leg couples of the cold and hot stages	32	48	160
5.	Electric power, P, W	7.62	9.78	14.79
6.	Voltage U, V	2.75	4.1	6.7
7.	Current I, A	2.77	2.38	2.2
8.	Efficiency η, %	13.18	13.07	12.91
9.	Amount of thermoelectric material, cm^3	5.58	2.27	1.52

Dependences of efficiency and electric power of two-stage modules on the hot side temperature are given in Fig. 4.

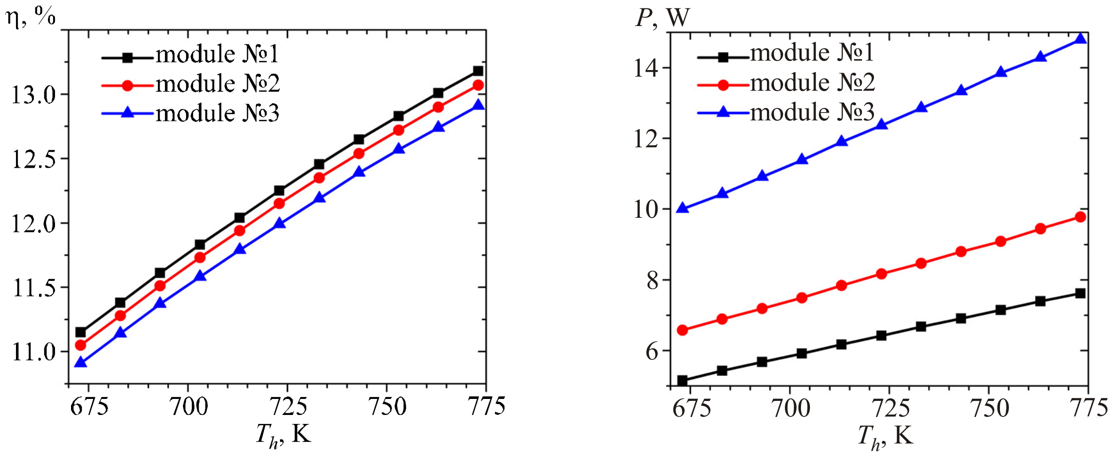

a) *b)*

Fig. 4. Dependences of efficiency (a) and electric power (b) of two-stage modules based on PbTe/Zn_4Sb_3 on the hot side temperature at T_c = 323 K.

As is evident from Fig. 4, in the range of hot side temperatures 673 – 773 K dependences of efficiency on the hot side temperature for modules № 1 – 3 are similar, the efficiency is increased from ~ 11 to ~ 13 %, the electric power of module № 3 is much higher as compared to the other two structures (by a factor of ~ 2).

Conclusions

Using optimal control theory methods, design of segmented and multi-stage modules of *PbTe/Zn_4Sb_3* –based materials is performed. Optimal concentrations of doping impurities for leg materials and optimal geometric parameters of legs whereby maximum efficiency of thermoelectric generator modules is achieved in the temperature range of 323 – 773 K are determined.

It is shown that the efficiency of one-segment modules of *PbTe/Zn_4Sb_3* materials is $\eta \approx 6 - 7.5$ %, two-segment – $\eta \approx 12.5 - 14.5$ %, FGM modules – $\eta \approx 14 - 15.5$ %, and multi-stage structures – $\eta \approx 13$ %. Under defined geometric parameters of multi-stage modules the optimal interstage temperature is within 495 – 525 K.

Thermoelectric structures based on *n-PbTe/p-Zn_4Sb_3* and *n-PbTe/p-PbTe* are characterized by identical efficiency. However, as compared to *p-PbTe*, *p-Zn_4Sb_3* has essentially lower cost and better mechanical properties, which on the whole offers it the advantage in the choice of a medium-temperature thermoelectric material for generator modules.

References

1. Z.H. Dughaish, Lead Telluride as a Thermoelectric Material for Thermoelectric Power Generation, *Physica B* **322**, 205 (2002).
2. E.P. Sabo, Technology of Chalcogenide Thermoelements, Physical Fundamentals, Chapter 1, Structure and Properties of Materials, *J. Thermoelectricity* **3**, 29 – 41 (2000).
3. S.H. Yang, T.J. Zhu, S.N. Zhang, J.J. Shen, X.B. Zhao, Natural Microstructure and Thermoelectric Performance of $(GeTe)_{80}(Ag_ySb_{2-y}Te_{3-y})_{20}$, *J. Electronic Materials* **39** (9), 2127 (2010).
4. B.S. Kim, I.H. Kim, J.K. Lee, N.K. Min, M.W. Oh, S.D. Park, H.W. Lee, and M.H. Kim, Electron Transport Properties of Rapidly Solidified $(GeTe)_x(AgSbTe_2)_{1-x}$ Pseudobinary Thermoelectric Compounds, *Electronic Materials Letters* **6** (4), 181 (2010).

5. E.A. Skrabek, D.S. Trimmer, Properties of the General TAGS System. *CRC Handbook of Thermoelectrics*, edited by D.M. Rowe, 1995, p. 267.
6. Mineral Commodity Summaries 2012, *U.S. Geological Survey* (Reston: Virginia, 2012), 198 p.
7. D.J.Singh, Electronic Transport in Old and New Thermoelectric Materials, *Science of Advanced Materials* **3**, 561 (2011).
8. J.-F. Li, W.-Sh. Liu, L.-D. Zhao, and M. Zhou, High-Performance Nanostructured Thermoelectric Materials, *NPG Asia Mater*. **2** (4), 152 (2010).
9. T.M. Tritt, Thermoelectric Phenomena, Materials, and Applications, *Annual Review of Materials Research* **41**, 433 (2011).
10. G.J. Snyder, E.S. Toberer, Complex Thermoelectric Materials, *Nature Materials* **7**, 105 (2008).
11. L.I. Anatychuk, L.N. Vikhor, *Thermoelectricity, Vol. IV, Functionally Graded Thermoelectric Materials* (Chernivtsi: Bukrek, 2012), 182 p.
12. V.M. Shperun, D.M. Freik, and R.I. Zapukhlyak, *Thermoelectricity of Lead Telluride and its Analogs* (Ivano-Frankivsk: Plai, 2000), 250 p.
13. H. Kong, Thermoelectric Property Studies on Lead Chalcogenides, *Double-Filled Cobalt Tri-Antimonide and Rare Earth-Ruthenium-Germanium, A Dissertation of Doctor of Philosophy (Physics),* The University of Michigan, 2008, 116 p.
14. Sh. Wang, F. Fu, X. She, G. Zheng, H. Li, X. Tang, Optimizing Thermoelectric Performance of *Cd*-Doped β-Zn_4Sb_3 through Self-Adjusting Carrier Concentration, *Intermetallics* **19** (12), 1823 (2011).
15. Sh. Wang, H. Li, D. Qi, W. Xie, and X. Tang, Enhancement of the Thermoelectric Performance of β-Zn_4Sb_3 by In Situ Nanostructures and Minute Cd-Doping, *Acta Materialia* **59**, 4805 (2011).
16. L.T. Strutynska, V.R. Bilinsky-Slotylo, V.Ya. Mykhaillovsky, Computer Design of Segmented *PbTe* Based Thermoelectric Modules, *J. Thermoelectricity* **3**, 44 – 49 (2012).

Submitted 20.12.2012.

L.I. Anatychuk[1,2], R.G. Giba[1], R.R. Kobylyanskii[1,2]

[1] Institute of Thermoelectricity NAS and MES of Ukraine, 1, Nauky Str., 58029, Ukraine;
[2] Yu. Fedkovych Chernivtsi National University, 2, Kotsyubinsky Str.,
Chernivtsi, 58000, Ukraine

SOME PECULIARITIES OF USING MEDICAL HEAT METERS IN THE INVESTIGATION OF LOCAL HUMAN HEAT RELEASE

This paper presents the results of computer simulation and experimental research on the effect of thermal insulation and spatial orientation of thermoelectric heat meter on its readings in the investigation of local human heat release. It has been proved experimentally that the presence of thermal insulation on thermoelectric heat meter does not always cause a decrease in its readings. In some cases it leads to their increase, since thermal insulation serves as a peculiar heat exchanger.

Key words: computer simulation, thermoelectric heat meter, medical thermal insulation, local human heat release.

Introduction

General characterization of the problem. Semiconductor thermoelectric heat meters are known to show good promise for the investigation of local human heat release [1-13]. They combine miniature size, fast response and parameter stability in a wide range of operating temperatures and are consistent with state-of-the art recording equipment [14, 15]. The use of such heat meters yields high locality and accuracy of heat measurements. This, in turn, affords an opportunity to obtain information on the characteristics of objects under study and analyze them in detail with the purpose of early detection of inflammatory processes in human body. However, the impact of different factors on the readings of thermoelectric heat meters remains an important issue.

Analysis of the literature. Effect produced by such heat meters on the object under investigation was studied analytically in [2], and for the case of living objects by means of computer simulation in [16, 17]. It was established that the influence of thermoelectric heat meter on measurement of human heat release can be minimized on condition of equality of heat exchange coefficients α_1, α_2 and radiation coefficients ε_1, ε_2 of heat meter and human skin surface, respectively. Also by means of computer simulation in [18] the effect of thermal insulation on thermoelectric heat meter readings was studied under real-service conditions. Besides, of paramount importance in the investigation of human heat release is heat meter spatial orientation, the method of its attachment to the surface of area under study and heat meter thermal insulation thickness increase that can affect considerably the thermoelectric heat meter readings.

Therefore, the purpose of this work is creation of improved computer model to determine the effect of thermal insulation and spatial orientation of thermoelectric heat meter on its readings, as well as experimental proof of the results obtained in the investigation of local human heat release.

Computer simulation results

To determine the effect of thermal insulation on thermoelectric heat meter readings, the model of biological tissue elaborated in [18] having on its surface thermoelectric heat meter with medical thermal insulation has been improved. Physical model improvement consists in approximating the shape and arrangement of medical thermal insulation to the real situation (Fig. 1). To construct an improved three-dimensional computer model, Comsol Multiphysics software package was employed [19], allowing simulation of thermophysical processes in human body biological tissue with account of blood circulation and metabolism. Calculation of temperature and heat flux density distributions in the biological tissue, thermoelectric heat meter and thermal insulation was done by finite element method (Fig. 2).

Computer simulation was used to obtain the distribution of temperature and heat flux density lines in the biological tissue of human body and thermoelectric heat meter (Fig. 3 – 5), as well as to construct isothermal surfaces in the biological tissue (Fig. 6) with regard to boundary effects in a three-dimensional computer model.

To determine temperature difference between thermoelectric heat meter surfaces, averaging of the resulting temperature distributions on the upper and lower heat meter surfaces was performed, since such distributions are nonuniform.

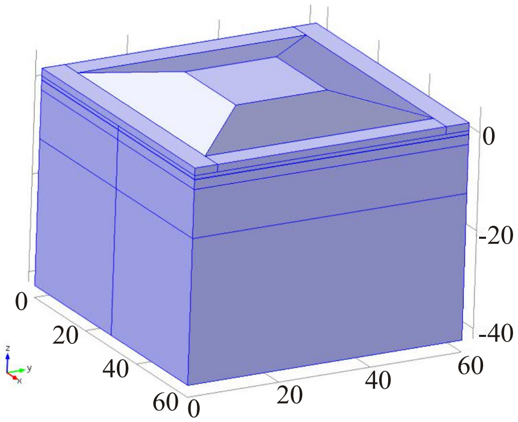

Fig. 1. Improved model of biological tissue having on its top thermoelectric heat meter with medical thermal insulation.

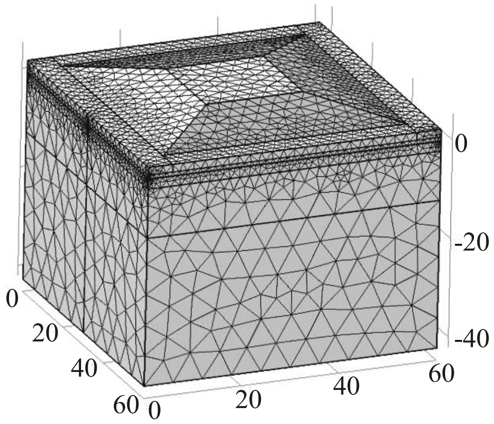

Fig. 2. Finite element method network.

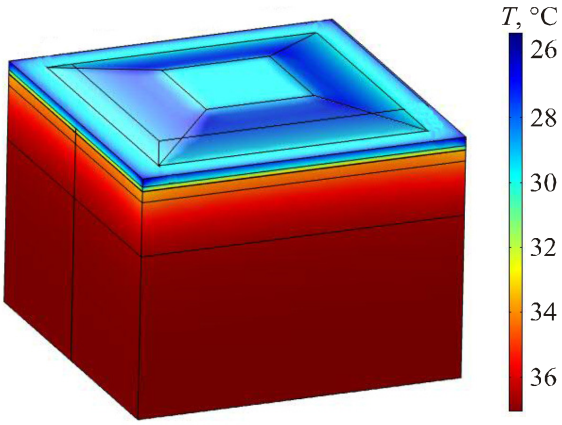

Fig. 3. Temperature distribution in biological tissue having on its top thermoelectric heat meter with medical thermal insulation.

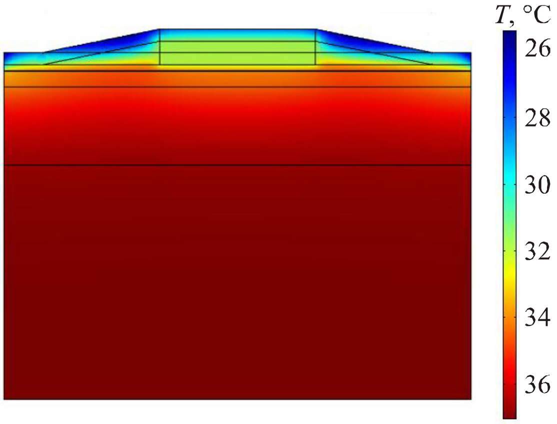

Fig. 4. Temperature distribution in the cut of biological tissue having on its top thermoelectric heat meter with medical thermal insulation.

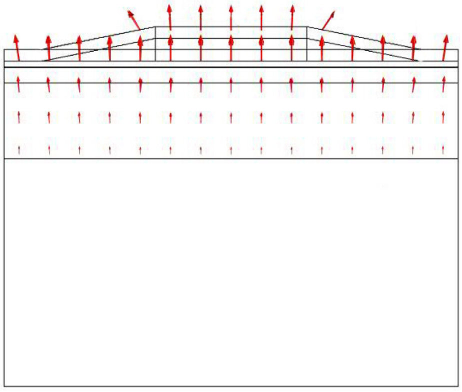

Fig. 5. Distribution of heat flux density lines in biological tissue having on its top thermoelectric heat meter with thermal insulation.

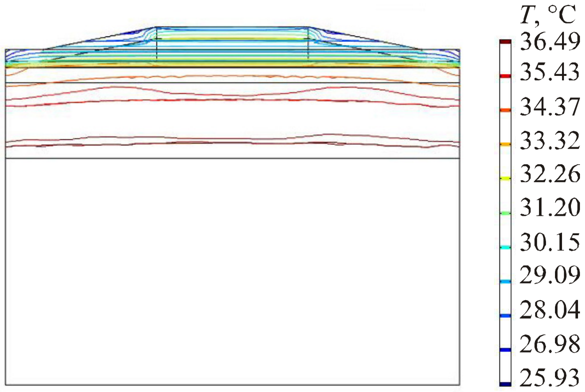

Fig. 6. Isothermal surfaces in biological tissue having on its top thermoelectric heat meter with medical thermal insulation.

Computer simulation was used to determine the effect of thermal insulation on thermoelectric heat meter readings under real-service conditions. Dependence of temperature difference on thermoelectric heat meter on the thickness of heat meter thermal insulation (the number of external bandage layers N_{extern}) was determined with different thickness of thermal insulation between the biological tissue and heat meter (the number of internal bandage layers N_{intern}) (Fig. 7).

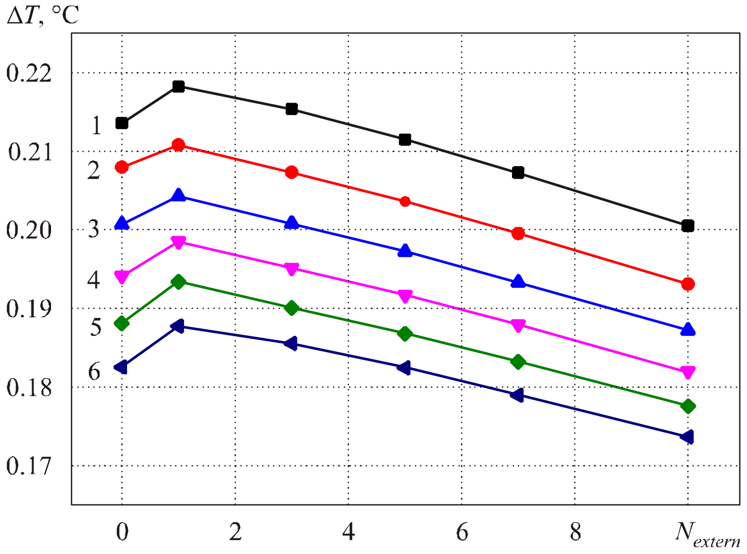

Fig. 7. Dependences of temperature difference on thermoelectric heat meter on the thickness of heat meter thermal insulation (the number of external bandage layers N_{extern}) with different thickness of thermal insulation between the biological tissue and heat meter (the number of internal bandage layers N_{intern}).
1 – N_{intern} = 0; 2 – N_{intern} = 1; 3 – N_{intern} = 2; 4 – N_{intern} = 3; 5 – N_{intern} = 4; 6 – N_{intern} = 5.

From Fig. 7 it is seen that increase in the thickness of thermal insulation between the biological tissue and thermoelectric heat meter definitely leads to a reduction of temperature difference between heat meter surfaces. However, increased thickness of heat meter external insulation does not always decrease its readings, and in some cases leads to their increase, since thermal insulation serves as a peculiar heat exchanger. This, in turn, must be taken into account when measuring local human heat release by creating identical conditions of repeated measurements.

Experimental studies of the effect of thermal insulation on thermoelectric heat meter readings

To determine the effect of thermal insulation on thermoelectric heat meter readings, a series of experimental measurements of local human heat fluxes was performed with different number of external N_{extern} and internal N_{intern} bandage layers. Measurement was performed on the area of human left hand at body temperature T_{body} = 36.6 °C and ambient temperature T_{room} = 20 °C with a horizontal arrangement of heat meter on the surface of area under study (Fig. 8).

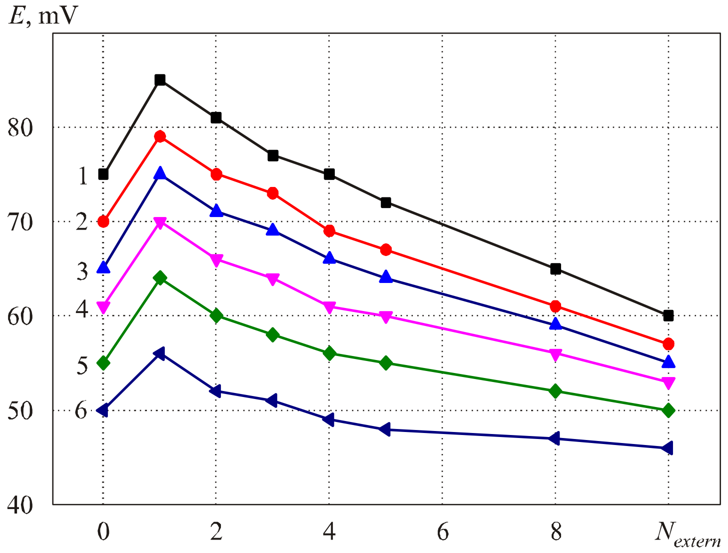

Fig. 8. Dependences of thermoelectric heat meter readings on thermal insulation thickness (the number of external N_{extern} and internal N_{intern} bandage layers) with a horizontal heat meter arrangement (φ = 0°) on the surface of human body area under investigation:
N_{extern} – the number of bandage layers on thermoelectric heat meter,
N_{intern} – the number of bandage layers between the skin and heat meter surface.
1 – N_{intern} = 0; 2 – N_{intern} = 1; 3 – N_{intern} = 2; 4 – N_{intern} = 3; 5 – N_{intern} = 4; 6 – N_{intern} = 5.

Thus, it has been established that the presence of thermal insulation on the biological tissue and thermoelectric heat meter does affect heat meter readings. From Fig. 8 it is seen that a small number of external layers of medical thermal insulation ($N_{extern} = 1 \div 4$) leads to increase in thermoelectric heat meter readings by 15 %, and further increase in thermal insulation (the number of external and internal bandage layers) reduces its readings by 40 % as compared to the case when thermal insulation is absent. Thus, the obtained results of experimental research confirm the assumption that thermal medical insulation serves as a peculiar heat exchanger and in some cases leads to increase in heat meter readings.

Table 1

Dependence of thermoelectric heat meter readings on the type of thermal insulation

№	Measurement conditions	*E*, mV
1.	$N_{intern} = 0$, $N_{extern} = 0$	75
2.	Ordinary jacket	65
3.	Knitted jacket	39
4.	Continental quilt	25

Also investigated was the influence of thermal insulation type on thermoelectric heat meter readings, that is, the cases of heat meter surface without thermal insulation, with clothing or continental quilt (Table 1). The measured data are represented in Fig. 9.

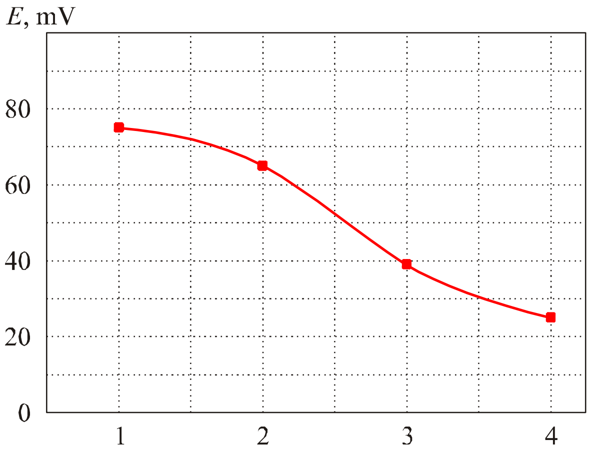

Fig. 9. Dependence of thermoelectric heat meter readings on the type of thermal insulation with investigation of local human heat release: 1 – no thermal insulation on heat meter surface, 2 – ordinary jacket, 3 – knitted jacket, 4 – continental quilt.

From Fig. 9 it is seen that the presence of thermal insulation on the surface of thermoelectric heat meter has a great impact on its readings which can decrease several times as compared to the case when thermal insulation is absent. This fact must be taken into account by creating identical conditions when measuring local heat fluxes of human body.

Dependence of thermoelectric heat meter readings on its spatial orientation

To determine the effect of spatial orientation of thermoelectric heat meter on its readings, a series of experimental measurements of heat fluxes from the respective area of human left hand was performed ($T_{body} = 36.7$ °C, $T_{room} = 20$ °C). The measured data are represented in Table 2 and Fig. 10, respectively, where φ is inclination angle of the hand with thermoelectric heat meter.

From Fig. 10 it is seen that with increasing the inclination angle of the left hand with a thermoelectric heat meter, its readings are reduced by 12 % with the number of bandage layers $N_{extern} = N_{intern} = 1$ and accordingly by 46 % with further increase in the number of bandage layers $N_{extern} = N_{intern} = 5$.

Table 2

Dependence of thermoelectric heat meter readings on its spatial orientation

φ, °	$N_{intern} = 1$ $N_{extern} = 1$	$N_{intern} = 2$ $N_{extern} = 2$	$N_{intern} = 3$ $N_{extern} = 3$	$N_{intern} = 4$ $N_{extern} = 4$	$N_{intern} = 5$ $N_{extern} = 5$
0	79	71	64	57	48
45	74	66	58	52	46
90	70	61	54	49	45

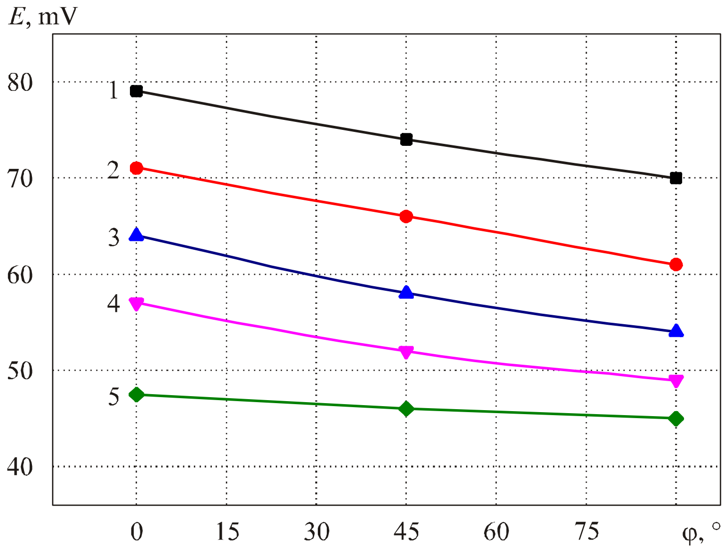

Fig. 10. Dependences of thermoelectric heat meter readings on its spatial orientation on the surface of human body area under investigation: N_{extern} – the number of bandage layers on thermoelectric heat meter, N_{intern} – the number of bandage layers between the skin and heat meter surface.
1 – N_{intern} = 1; 2 – N_{intern} = 2; 3 – N_{intern} = 3; 4 – N_{intern} = 4; 5 – N_{intern} = 5.

Thus, peculiarities of using medical heat meters in the investigation of local human heat release have been established. It has been found that spatial orientation of thermoelectric heat meter has a great impact on its readings which can vary up to 15 % depending on the thickness of medical thermal insulation on the heat meter surface.

Conclusions

1. Computer simulation results have been proved experimentally. It has been established that the presence of medical thermal insulation on thermoelectric heat meter does not always decrease its readings. In some cases it leads to their increase, since thermal insulation serves as a peculiar heat exchanger. However, further increase in the thickness of medical thermal insulation definitely leads to a decrease in heat meter readings about to 40 % as compared to the case when thermal insulation is absent.
2. It has been established that depending on spatial orientation of thermoelectric heat meter on human body area under investigation, heat meter readings can vary up to 15 %. This fact must be taken into account by creating identical conditions when measuring local human heat release.

References

1. L.I. Anatychuk, *Thermoelements and Thermoelectric Devices: Handbook* (Kyiv: Naukova Dumka, 1979), p. 766.
2. O.A. Geraschenko, *Foundations of Heat Flux Measurement* (Kyiv: Naukova Dumka, 1971), p. 192.
3. L.I. Anatychuk, N.G. Lozinsky, P.D. Mykytyuk, Yu.Yu. Rozver, Thermoelectric Semiconductor Heat Meter, *Instruments and Experimental Techniques* **5**, 236 (1983).
4. L.I. Anatychuk, L.P. Bulat, D.D. Gutsal, and A.P. Myagkota, Thermoelectric Heat Meter, *Instruments and Experimental Techniques* **4**, 248 (1989).
5. R.B. Ladyka, D.N. Moskal, V.D. Didukh, Semiconductor Heat Meters in Arthropathy Diagnostics

and Treatment, *Biomedical Engineering* **6**, 34 – 35 (1992).

6. R.B. Ladyka, O.N. Dakalyuk, L.P. Bulat, and A.P. Myagkota, Use of Semiconductor Heat Meters in the Diagnostics and Treatment, *Biomedical Engineering* **6**, 36 – 37 (1996).
7. B.M. Demchuk, L.Ya. Kushneryk, and I.M.Rublenyk, Thermoelectric Sensors for Orthopedics, *J. Thermoelectricity* **4**, 78 – 82 (2002).
8. A. Acheulov, L.Ya. Kushneryk, Thermoelectric Device for Medico-Biological Express-Diagnostics, *Tekhnologiya i Konstruirovaniye v Elektronnoi Apparature* **4**, 38 – 39 (2004).
9. B.M. Demchuk, R.R. Kobylyanskii, and A.V. Prybyla, Primary Thermoelectric Converters Based on Semiconductor Materials for Gradient Heat Meters, The 31-st International and 10-th European Conference on Thermoelectrics, Aalborg, Denmark, 2012, p. 277.
10. L.I. Anatychuk, R.R. Kobylyanskii, Thermoelectric Converters for Gradient Heat Meters, Proceedings of XIII Interstate Workshop “Thermoelectrics and Their Applications”, Saint-Petersburg, November 13-14, 2012, pp. 1-5.
11. L.I. Anatychuk, R.R. Kobylyanskii, Patent of Ukraine № 71619, Thermoelectric Medical Heat Meter, 2012.
12. L.I. Anatychuk, R.R.Kobylyanskii, Patent of Ukraine № 72032, Thermoelectric Sensor for Temperature and Heat Flux Measurement, 2012.
13. L.I. Anatychuk, R.R. Kobylyanskii, Patent of Ukraine № 73037, Thermoelectric Medical Device, 2012.
14. V.S. Gischuk, Electronic Recorder of Signals from Human Heat Flux Sensors, *J. Thermoelectricity* **4**, 101 – 104 (2012).
15. V.S. Gischuk, Electronic Recorder with processing Signals from Heat Flux Thermoelectric Sensor, *J. Thermoelectricity* **1**, 74 – 76 (2013).
16. L.I. Anatychuk, R.R. Kobylyanskii, Research into the Effect of Thermoelectric Heat Meter on Human Heat Release Measurement, *J. Thermoelectricity* **4**, 59 – 65 (2012).
17. L.I. Anatychuk, R.R. Kobylyanskii, 3D-Model for Determination of Thermoelectric Heat Meter Effect on the Accuracy of Human Heat Release Measurement, Scientific Bulletin of Chernivtsi University: Collected Scientific Works. Physics. Electronics, **2**, issue 1 (Chernivtsi: Chernivtsi National University, 2012), p. 15 – 20.
18. L.I. Anatychuk, R.R. Kobylyanskii, Computer Design of Thermoelectric Heat Meter Readings under Real-Service Conditions, *J. Thermoelectricity* **1**, 47 – 54 (2013).
19. COMSOL Multiphysics User’s Guide, COMSOLAB, 2010, 804 p.

Submitted 20.02.2013.

Yu.M. Lobunets

Yu.M. Lobunets

Institute of Thermoelectricity of NAS and MES
of Ukraine, 1, Nauky Str., Chernivtsi,
58029, Ukraine

SOLAR POND WITH THERMOELECTRIC ENERGY CONVERTER

Analysis has been performed of solar energy recovery scheme based on a solar (saline) pond with thermoelectric converter. The feasibility of creating a thermoelectric generator with a solar pond as the energy source (STEG) with acceptable technical and economic features has been demonstrated.

Key words: solar energy, solar pond, thermoelectric generator.

Introduction

A solar pond is a water reservoir 2 to 3 m deep, filled with a salt solution. Owing to the fact that solubility of salts in water is increased with a rise in temperature, situations are possible when solution stratification takes place, i.e. in the bottom layer the concentration (and density) of solution is increased, and in the surface layer it is decreased. In so doing, three distinct zones appear in the water reservoir, namely an upper convective zone 0.1...0.3 m thick, consisting of fresh water, a gradient layer where salt concentration increases with increasing the depth, and a bottom convective zone with maximum concentration of salts (Fig. 1).

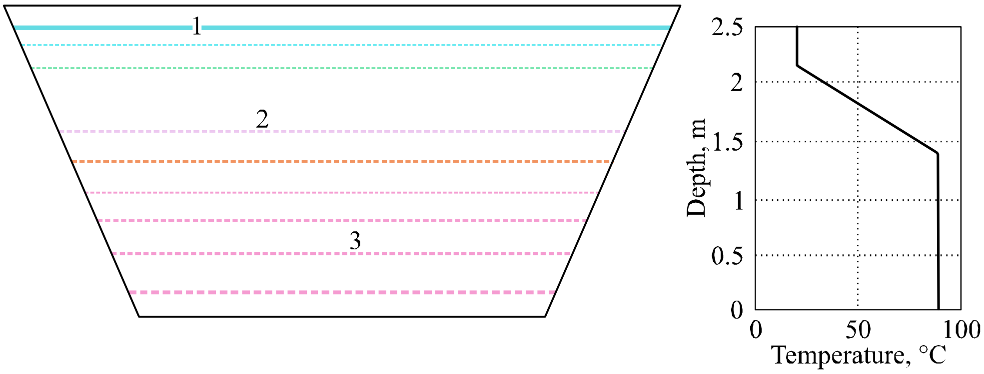

Fig. 1. Solar pond scheme [1]. 1 – fresh water; 2 – insulating layer with downward increasing brine salinity; 3 – hot brine layer.

Due to suppression of natural convection, the gradient layer possesses high thermal resistance (approximately three orders of magnitude higher than that of fresh water in vivo). As a result, the bottom layer is thermally insulated from the surface and capable of accumulating the energy of solar radiation. The temperature in the bottom layer can reach more than 100 °C. Thus, a solar pond is a concentrator and accumulator of solar energy at the same time. By estimates [2], a solar pond increases the density of solar radiation exergy many hundred thousand times, making this technology promising for creation of solar energy recovery systems.

At the present time, a number of power projects based on solar ponds with steam-vapour generators have been implemented [3]. In [4, 5], technical and economic analysis of such plants was performed which confirmed the advisability of using such systems. The specific power of such plants is of the order of 20 W/m^2 of water reservoir surface, which is 5...7 times higher compared to the existing hydroelectric power stations. In due time, research on the extent of possible use of Siwash salt bay was performed, by the results of which the energy potential of this bay was estimated as 10 GW of peak electric power. The scheme under consideration also fits well in the concept of integrated utilization of deep sea water [6] – the presence in the scheme of a low-temperature sink of thermal energy is capable of increasing considerably the efficiency of solar energy conversion system in general.

Alongside with known solutions, the use of thermoelectric generators in such systems can expand the area of application of such energy sources. This paper analyzes technical and economic features of solar energy conversion system of the type “solar pond-thermoelectric generator”.

Scheme of a TEG with a solar pond as the energy source (STEG)

Let us consider the features of a thermoelectric generator utilizing a solar pond as a source of thermal energy, and sea water as a sink. Thermal energy accumulated in the bottom layer of the pond is removed by heat carrier pumped through the collector placed on the bottom. Heat carrier is circulated through STEG heat exchanger. The generator is cooled by water coming to process scheme of a centre for using deep sea water [6].

To analyze the scheme, we employ a method for calculation of TEG stated in [7] and the features of solar ponds [4, 5].

Initial data for the analysis:

– net power of STEG N_o = 100 kW;
– hot water temperature t_{hot} = 80 °C;
– cold water temperature t_{cold} = 8 °C;
– solar pond efficiency η = 30 %;
– intergral flux of solar radiation E_o = 2000 kWh/m^2 per year;
– thermoelectric module figure of merit z = 0.003;
– thermoelement height h = 0.5 mm;
– module size 40 × 40 mm;
– cost of one module – 3 $;
– specific cost of heat exchanger – 250 $/m^2;
– specific cost of solar pond – 30 $/m^2 [5];
– cost of grid tie inverter – 150 $/kW;

As was shown in [7], the features of such system for ocean thermal energy converter (OTEG) are essentially dependent on the hydraulic resistance of thermoelectric generator heat exchangers. In the case under consideration, due to a higher TEG efficiency, this dependence is not decisive. The estimate of TEG cost for the system at hand is given in Figs. 2 and 3.

The most capital-intensive part of STEG is a source of heat comprising a solar pond and a collector. To assure round-the-clock operation of STEG, the pond must possess the necessary heat capacity. Under the above conditions, the necessary solar pond area is 300...350 m^2/kW. Accordingly, the specific cost of heat source is 10...12 thousand $/kW, and the specific cost of the whole device is of the order of 13 thousand $/kW (without including the land area necessary for creation of a pond). Therefore, a 100 kW STEG will require a solar pond of the area about 3.5 hectares; the cost of such device will be approximately 1.3 mln $.

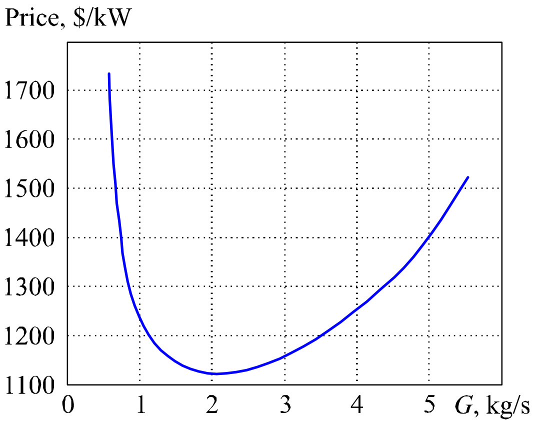

Fig. 2. Specific cost of TEG versus heat carrier flow rate.

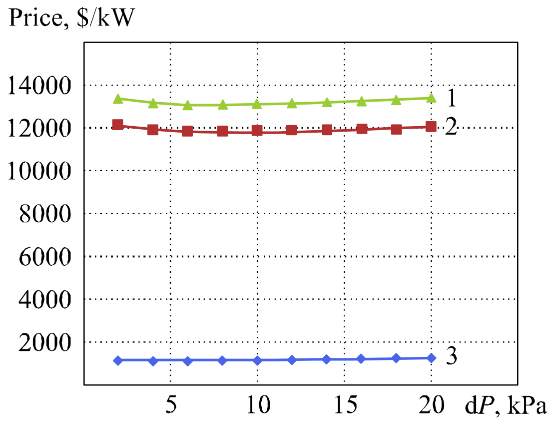

Fig. 3. Specific cost of STEG components versus the hydraulic resistance of heat exchangers.
1 – TEG cost, 2 – Solar pond cost, 3 – STEG cost.

The above data allow for using STEG in a base-load mode, i.e. at constant round-the-clock load. With full loading of STEG, electric energy generation will be about 900 thousand kW·h/year, which for standard depreciation periods of 20 years yields the electric energy cost of the order of 0.07 $/kW·h. With regard to maintenance costs, tax deduction and operating organization profit, this figure can increase maximum to 0.1 $/kW·h. Experience of using such systems suggests that with operation in a peak mode converter power can be increased by a factor of 3...5 with solar pond dimensions unchanged. Using STEG in a peak mode with the load coefficient of 50...70 %, the necesasry pond area (and capital expenditures) are reduced several times, and, accordingly, the cost of electric energy can be reduced to the level of 0.03...0.06 $/kW·h. For comparison, it should be noted that current feed-in tariff for systems of photoelectric solar energy conversion in the power range under consideration is 0.3...0.6 $/kW·h [8]. That is, the existing tariffs exceed by a factor of 5...10 the values obtained for STEG, proving high competitive ability of the scheme analyzed.

Conclusions

Analysis of thermoelectric system of solar energy conversion has shown the feasibility of creating STEG in the power range of 100 kW with technical and economic features acceptable for a wide commercial application.

References

1. N.V. Kharchenko, Individual Solar Plants (Moscow: Energoatomizdat, 1991), 208 p.
2. E.I. Yantovsky, Energy and Exergy Flows (Moscow: Nauka, 1988), 144 p.
3. http://soilwater.com.au/solarponds/history.HTM
4. R. Kayali, Economic Analysis and Comparison of Two Solar Energy Systems with Domestic Water Heating Systems, *J. of Physics* **22**, 489 – 496 (1998).
5. http://soilwater.com.au/solarponds/costs.htm
6. Deep Seewater “Kumejima model” // http://www.okinawab2b.jp/misc6.html
7. Yu.M. Lobunets, Performance Evaluation of OTEC with Thermoelectric Power Converter, *J. Thermoelectricity* **1**, 55 – 59 (2013).
8. http://www.renewableenergyworld.com/rea/news/article/2012/06/japan-approves-feed-in-tariffs

Submitted 01.02.2013.

V.S. Gischuk

V.S. Gischuk

Institute of Thermoelectricity
NAS and MES of Ukraine,
1, Nauky Str., Chernivtsi, 58029 Ukraine

MODERNIZED DEVICE FOR HUMAN HEAT FLUX MEASUREMENT

This paper presents the results of development of a modernized device intended for simultaneous measurement of heat flux density and temperature of human body surface by contact method. A special computer program "Termomonitor" is created for processing electronic recorder data, their storage and reproduction in a specified form on a personal computer which allows monitoring of temperature and thermal human state in real time. Device structural features, technical characteristics, flowchart and functional capabilities are shown.

Key words: heat flux, thermoelectric sensor, electronic recorder.

Introduction

General characterization of the problem. It is known that investigation of human heat release is enourmously important, since this information can bear evidence of exacerbation and rehabilitation processes alike. Therefore, development of highly sensitive heat flux thermoelectric sensors and electronic recorders of signals from these sensors is a relevant problem.

Analysis of the literature. A factor of importance in the investigation of human heat fluxes using such sensors is the accuracy and speed of recording signals from thermoelectric sensors. Previous developments of signal recorders [1-6] are characterized by a relatively high measurement error, large dimensions and a low speed and have no power supplies of their own. Later design efforts along this line resulted in creation of modern electronic recorders with processing information from thermoelectric sensors [7, 8] that have internal memory for storing the measured results and self-contained power supplies. However, the trouble with these devices is the impossibility of connecting several thermoelectric sensors at a time and the absence of simultaneous visulalization of measurements on a personal computer in real time.

Therefore, the purpose of this work is to develop a modernized medical device that allows real-time monitoring of temperature and thermal human state. Such information is important for the diagnostics of health condition.

Device design and technical characteristics

A modernized device for human heat flux measurement has been developed at the Institute of Thermoelectricity NAS and MES of Ukraine (Fig. 1).

The device is composed of electronic recorder (Fig. 1) and thermoelectric sensors (Fig. 2). The device includes special thermoelectric sensors [9, 10] which can register heat release due to evaporation from human skin surface. For this purpose, the sensors are made with air gaps between thermoelement rows, for the evaporation to take place from the sensor surface and to record in this way the real values of heat fluxes.

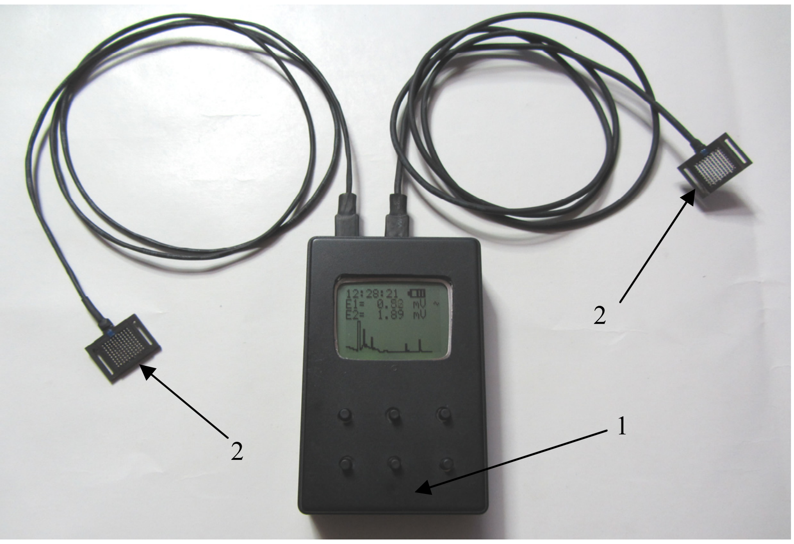

Fig. 1. Modernized device for human heat flux measurement: 1 − electronic recorder, 2 − thermoelectric sensor of heat flux and temperature.

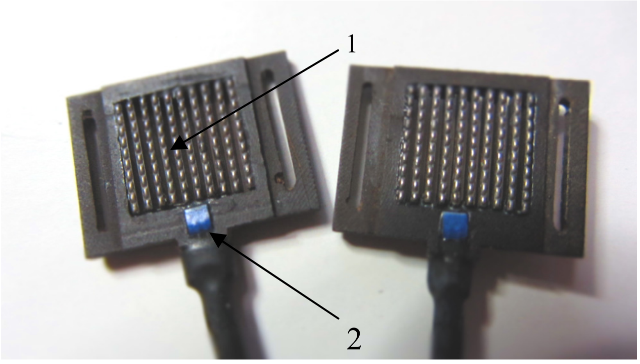

Fig. 2. Thermoelectric sensors of heat flux and temperature: 1 – thermopile for heat flux density measurement, 2 – sensor for temperature measurement.

Mounted on the device upper wall are two connectors for thermoelectric sensors of heat flux and temperature. The right side wall has a connector for microSD memory card and a miniUSB-connector for information exchange with a personal computer. The miniUSB-connector is also used for power supply to device battery.

Mounted on the case front wall is a liquid-crystal momochrome display with a resolution of 96 × 48 pixels. One pixel of display screen is matched by 10 mV of thermoelectric sensor electromotive force. The display shows plotted values of the heat flux of respective human body area in millivolts (mV) and temperature values in centigrade (°C). Thus, previous measurement data can be analyzed directly from the plots shown on the display. The presence of two thermoelectric sensors allows comparing the results of measuring the sick and healthy areas of human body surface.

Besides, the device front wall has 6 buttons for control over the device work − "LEFT", "RIGHT", "UP", "DOWN", "OK", "MENU". The “MENU” options have the following purpose:

- "START RECORDING" / "STOP RECORDING" – the device starts recording measured results into a new file, stops the respective record and saves information into memory card;
- "MODE SELECTION" – calls the submenu for selection of one of 9 information display modes in the form of real-time plots;
- "RECORDING PERIOD" – intended for selection of periodic intervals for recording measured

results into memory card file and displaying them on the device;

– "TIME/DATA" – transition to time and date adjustment mode;
– "BATTERY" – shows voltage on device supply battery;
– "HELP" – shows information on the device.

Device flowchart (Fig. 3) consists of the following functional assemblies: thermoelectric sensor with a built-in temperature sensor, analog-to-digital converter (ADC) for conversion of analog sensor signals to digital ones, multiplexor for commutation of ADC digital signals and their turn-by-turn transmission to microcontroller which is used for processing digital signals, their saving into memory card, graphical visualization of information on a display and personal computer.

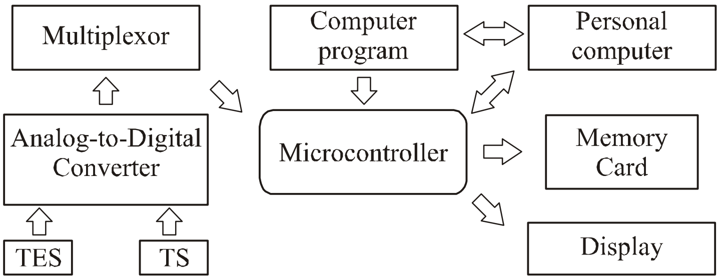

Fig. 3. Flowchart of a modernized device for human heat flux measurement:
TES – thermoelectric sensor, TS – temperature sensor.

The main functional assembly of electronic signal recorder is a microcontroller operating at a frerquency up to 20 MHz which asures high processing rate of signals from thermoelectric heat flux sensor. Personal computer is used to program the microcontroller which, in turn, controls the work of other functional assemblies of the device.

The device has a power supply of its own to provide the opportunity of its use in a self-contained mode together with a patient. This, in turn, allows expanding the device functional capabilities. Device power supply is from lithium-ion battrery of capacity 1200 mA/h, assuring 48 hours of uninterrupted device work.

Technical characteristics of device for measurement of human heat fluxes are given in Table 1.

Table 1

Technical characteristics of device for measuring human heat fluxes

№	Technical characteristics of device	Parameter values
1.	Operating temperature range of thermoelectric sensor	(0 ÷ 50.15) °C
2.	Time of measuring heat flux value	(100 ÷ 300) s
3.	Mesaurement time range for storing on memory card	1 ÷ 3600 s
4.	Number of measurement channels (thermoelectric sensors)	2
5.	Temperature measurement accuracy	± 0.1 °C
6.	Device supply voltage	3.6 V
7.	Device power consumption	~ 100 mW
8.	Dimensions of heat flux thermoelectric sensors	(0.02 × 0.015 × 0.0025) m
9.	Electronic recorder dimensions	(0.09 × 0.055 × 0.025) m
10.	Weight of heat flux thermoelectric sensor	0.01 kg
11.	Device weight	0.12 kg
12.	Time of uninterrupted device work	48 hours

Description of device computer program

Device computer program (Fig. 4 *a, b*) is written in Delphi programming language. The program allows exchanging data with the electronic recorder through USB-interface. Data exchange takes place according to HID-protocol (Human Interface Device), enabling device connection to personal computer without the neeed for installing additional drivers.

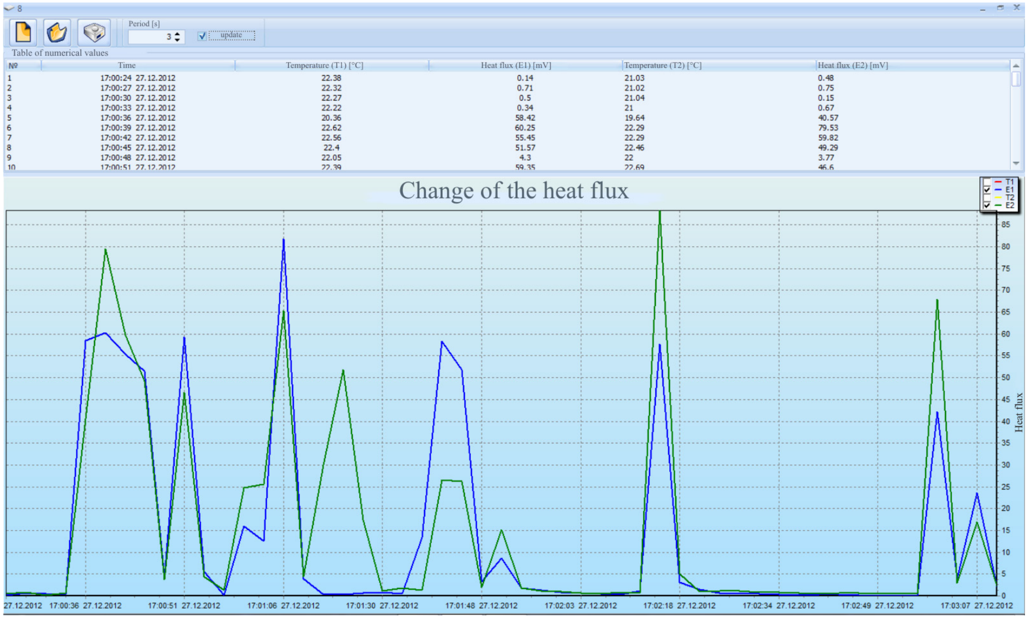

Period [s] 3

☑ update

Table of numerical values

№	Time	Temperature (T1) [°C]	Heat flux (E1) [mV]	Temperature (T2) [°C]	Heat flux (E2) [mV]
1	17:00:24 27.12.2012	22.38	0.14	21.03	0.48
2	17:00:27 27.12.2012	22.32	0.71	21.02	0.75
3	17:00:30 27.12.2012	22.27	0.5	21.04	0.15
4	17:00:33 27.12.2012	22.22	0.34	21	0.67
5	17:00:36 27.12.2012	20.36	58.42	19.64	40.57
6	17:00:39 27.12.2012	22.62	60.25	22.29	79.53
7	17:00:42 27.12.2012	22.56	55.45	22.29	59.82
8	17:00:45 27.12.2012	22.4	51.57	22.46	49.29
9	17:00:48 27.12.2012	22.05	4.3	22	3.77
10	17:00:51 27.12.2012	22.39	59.35	22.69	46.6

a)

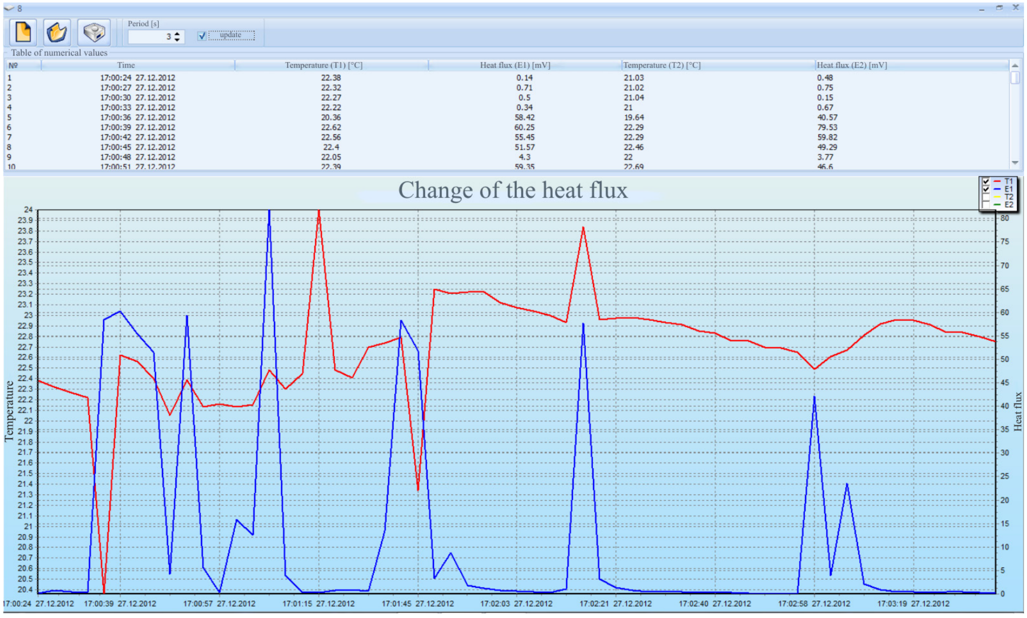

Period [s] 3

☑ update

Table of numerical values

№	Time	Temperature (T1) [°C]	Heat flux (E1) [mV]	Temperature (T2) [°C]	Heat flux (E2) [mV]
1	17:00:24 27.12.2012	22.38	0.14	21.03	0.48
2	17:00:27 27.12.2012	22.32	0.71	21.02	0.75
3	17:00:30 27.12.2012	22.27	0.5	21.04	0.15
4	17:00:33 27.12.2012	22.22	0.34	21	0.67
5	17:00:36 27.12.2012	20.36	58.42	19.64	40.57
6	17:00:39 27.12.2012	22.62	60.25	22.29	79.53
7	17:00:42 27.12.2012	22.56	55.45	22.29	59.82
8	17:00:45 27.12.2012	22.4	51.57	22.46	49.29
9	17:00:48 27.12.2012	22.05	4.3	22	3.77
10	17:00:51 27.12.2012	22.39	59.35	22.69	46.6

b)

Fig. 4. Interface of "TermoMonitor" computer program for processing electronic recorder data, their storing and reproduction in specified form on personal computer:
a) a change in heat flux of 2 thermoelectric sensors is represented;
b) a change in heat flux and temperature of the 1st thermoelectric sensor is represented.

Selecting the mark “DATA UPDATE” in computer program runs a cycle which sends requests for data transfer from the electronic recorder. In response to these requests, the recorder sends data package on temperature and heat flux of thermoelectric sensors with a prescribed time interval. The obtained data package is processed, following which the information is displayed on a personal computer in the form of tables and plots.

On pressing the button "SAVE", all data from the table are converted into "row" values (ordinary text), divided by dot and comma and written into a file with "csv" extension which can be opened using any program for work with electronic tables (Microsoft Excel, etc). On opening the file with such program, the "csv"-format is decoded into a data package with a floating point, which enables information dosplay in the form of a table and the respective plots on a personal computer.

Conclusions

1. A modernized device is developed that allows simultaneous measurement of temperature and heat fluxes with recording information on their values in real time for 48 hours. The device has a capability of connecting several thermoelectric sensors at a time and provides visualization of sensor signals both on a display and on a personal computer in the form of time-dependent plots. Information transfer to a personal computer for its further processing according to prescribed algorithm is foreseen.
2. Special "TermoMonitor" computer program is developed for processing data from electronic recorder of thermoelectric sensor signals, their storage and reproduction in a prescribed form on a personal computer.
3. The device performs monitoring of temperature and thermal human state, which allows early revealing the inflammatory processes of human organism, various diseases and express-diagnostics during mass health examination.

References

1. L.I. Anatychuk, *Thermoelements and Thermoelectric Devices. Handbook* (Kyiv: Naukova Dumka, 1979), 766 p.
2. L.I. Anatychuk, N.G. Lozinsky, P.D. Mykytyuk, Yu.Yu. Rozver, Thermoelectric Semiconductor Heat Meter, *Instruments and Experimental Techniques* **5**, 236 (1983).
3. L.I. Anatychuk, L.P. Bulat, D.D. Gutsal, A.P. Myagkota, Thermolectric Heat Meter, *Instruments and Experimental Techniques* **4**, 248 (1989).
4. B.M. Demchuk, L.Ya. Kushneryk, and I.M. Rublenyk, Thermoelectric Sensors for Orthopedy, *J. Thermoelectricity* **4**, 78 – 82 (2002).
5. A.A. Ascheulov, L.Ya. Kushneryk, Thermoelectric Device for Medico-Biological Express Diagnostics, *Tekhnologiya i Konstruirovanie v Elektronnoi Apparature* **4**, 38 – 39 (2004).
6. L.K. Holtermann, *Patent US 4198859. Heat flow probe*, 1980.
7. V.S. Gischuk, Electronic Recorder of Signals from Human Heat Flux Sensors, *J. Thermoelectricity* **4**, 101 – 104 (2012).
8. V.S. Gischuk, Electronic Recorder with Processing Signals from Human Heat Flux Sensors *J. Thermoelectricity* **1**, 74 – 76 (2013).
9. L.I. Anatychuk, R.R. Kobylyansky, *Patent of Ukraine № 72032, Thermoelectric Sensor for Temperature and Heat Flux Measurement*, 2012.
10. L.I. Anatychuk, R.R. Kobylyansky, *Patent of Ukraine № 71619. Thermoelectric Medical Heat Flux Meter*, 2012.

Submitted 29.12.2012.

NEWS

INTERNATIONAL THERMOELECTRIC ACADEMY

DMYTRO MYKHAILOVYCH FREIK

(DEDICATED TO 70-th BIRTHDAY)

On April 5, 2013 Dmytro Mykhailovych Freik – Honoured Worker of Science and Technology of Ukraine, academician of the International Thermoelectric Academy, academician of the Higher School Academy of Sciences of Ukraine, DSc in Chemistry, professor, Director of Physics and Chemical Institute of V.Stefanyk National University, Head of Department of Physics and Chemistry of Solid State, celebrated his 70-th jubilee.

Dmytrro Mykhailovych Freik was born on April 5, 1943 in the village of Kinashiv, Halyts district, Ivano-Frankivsk region. In 1964 he graduated from Physics and Mathematics Faculty of Ivano-Frankivsk State Pedagogical Institute, and later – the post-graduate course at I. Franko Lviv State University. In 1968 he maintained his PhD thesis, and in 1984 – doctoral thesis. Since 1968 he has worked at V.Stefanyk Precarpathian University, rising through the ranks from assistant to professor.

Dmytro Mykhailovych Freik is a scientist of world reputation who has founded a new research area – the physics and chemistry of materials science of nanostructures, thin films and crystals of $A^{II}B^{VI}$, $A^{IV}B^{VI}$ compounds and solid solutions on their basis, promising for active elements of opto- and microelectronics, infra-red engineering and thermoelectricity. For the first time the integrated crystal-chemical and thermodynamic approaches were used to specify the mechanisms of defect subsystem creation which determine optimal values of their thermoelectric characteristics.

D.M. Freik is an experienced pedagogue, organizer and leader. He is the founder of scientific and pedagogical school of semiconductor materials science in the Precarpathian University and the region as a whole. Under the guidance of prestigious scientist, the scientific workers community successfully functions, high-skilled brainpower for the purposes of science and industry is trained. Under the supervision of professor Freik, 52 PhD and 3 doctoral theses have been maintained. He is the co-author of over 800 monographs, scientific papers, certificates of authorship for inventions and patents of Ukraine.

D.M. Freik is the founder and editor-in-chief of All-Ukrainian journal “Physics and Chemistry of Solid State”, a member of editorial boards of several scholarly journals and specialized councils for the defense of theses, full member of many scientific societies and organizations.

For achievements in scientific, pedagogical and social activity D.M. Freik was awarded with the Third Class Order of Merit (2009), many other distinctions – “For Scientific Achievements”, “For Contribution to Science” (2008), diploma “Outstanding Scientist of the Year” (2011). The scientist has won international acclaim: he was awarded with medal of RAS “Academician Nikolai Semenovich Kurnakov” (1978), the International G.Soros grant (1995), recognized as an Outstanding Scientist of the XX century (1999, England), Leader of New Epoch (2000, USA) and “Man of the Year 2001” (USA); he was elected full member of New-York Academy of Sciences, academician of the International Thermoelectric Academy, academician of Higher School Academy of Sciences of Ukraine.

International Thermoelectric Academy, Institute of Thermoelectricity of the National Academy of Sciences and Ministry of Education and Science, Youth and Sports of Ukraine, “Journal of Thermoelectricity” Publishers cordially greet the esteemed Dmytro Mykhailovych Freik on his glorious 70-th jubilee, wishing him sound health, happiness and new scientific achievements.

ARTICLE PREPARATION RULES

The article shall conform to the journal profile. The article content shall be legible, concise and have no repetitions.

The article shall be submitted to the editorial board in electronic version.

The text shall be typed in text editor not lower than MS Word 6.0/7.0.

Page setup: “mirror margins”- top margin – 2.5 cm, bottom margin – 2.0 cm, inside – 2.0 cm, outside– 3.0 cm, from the edge to page header – 1.27 cm, page footer – 1.27 cm.

Graphic materials, pictures shall be submitted in color or, as an exception, black and white, in .opj or .cdr formats, .jpg or .tif formats being also permissible. According to author’s choice, the tables and partially the text can be also in color.

The article shall be submitted in English on A4 paper sheets; the number of pages shall not exceed 12. By agreement with the editorial board, the number of pages can be increased.

To accelerate publication of the article, please adhere to the following rules:

- the authors’ initials and names are arranged in the centre of the first page at the distance of 1 cm from the page header, font Times New Roman, size 12 pt, line spacing 1.2;
- the name of organization, address (street, city, postal code, country) – indent 1 cm below the authors’ initials and names, font Times New Roman, size 11 pt, line spacing 1.2, center alignment;
- the title of the article is arranged 1 cm below the name of organization, in capital letters, semi-bold, font New Roman, size 12 pt, line spacing 1.2, center alignment. The title of the article shall be concrete and possibly concise;
- the abstract is arranged 1 cm below the title of the article, font Times New Roman, size 10 pt, in italics, line spacing 1.2 ,center alignment;
- key words are arranged below the abstract, font Times New Roman, size 10 pt, line spacing 1.2, justified alignment. The title “Key words” – font Times New Roman, size 10 pt, semi-bold;
- the main text of the article is arranged 1 cm below the abstract, indent 1 cm, font Times New Roman. size 11 pt, line spacing 1.2, justified alignment;
- formulae are typed in formula editor, fonts Symbol, Times New Roman. Font size is “normal” – 12 pt, “large index” – 7 pt, “small index” – 5 pt, “large symbol” – 18 pt, “small symbol” – 12 pt). The formula is arranged in the text, centre aligned and shall not occupy more than 5/6 of the line width, formulae are numbered in round brackets right;
- dimensions of all quantities used in the article are represented in the International System of Units (SI) with the explication of the symbols employed;
- figures are arranged in the text. The figures and pictures shall be clear and contrast; the plot axes – parallel to sheet edges, thus eliminating possible displacement of angles in scaling;
- tables are arranged in the text. The width of the table shall be 1 cm less than the line width. Above the table its ordinary number is indicated, right alignment. Continuous table numbering throughout the text. The title of the table is arranged below its number, center alignment;
- references should appear at the end of the manuscript. References within the text should be enclosed in square brackets. References should be numbered in order of first appearance in the text. Examples of various reference types are given below.

- L.I. Anatychuk, *Thermoelements and Thermoelectric Devices: Handbook* (Kyiv: Naukova Dumka, 1979), p.766. (Book)
- T.M. Tritt, Thermoelectric Phenomena, Materials, and Applications, *Annual Review of Materials Research* **41**, 433 (2011). (Journal paper)
- U. Ghoshal, *Proceedings of the XXI International Conference on Thermoelectrics* (N.Y., USA, 2002), p. 540. (Proceedings Conference)

The article should be supplemented by:

- letter from the organization where the work was performed or from the authors of the work applying for the publication of the article;
- information on the author (authors): last name and initials; full name and postal address of the institution where the author works; academic degree; position; telephone number; E-mail;
- author's (authors') photo in color or, as an exception, in black and white. With the number of authors more than two their photos are not given;
- author's application to the following effect:

> We, the undersigned authors, … transfer to the founders and editors of "Journal of Thermoelectricity" the right to publish the article…in Ukrainian, Russian and English. This is to confirm that the present publication does not violate the copyright of other persons or organizations.
>
> Date Signatures

Below is given an example of article preparation.

Author's
photo
3 × 4 cm

A.I. Casian[1], B.M. Gorelov[2]

[1]Technical University of Moldova,
168, Stefan cel Mare Ave.,
Chisinau, MD-2004, Moldova;
[2]Institute of Surface Chemistry of National Academy
of Sciences of Ukraine, 17, Gen. Naumov Str.,
Kyiv, 03164, Ukraine

Author's
photo
3 × 4 cm

STATE OF THE ART AND PROSPECTS OF THERMOELECTRICITY ON ORGANIC MATERIALS

The aim of the paper is to analyze the expected thermoelectric opportunities of organic materials, including some highly conducting quasi-one-dimensional crystals. It is shown that interest of investigators in these materials has been growing recently. Quasi-one-dimensional organic crystals have high prospects for thermoelectric applications. These materials combine the properties of multi-component systems with more diverse internal interactions and of quasi-one-dimensional quantum wires with increased density of electronic states. It is shown that the values of the thermoelectric figure of merit $ZT \sim 1.3 - 1.6$ at room temperature are expected in really existing organic crystals of tetrathiotetracene-iodide, TTT_2I_3, if the crystal parameters are approaching the optimal ones.

Key words: thermoelectricity, tetrathiotetracene-iodide, polarizability.

Introduction

It is known that conducting organic materials usually have much lower thermal conductivity than the inorganic materials. Moreover, the organic materials can be fabricated by simpler chemical methods, and it is expected that such materials will be less expensive in comparison with the inorganic ones. Exactly these properties attracted attention to such materials for the use in thermoelectric (TE) applications long time ago [1, 2]. In spite of relatively high value of the thermoelectric figure of merit $ZT = 0.15$ at room temperature observed in polycopper phthalocyanine [2] as early as 1980, the thermoelectric properties of organic materials are still weakly investigated. This situation has the only explanation that thermoelectricians are still weakly interested in organic materials, and organic chemists are also weakly interested in thermoelectric materials. Moreover, in order to seek good organic thermoelectrics, it is necessary to organize multidisciplinary consortiums of physicists, organic chemists and engineers in the field of thermoelectricity. …

The aim of this paper is to present briefly the state-of-the-art of investigations in the area of new organic thermoelectric materials and to describe the nearest expected results for really existing quasi-one-dimensional organic crystals of tetrathiotetracene-iodide, TTT_2I_3.

Quasi-one-dimensional organic crystals of TTT_2I_3

The structure of quasi-one-dimensional organic crystals of tetrathiotetracene-iodide, TTT_2I_3, has been briefly described in [34]. These needle-like crystals are formed of segregate chains or stacks of planar molecules of tetrathiotetracene TTT, and iodine ions. The chemical compound TTT_2I_3 is of mixed-valence: two molecules of TTT give one electron to the iodine chain which is formed from I_3^- ions. The conductivity of iodine chains is negligibly small, so that only *TTT* chains are electrically conductive and holes serve as carriers. The electrical conductivity σ along *TTT* chains at room temperature varies between 10^3 and $10^4\ \Omega^{-1}\text{cm}^{-1}$ for crystals grown by gas phase method [35], and between 800 and $1800\ \Omega^{-1}\text{cm}^{-1}$ for crystals grown from solution [36]. Thus, the conductivity is very sensitive to crystal impurity and perfection which depends on growth method. In the direction perpendicular to chains σ is by three orders of magnitude smaller than in the longitudinal direction and is neglected. …

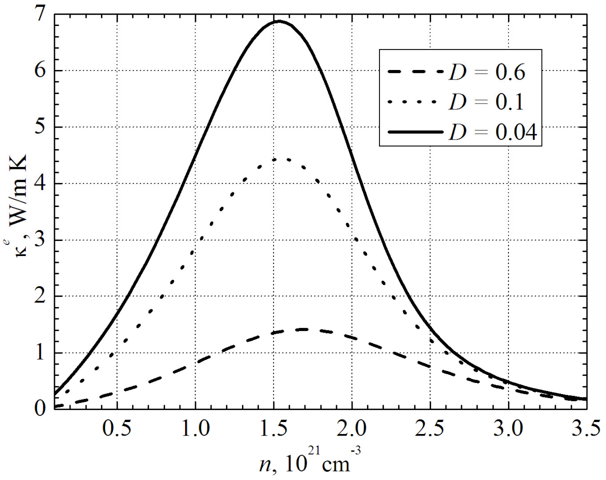

Fig. 1. Dependences of electron thermal conductivity κ^e *on n.*

$$\sigma = R_0,\ S = R_1 / eTR_0,\ \kappa^e = \left(e^2T\right)^{-1}\left(R_2 - R_1^2 / R_0\right), \tag{1}$$

Thermoelectric properties

Expressions (2) – (3) have been calculated in order to determine the thermoelectric properties of quasi-one-dimensional organic crystals of TTT_2I_3 with different degrees of purity….

Conclusions

The state-of-the-art of research on new organic materials for thermoelectric applications is analyzed. It is shown that the interest of investigators in these materials has been growing in recent years. The highest value of $ZT \sim 0.38$ at room temperature has been measured in doped acetylene, with the only problem that this material is not stable. Accurate control of the oxidation level in poly (3, 4-ethylenedioxythiophene) (PEDOT) gave the power factor 324 $\mu\text{W}\cdot\text{m}^{-1}\text{K}^{-2}$ and in combination with its low intrinsic thermal conductivity ($\kappa = 0.37\ \text{W}\cdot\text{m}^{-1}\text{K}^{-1}$) yielded $ZT = 0.25$ at room temperature, and this material is air-stable….

References

1. Ali Shakouri, Recent Developments in Semiconductor Thermoelectric Physics and Materials, *Annu.Rev.Mater.Res.***41**, 399-431 (2011).
2. L.I. Anatychuk, *Thermoelectricity, Vol.2, Thermoelectric Power Converters* (Kyiv, Chernivtsi: Institute of Thermoelectricity, 2003), 376p.
3. M.E. Bengen, *German Patent Appl.* OZ 123, 438, 1940; *German Patent* 869,070, 1953, Tech. Oil Mission Reel, 143,135, 1946.

ISSN 1607 - 8829. Journal of Thermoelectricity. 2013. № 2. 1-104